TÉCNICO LISBOA

Numerical characterization and flow optimization and heat transfer inside corrugated tubes

Milton Mateush

Thesis to obtain the Master of Science Degree in

Mechanical Engineering

Supervisors: Prof. José Manuel da Silva Chaves Ribeiro Pereira
Prof. Miguel Abreu de Almeida Mendes

Examination Committee

Chairperson: Prof. Carlos Frederico Neves Bettencourt da Silva
Supervisor: Prof. Miguel Abreu de Almeida Mendes
Member of the Committee: Prof. Ana Sofia Oliveira Henriques Moita

October 2021

To my mother Galina and my brother Dolfin

Acknowledgments

First of all I want to thank my mother and my brother for always supporting me not only in the good times but also in the bad times and giving me strength to finish this work.

I also want to thank professor Miguel Mendes and José Chaves for accompanying me during the process and for making the revision of the work done.

Finally, last but not least, I want to thank Gonçalo Granjal for helping me solving some doubts that i had during the process of making this work.

For all of you thank you verty much.

Resumo

O escoamento interno em 9 tubos corrugados com passo ($p = 6, 9, 12\ mm$) e altura de corrugação ($e = 0.4, 0.5, 0.6\ mm$), de regime $Re = 100 - 3000$, foram estudados neste trabalho para optimizar o escoamento e verificar a influência da geometria de corrugação em perdas de pressão e transferência de calor. Com água como fluido e fluxo de calor constante imposto na parede, $100\ kW/m^2$, foi desenvolvido um modelo numérico com o CFD software STAR-CCM+, onde o modelo $k-\omega$ SST foi usado para modelar a turbulência. Os resultados numéricos obtidos foram validados com os dados experimentais diponíveis. Estes demonstram que a corrugação induz vórtices que promovem regiões de recirculação de escoamento que diminuem o Reynolds crítico e antecipam o início da transição. O factor de performance térmico foi comparado ao tubo liso. A melhor performance das geometrias corrugadas foi para $Re = 850 - 2300$ onde foi verificado um crescimento praticamente linear. O tubo com $p = 6$, $e = 0.6\ mm$ foi o melhor para $Re = 850$, o $p = 12$, $e = 0.5\ mm$ foi o melhor para $Re = 2300$ e o $p = 12$, $e = 0.6\ mm$ foi o melhor no meio do intervalo. Para $Re = 100 - 700$ os tubos corrugados demonstram pior performance que o tubo liso. Para $Re = 3000$ a performance é similar. Um estudo de otimização multi-objetivo também é realizado e concluiu-se que para um permutador de calor com a menor potência de bombagem deve-se usar o tubo com $p = 6$, $e = 0.6\ mm$ a $Re = 850$ e para máxima performance térmica o $p = 12$, $e = 0.5\ mm$ a $Re = 2300$.

Palavras-chave: escoamento interno, altura da corrugação, passo da corrugação, potência de bombagem, performance térmica, aprimoramento de transferência de calor, tubos corrugados

Abstract

The internal flow in 9 corrugated tubes with pitch ($p = 6, 9, 12\ mm$) and corrugation height ($e =\ 0.4$,0.5, $0.6\ mm$), regime $Re = 100-3000$, was studied in this work to optimize the flow and verify the influence of the corrugation geometry on pressure losses and heat transfer. With water as working fluid and constant heat flux imposed on the tube wall, $100\ kW/m^2$, a numerical model was developed with the CFD software STAR-CCM+, where the $k-\omega$ SST model was used for turbulence. Numerical results were obtained and validated with the available empirical data. These demonstrate that corrugation induces a swirl promoting recirculating flow regions which decrease the critical Reynolds number and anticipate onset of the transition region. The thermal performance factor was evaluated and compared to the smooth tube. The best performance for the corrugation geometries was for $Re =\ 850 -\ 2300$ where it was verified an almost linear growth. The tube with $p = 6$, $e = 0.6\ mm$ was the best for $Re = 850$, the $p = 12$, $e = 0.5\ mm$ was the best for $Re = 2300$ and the $p = 12$, $e = 0.6\ mm$ was the best in between. For $Re = 100 - 700$ the corrugated tubes show an under-performance compared to the smooth tube. For $Re = 3000$ the performance is similar and doesn't justify the use of a corrugated geometry. A multi-objective optimization study is also performed and it was concluded that for a heat exchanger with the lower pumping power one should use the tube with $p = 6$, $e = 0.6\ mm$ at $Re = 850$ and for maximum thermal performance the $p = 12$, $e = 0.5\ mm$ at $Re = 2300$.

Keywords: internal flow, corrugation height, corrugation pitch, pumping power, thermal performance, heat transfer enhancement, corrugated tubes

Contents

List of Tables

List of Figures

Nomenclature

Greek symbols

Δp	Pressure drop. [Pa]
ϵ	Dissipation rate. [J/(kg $\cdot s$)]
μ	Dynamic viscosity. [N $\cdot s/m^2$]
ν	Kinematic viscosity. [m$^2/s$]
ω	Specific dissipation rate. [1/s]
Φ	Dissipation function. [-]
ϕ	Severity index. [-]
ρ	Density. [kg/m^3]
τ	Surface stress. [J/m^2]
φ	Solution variable. [-]

Roman symbols

$\mathbf{u}$	Velocity vector. [m/s]
$\dot{V}$	Volumetric flow. [m$^3/s$]
$\dot{m}$	Mass flow. [kg/s]
$\dot{q}$	Heat flux. [W/m^2]
A_c	Cross section area. [m^2]
A_{wet}	Wet area. [m^2]
c_p	Specific heat at constant pressure. [J/(kg $\cdot K$)]
D	Tube's diameter. [m]
D_e	Outer diameter. [m]
D_h	Hydraulic diameter. [m]

D_i Inner diameter. [m]

E Energy. [J]

e Corrugation height. [m]

f Friction factor. [-]

g Gravity. [m/s^2]

h Local convective heat transfer coefficient. [W/(m$^2 \cdot K$)]

i Internal thermal energy. [J]

k Thermal conductivity. [W/(m $\cdot K$)]

k Turbulent kinetic energy. [J/kg]

L Reference length. [m]

Nu Nusselt number. [-]

P Pumping power. [(Pa $\cdot m^3)/s$]

p Corrugation pitch. [m]

p Pressure. [Pa]

P_{wet} Wet perimeter. [m]

Pr Prandtl number. [-]

q Heat transferred. [W]

r Radius. [m]

r_o Inner radius. [m]

Re Reynolds number. [-]

S Source term. [-]

T Temperature. [° C]

u, v, w Velocity cartesian components. [m/s]

V_{wet} Wet volume. [m^3]

y^+ Dimensionless distance to the wall. [-]

Subscripts

∞ Free-stream condition.

b Bulk temperature.

c Corrugated.

$conv$ Convection heat transfer.

$crit$ Critical.

e Exterior.

env Envelope.

f Fluid.

fd, h Fully developed hydrodynamically.

fd, t Fully developed thermally.

i Inlet.

i Interior.

lam Laminar.

m Mean.

M_x Momentum in x.

M_y Momentum in y.

M_z Momentum in z.

n Normal component.

o Outlet.

r, θ, z Cylindrical components.

s Smooth.

s Surface.

$turb$ Turbulent.

w Wall.

x, y, z Cartesian components.

Superscripts

’ Fluctuating component.

’ Parameter to be converted.

- Mean value.

Chapter 1

Introduction

This work will mainly focus in numerical studies of the heat transferred in different helical inward corrugated tubes with pitch and corrugation height variation. An optimized flow will also be determined from these studies.

1.1 Motivation

Nowadays there is a great demand of techniques to enhance heat exchanger tubes because they are widely used in applications such as power generation, air conditioning and food industry, among others [1, 2].

One can use three different techniques to increase the heat transfer in heat exchangers. First there is the active method which requires a power source like a vibrated flow or a surface vibration, second there is the passive method which only depends on a surface modification or extension and finally there is the compound method which is a mix of the two previous or multiple techniques of each method at the same time as rough surface with nano-fluid or fluid vibration [3].

These days, in order to get not only a smaller size heat exchanger but also effectiveness, having low cost thermal transport devices makes it necessary to use all the three techniques. Despite that the passive ones are still prefered.

1.2 Literature Review

The passive enhanced heat transfer technologies are commonly the first choice for compact heat exchangers and there are different types as for example twisted tapes [4], ribs [5], fins [6], extended surfaces [7], rough surface [8], additives [9], wire coil insert [10] and corrugations [3]. All these techniques improve the heat transferred compared with the smooth tube, however in this study the corrugated geometries will be the main subject of discussion.

The main purpose of using passive techniques is to induce swirl and vortices at the secondary flow region, which mix the fluid layers with the core flow and increase the wet area [11]. In this case Ka-

reem et al. [3] explained that the main goal of the corrugation, as similarly said for general passive techniques, is to promote the secondary recirculation flow by inducing radial velocity components, mixing the flow layers and finally, increasing the wet perimeter with holding the throat cross-section area constant, which leads to an increase of the convective surface area. It should be noted that Kareem et al. [3] paper focused on making a review of all the studies made between 1977 and 2015 about heat transfer enhancement for different types of corrugations. It shows that analysis have been made for all the regimes (laminar, transition and turbulent) and in terms of optimization it was concluded that the heat transfer is always accompanied with pressure drop which has higher values for a turbulent flow. In general the corrugated tubes have a significant improvement on heat transfer compared with the smooth tube. It is also said that the corrugation pitch and height have great influence on the flow pattern of the tested fluid and finally that helically corrugated tubes give further enhancement of heat due to the mixed effects of curvatures and corrugations.

Numerous numerical simulation and experimental studies have been made in the recent years considering various parameters such as different corrugation shapes [12, 13], the Reynolds number (Re) [14–16], the Prandtl number (Pr) [17, 18], the corrugation height [19, 20] and the corrugation pitch [21–24]. Most of the studies about corrugated tubes focused on the inward concave type [13, 15, 22, 25–29] because cold rolling the external tube surface is easier and they are more competitive in comparison to performance and cost of other enhanced techniques. This confirms that the helical corrugated tubes are the best optimization choice.

A lot of studies also focus on the liquid heat transfer process because of the higher heat transfer coefficients of denser fluids. The gas-gas heat exchangers usually have a great cost because of the metal materials and used space due to the low thermal conductivity [30]. Webb et al. [31] also suggested that the most important variables are pressure drop, heat transfer rate and flow rate in order to obtain the optimum surface geometry of the flow in the tube.

Thus, taking into account the parameters previously mentioned, helical inward corrugated tubes (Fig. 1.1) with different pitch and height will be analyzed in terms of heat transfer and pressure drop for a range of Reynolds number going from laminar to turbulent regime with a final flow optimization study.

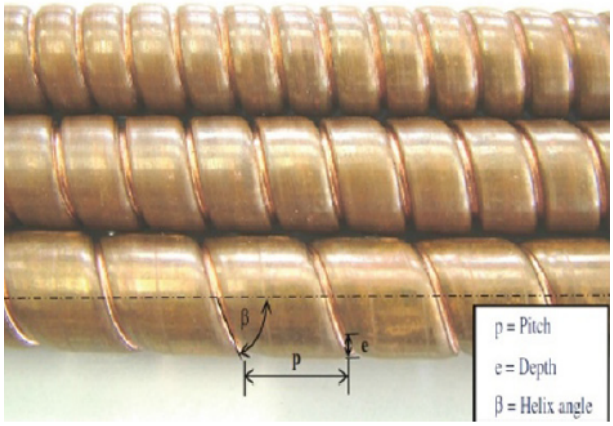

Figure 1.1: Example of inward helically corrugated tubes with different pitch used by Laohalertdecha et al. [32]

1.3 Objectives

For nine helical inward corrugated tubes with three different pitches and corrugation heights, a numerical study will be accomplished with the following goals:

- Comparison of the Nu number between the smooth tube and the corrugated tube validating the results, when possible, with the experimental data available;
- Comparison of the Darcy friction factor f between the smooth tube and the corrugated tube validating the results, when possible, with the experimental data available;
- Understand what impact the corrugation pitch and height have in the flow transition region;
- Understand how swirls are formed inside the corrugated tubes and how they enhance the heat transfer;
- Determine of the Nu augmentation factor for the different corrugated tubes compared to the smooth tube;
- Determine of the f augmentation factor for the different corrugated tubes compared to the smooth tube;
- Determine of the Thermal Performance of the corrugated tubes compared to the smooth tube;
- Determine and comparison of the Pareto efficiency curves of the nine corrugated tubes and check which are the optimum working conditions.

1.4 Thesis Outline

This work is divided in five chapters: Introduction, Background, Implementation, Results and Conclusions.

In the Introduction, to which this point also belongs, are presented some methods to improve heat exchangers and which ones are the most common and used at the industry. It is also referred the object of study in this thesis and the objectives to be accomplished for the same.

In the Background chapter it will be described the theoretical overview of the internal flow inside smooth tubes and how it is adapted to the corrugated ones. There will also be presented the governing equations used in the numerical studies and some experimental correlations that will be used as a comparison to the outcome results of the simulations.

For the Implementation chapter a discussion will be made about the CAD models used, the numerical models, how were they solved and finally a verification and validation of those models.

In the Results chapter the objectives outlined in the Introduction will be studied, compared with the experimental correlations available and discussed.

At last place there are the Conclusions in which will be described the achievements of the results obtained in this study and some suggestions for future work in this subject.

Chapter 2

Background

In this chapter, hydrodynamic and thermal considerations are presented for a common circular tube and after corrugated tubes are introduced. After that the available empirical correlations for helical corrugated tubes are presented in order to be compared with the equations available for the smooth tube and finally, the fluid flow and heat transfer model is described from the basic principles of conservation of mass, momentum and energy.

2.1 Internal Flow

It is easy to verify when there is an internal flow, such as a flow in a pipe, since its fluid is surrounded by a surface. Thus the boundary layer is incapable to develop without eventually being constrained by the walls. So it is possible to say that the internal flow configuration is a practical way for cooling and heating fluids that are used in energy conversion technologies, environmental control and chemical processing [33].

2.1.1 Hydrodynamic considerations

In an internal flow it is necessary to know about the existence of an entrance region and a fully developed region. Considering a laminar flow in a tube of radius r_o where the incoming fluid has an uniform velocity profile, the fluid interacts with the surface creating a boundary layer that develops with increasing x until the end of the hydrodynamic entry length, $x_{fd,h}$, where it merges (Fig. 2.1). Being a laminar flow the viscous effects become relevant, and after the merge of the boundary layers, they extend through all the cross section of the tube resulting in an unchangeable velocity profile with x (fully developed flow).

For the case that the boundary layer is turbulent (Fig. 2.2) the velocity profile exhibit a different shape. This boundary layer is characterized by inside unsteady swirling flows. The nominal thickness of the boundary layer is defined as the normal distance from the wall to the point where the velocity reaches 99% of the free-stream velocity. Above this point the effects of viscous stresses can then be neglected.

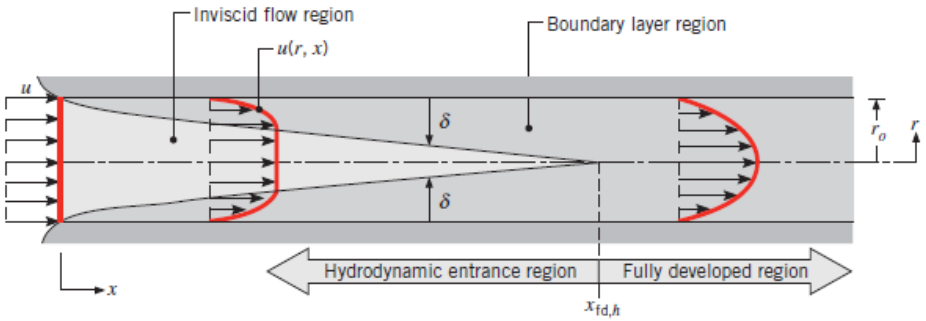

Figure 2.1: The development of a laminar hydrodynamic boundary layer in a circular tube [33]

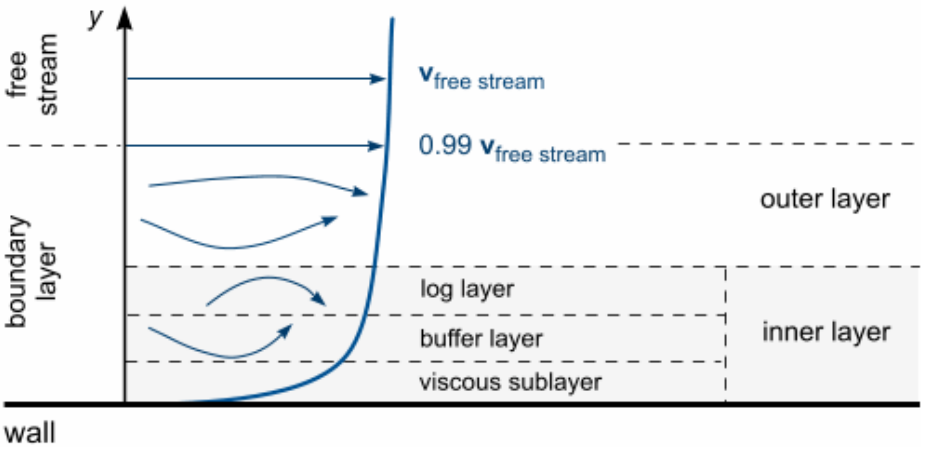

Figure 2.2: Velocity profile of a turbulent boundary layer [34]

As shown in Fig. 2.2 the turbulent boundary layer is divided into two main layers which are the outer layer and the inner layer. The outer layer is dominated by turbulent effects (inertia dominated core flow far from wall) and it is free from direct viscous effects. In the other hand the inner layer (10 to 20% of the total thickness of the wall layer) can be split up into three more sublayers which are the viscous sub-layer, buffer layer and log layer. In the viscous sublayer the fluid layer in contact with the wall is dominated by viscous effects and is almost laminar (diffusion predominance). The mean flow velocity only depends on the fluid density, viscosity, distance from the wall and the wall shear stress, presenting a nearly linear velocity profile. The buffer layer is a transitional layer between the viscous sublayer and the log layer where diffusion and turbulent mixing are comparable. Finally there is the turbulent log layer which is dominated by turbulent effects.

Resuming the analysis of Fig. 2.1 it it possible to say that the size of the entry region depends on the laminar or turbulent regime of the flow which can be determined by the Reynolds number

$$Re_D = \frac{u_m D}{\nu} \tag{2.1}$$

where

$$u_m = \frac{\dot{m}}{\rho A_c} \tag{2.2}$$

The Re_D represents the ratio between inertial forces and viscous forces, having a higher or lower number depending if inertial forces or viscous forces are more predominant respectively. Also in equation 2.1, the u_m refers to the mean fluid velocity over the tube cross section A_c, D is the tube diameter (which is $D = D_i$ for a circular tube) and ν is the kinematic viscosity of the fluid. In equation 2.2, $\dot{m}$ corresponds to the mass flow rate.

The critical Reynolds number at what turbulence effects start to be noticed is

$$Re_{D,crit} \approx 2300 \tag{2.3}$$

yet higher Reynolds numbers are needed in order to have fully turbulent conditions ($Re_D \approx 10000$).

As said by Bergman et al. [33], for a laminar flow ($Re_D \lesssim 2300$), the hydrodynamic entry length can be expressed as

$$\left(\frac{x_{fd,h}}{D}\right)_{lam} \approx 0.05 Re_D \tag{2.4}$$

assuming that the fluid enters the tube from a rounded converging nozzle and that the velocity profile at the entrance is practically uniform (Fig. 2.1). And for the turbulent flow, despite not having an optimal general expression for the entry length, it is known that it is approximately independent of the Reynolds number and as a first approximation can be represented as

$$10 \lesssim \left(\frac{x_{fd,h}}{D}\right)_{turb} \lesssim 60 \tag{2.5}$$

assuming fully developed turbulent flow at $\left(\frac{x}{D}\right) > 10$. As said by Cruz [35] and [36], in a more recent study, one the development of turbulent flow inside a pipe have been made by Doherty et al. [37] and they proposed that the turbulent fully developed entry length was a little bit longer and expressed as

$$\left(\frac{x_{fd,h}}{D}\right)_{turb} \lesssim 80 \tag{2.6}$$

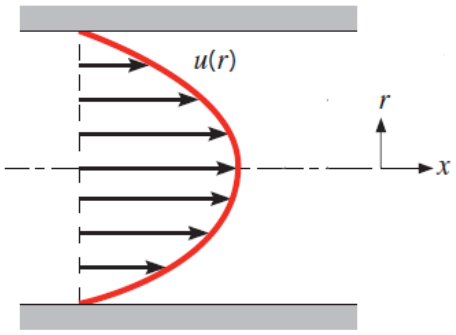

Figure 2.3: Velocity profile for a laminar flow inside a circular tube [33]

The velocity profile of the circular tube can be obtained solving the $x-$momentum equation. Therefore, for a laminar, incompressible, constant property fluid flow in the fully developed region the profile becomes

$$\frac{u(r)}{u_m} = 2\left[1 - \left(\frac{r}{r_o}\right)^2\right] \tag{2.7}$$

As it is possible to verify through equation 2.7 and Fig. 2.3 the fully developed velocity profile inside the tube is parabolic where u_m can be determined knowing the mass flow rate.

Nowadays, for engineering purposes, it is also important to know the pressure drop for a sustainable internal flow since this quantity can be used to obtain the fan or pump power requirements. The Darcy friction factor is a dimensionless parameter that can be written in terms of the pressure drop as

$$f \equiv \frac{-2\left(\frac{\partial p}{\partial x}\right)D}{\rho u_m^2} \tag{2.8}$$

and it leads to the Darcy-Weisbach equation which reorganized in order to f yields

$$f = \frac{2D}{\rho u_m^2}\left(\frac{\Delta p}{L}\right) \tag{2.9}$$

where Δp is the pressure drop, ρ is the material density, L the reference length of the tube and $\frac{\Delta p}{L}$ is the pressure loss per unit length. From this, for a fully developed laminar flow the equation 2.8 (Hagen-Poiseuille equation) becomes

$$f = \frac{64}{Re_D} \tag{2.10}$$

For a fully developed turbulent flow it is difficult to obtain good correlations once not only there is dependence on the Reynolds number but also on the surface condition (roughness) and therefore empirical correlations are used.

Considering a smooth tube, Petukhov et al. [38] found the following correlation

$$f = (0.79\ln Re_D - 1.64)^{-2} \qquad 3000 \lesssim Re_D \lesssim 5\cdot 10^6 \tag{2.11}$$

Many other studies have been made throughout the years about horizontal tubes in order to obtain friction factor correlations for different flow regimes and Tam et al. [39] made a compilation of the most important. So from their work, for an isothermal transition fully developed flow Hrycak and Andrushkiw [40] found the following correlation

$$f = 4(-3.1\times 10^{-3} + 7.125\times 10^{-6}Re_D - 9.7\times 10^{-10}Re_D^2) \qquad 2100 < Re < 4500 \tag{2.12}$$

There is also the Blasius correlation [41] for the turbulent fully developed flow for the smooth tube which is a simpler way to compute the Darcy friction factor since it has no term for pipe roughness

$$f = 0.3164 Re_D^{-0.25} \tag{2.13}$$

Both equations, 2.12 and 2.13, have a multiplicative factor 4 associated in order to be in accordance with the friction factor equation 2.10 that comes from the Darcy-Weisbach equation.

Knowing the pressure drop one can finally determine the fan or pumping power necessary to overcome the resistance to the flow related to this pressure drop. By this definition it is possible to obtain

$$P = (\Delta p)\dot{V} \tag{2.14}$$

where $\dot{V} = \frac{\dot{m}}{\rho}$ and it represents the volumetric flow rate for an incompressible fluid.

2.1.2 Thermal considerations

Now for the same circular tube that was showed in Fig. 2.1, if it is considered that the incoming fluid has a uniform temperature $T(r,0)$ being this one less than the surface temperature ($T_s > T(r,0)$), by Fig. 2.4 it is possible to see the development of the thermal boundary layer due to the convection heat transfer that occurs.

There are two surface conditions that can be imposed in the tube which are the uniform temperature (T_s is constant) or a uniform heat flux (q_s'' is constant). This last one will be considered in this work and over again mentioned in the implementation chapter. By choosing one or another fixed condition the thermally fully developed flow can be achieved, however, the shape of the fully developed temperature profile $T(r,x)$ becomes different.

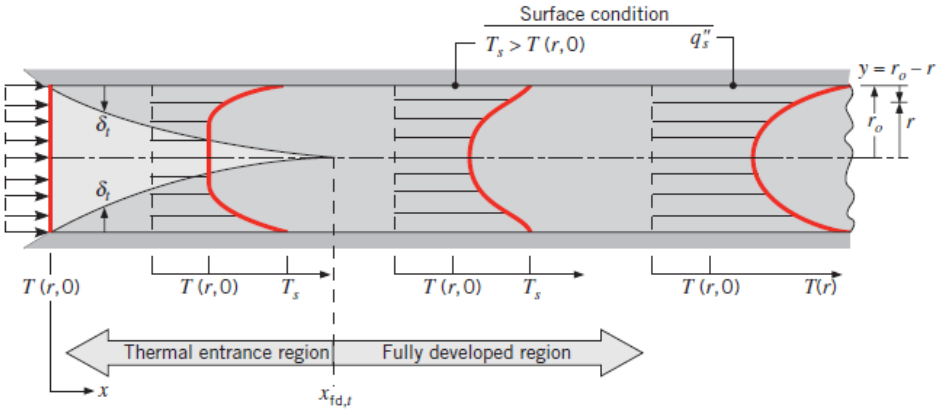

Figure 2.4: The development of the thermal boundary layer in a heated circular tube [33]

One can also realize that for both surface conditions, the amount by which fluid temperatures exceed the entrance temperature increases with increasing x.

In this case, for a laminar flow, Bergman et al. [33] says that Kays et al. [42] defined a thermal entry length as

$$\left(\frac{x_{fd,t}}{D}\right)_{lam} \approx 0.05 Re_D Pr \tag{2.15}$$

where Pr is the Prandtl number which can be defined as the ratio between the momentum diffusivity

and thermal diffusivity and can be represented as

$$Pr = \frac{c_p \mu}{k} \tag{2.16}$$

where c_p is the specific heat, μ the dynamic viscosity and k the thermal conductivity of the fluid.

Comparing the equations 2.4 and 2.15 for laminar conditions, it is possible to observe that if $Pr < 1$, the hydrodynamic boundary layer develops slower than the thermal boundary layer ($x_{fd,h} > x_{fd,t}$), if $Pr > 1$ the opposite happens ($x_{fd,h} < x_{fd,t}$) and for $Pr = 1$, the boundary layers are approximately equal in extent. In this work and as it will be discussed in the implementation section, the fluid that is being used is water, which for 300K has $Pr = 5.83$ [33]. Thus, the momentum diffusivity is 5.83 times bigger than the thermal diffusivity and therefore the hydrodynamic boundary layer will developed around 6 times faster than the thermal one.

After all, Cruz [35] stated in his work that studies have been made by Meyer and Everts [43] in smooth circular tubes with constant heat flux surface condition and they found out that a longer thermal entry length is needed when the flow is simultaneously hydrodynamically and thermally developing comparing to when the flow is hydrodynamically fully developed and thermally developing. Therefore, as shown in equation 2.17 a coefficient of at least 0.12 must be considered compared to the initial 0.05 indicated above in equation 2.15.

$$\left(\frac{x_{fd,t}}{D}\right)_{lam} \approx 0.12 Re_D Pr \tag{2.17}$$

One can easily realize that the Prandtl number has a great influence on the laminar thermal entry length ($x_{fd,t}$ grows with Pr) however for a turbulent flow the conditions are almost independent of Pr and the following approximation can be done [33]

$$\left(\frac{x_{fd,t}}{D}\right)_{turb} \approx 10 \tag{2.18}$$

It is known that to describe an internal flow, in case there is absence of a free stream velocity (u_∞), a mean velocity is needed. In a similar way, a mean temperature (bulk temperature) is needed if there is absence of a fixed free stream temperature (T_∞). Therefore, in order to obtain the mean temperature definition, first equation 2.19 must be evaluated

$$q = \dot{m} c_p (T_o - T_i) \tag{2.19}$$

where the right side terms represent the thermal energy for an incompressible liquid or the enthalpy (flow work plus thermal energy) for an ideal gas which is transported by the fluid. Knowing that there is convection, the mean temperature T_m can be determined through an equation where $\dot{m} c_p T_m$ is equal to the rate of thermal energy (or enthalpy) advection integrated over the cross section and may be presented as

$$\dot{m} c_p T_m = \int_{A_c} \rho u c_p T \, dA_c \tag{2.20}$$

where ρu is the mass flux inside the circular tube and $c_p T$ is the thermal energy (or enthalpy) per unit

mass, being ρ and c_p constant fluid properties.

After knowing T_m one can define the Newton's law of cooling

$$q_s'' = h(T_s - T_m) \tag{2.21}$$

where h is the local convection heat transfer coefficient and T_s is the surface temperature. It is important to realize that T_m is as much as a good reference temperature for internal flows as T_∞ is for external flows yet they have a crucial difference. If the flow direction is considered, T_∞ remains constant while T_m vary in this direction. That happens because $\frac{\partial T_m}{\partial x} \neq 0$ when heat transfer occurs. T_m increases with x if the heat transfer is from the surface to the fluid ($T_s > T_m$) and decreases with x if the opposite happens ($T_s < T_m$).

As previously said, if there is heat transfer neither $\frac{\partial T_m}{\partial x}$ or $\frac{\partial T}{\partial x}$ get to zero for any radius r. That being said, in order to obtain thermally fully developed conditions one must define an adimentional temperature difference as $(T_s - T)/(T_s - T_m)$. Despite the change of the temperature profile $T(r)$ with x, the profile's shape no longer changes and finally it is possible to state that the flow is thermally fully developed and its condition can be presented as

$$\frac{\partial}{\partial x}\left[\frac{T_s(x) - T(r,x)}{T_s(x) - T_m(x)}\right]_{fd,t} = 0 \tag{2.22}$$

where the tube's surface temperature is T_s, the local fluid temperature is T and the mean temperature of the fluid over the cross section of the tube is T_m. This condition is achieved with either an uniform surface temperature or an uniform surface heat flux. From equation 2.22 one can also conclude that the local convection coefficient is constant and independent of the x direction from the point where the thermally fully developed conditions are reached ($x_{fd,t}$) as demonstrated in Fig. 2.5 bellow, which is defined by equation 2.23 as

$$\frac{h}{k} \neq f(x) \tag{2.23}$$

Note that constant fluid properties are considered.

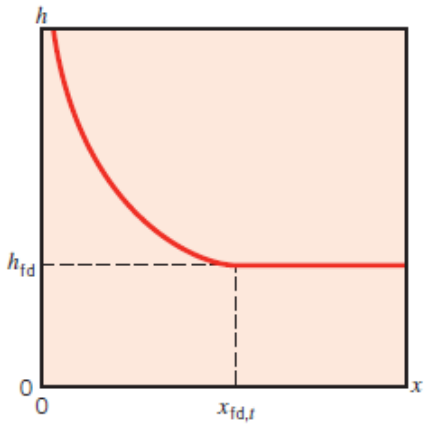

Figure 2.5: Convection heat transfer coefficient variation with x in a circular tube [33]

Through the same figure one can also notice that equation 2.22 does not satisfy the thermal entrance region, where h changes with x. That happens because the thermal boundary layer thickness at the tube entrance is zero and therefore the h is too high at $x = 0$, beginning to decay as soon as the thermal boundary layer starts to develop until the point $x_{fd,t}$ from where it stabilizes at said above.

Knowing that the tube in Fig. 2.4 is fully enclosed, parameters as the mean temperature along x and the total convection heat transfer (q_{conv}) related to the inlet and outlet temperature difference can be determined through an energy balance. To solve this problem usually some assumptions are made. For example it is common to neglect the viscous dissipation and consider that the fluid can be modeled as an incompressible liquid or as an ideal gas with negligible pressure variation. The net heat transfer by conduction in the axial direction is also reasonable to neglect, hence, equation 2.19 will only depend on q_{conv} and after rewriting it, for a tube of finite length it yields

$$q_{conv} = \dot{m} c_p (T_{m,o} - T_{m,i}) \tag{2.24}$$

where $T_{m,o}$ is the mean temperature in the outlet and $T_{m,i}$ is the mean temperature at the inlet.

As previously mentioned in this work a uniform surface heat flux on the tube will be considered. Being q_s'' independent of the axial direction, the total heat transfer rate can be written as

$$q_{conv} = q_s''(P \cdot L) \tag{2.25}$$

where P is the tube's inner surface perimeter and L the length of the tube.

For this surface condition there is also

$$\frac{dT_m}{dx} = \frac{q_s'' P}{\dot{m} c_p} \neq f(x) \tag{2.26}$$

which integrated from $x = 0$ yields

$$T_m(x) = T_{m,i} + \frac{q_s'' P}{\dot{m} c_p} x \tag{2.27}$$

for a constant heat flux.

Through equation 2.27 one can easily verify on Fig. 2.6 that the mean temperature has a linear variation with x and in the same figure, the variation of $(T_s - T_m)$ from equation 2.21 can also be analyzed. As h decreases fast in the beginning of the thermal entry length (Fig. 2.5) the temperature difference starts to rise quickly until a certain point where it begins to stabilize due to h lower variation. As previously said, when the the point $x_{fd,t}$ is reached, thermally fully developed conditions are achieved, so h becomes constant and in turn the temperature difference $(T_s - T_m)$ becomes constant as well.

In order to determine the convection coefficient, a balance between radial conduction and axial advection should be done, which after some rearrangements yields

$$T_m(x) - T_s(x) = -\frac{11}{48} \frac{q_s'' D}{k} \tag{2.28}$$

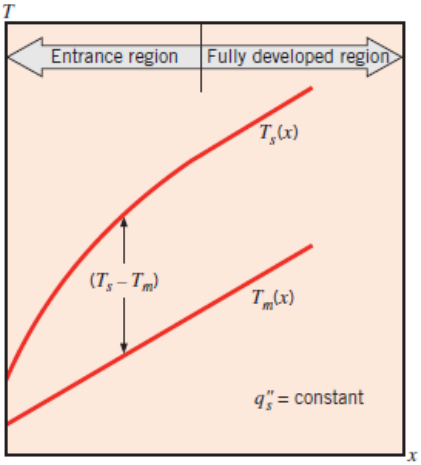

Figure 2.6: Axial temperature variations for a circular tube with uniform surface heat flux [33]

which combined with equation 2.21 (Newton's law of cooling) gives

$$Nu_D = \frac{hD}{k} = 4.36 \tag{2.29}$$

The equation 2.29 is a theoretical result for a laminar, incompressible, constant property fluid flow in fully developed conditions inside a circular tube and uniform surface heat flux. In this equation h is the convective heat transfer coefficient, D is the tube inner diameter and k is the fluid thermal conductivity. Together they form the Nusselt number (Nu_D) which represents the ratio between the heat transferred by convection and the heat transferred by conduction. It is easy to realize that for these conditions the Nu_D is constant and independent of Pr, Re_D and axial direction.

In 1976 Gnielinski [44] determined a correlation for a turbulent fully developed flow (thermally and hydrodynamically) inside a circular tube, also valid for the transition region and which in a simplified form yields

$$Nu_D = \frac{(f/8)(Re_D - 1000)Pr}{1 + 12.7(f/8)^{1/2}(Pr^{2/3} - 1)} \qquad 0.5 \lesssim Pr \lesssim 2000 \quad , \quad 3000 \lesssim Re_D \lesssim 5 \cdot 10^6 \tag{2.30}$$

where the friction factor can be obtained from equation 2.11 or the Moody diagram.

In a more recent work in 2013 [45], a linear interpolation between Nusselt numbers ranging from $Re = 2300$ to 4000 was made in order to close the gap that existed at the transition region ($Re = 2300$) and the following correlation was presented

$$Nu_{corr} = Nu_{exp} \left(\frac{4,5}{Pr}\right)^{0.42} \left(\frac{Pr_w}{Pr}\right)^{0.11} \qquad 1000 < Re < 15000 \tag{2.31}$$

where the experimental Nusselt numbers determined are normalized by the factor of $(4.5/Pr)^{0.42}$ and finally corrected by $(Pr/Pr_w)^{0.11}$ for the temperature dependence of the physical properties (fluid Prandtl Pr and wall Prandtl Pr_w).

By the end of year 2020 Ammar and Park [46] also made a research to validate the Gnielinski

correlation in order to evaluate the heat transfer coefficient of enhanced tubes by a non-linear regression model. They start by saying that despite equation 2.30 being an accurate correlation for transition and turbulent flow it has an error of $\pm 20\%$ for 90% of the data that was based on 800 experimental data points. After some studies the following correlation was proposed

$$Nu_{new} = 0.3Re^{0.22}\left[\frac{(f/8)(Re-1000)Pr}{1+12.7(f/8)^{1/2}(Pr^{2/3}-1)}\left(1+\left(\frac{D_i}{L}\right)^{2/3}\right)\left(\frac{Pr}{Pr_w}\right)^{0.11}\right]^{0.77}_{Gnielinski} \tag{2.32}$$

which is valid for $Re = 8500 - 12500$ for heating fluid conditions. As is it possible to see this correlation introduces an extra Reynolds number term and the correlation suggest the enhanced tube results well with an agreement within $\pm 5\%$, being the total mean error equal to 2.1%. In this equation D_i and L are the inner tube diameter and the tube length respectively.

2.1.3 Corrugated tubes

Despite all the circular tube studies, as above described, non-circular tubes, especially corrugated tubes, have brought a lot of interest to researchers especially because they involve convection transport and are being more used in compact heat exchangers. In order to compare circular tubes with the helically corrugated ones, an effective diameter (characteristic length) should be defined. Therefore, not only Bergman et al. [33] but also Yang et al. [47], Ajeel et al. [48], Wang et al. [49] among others, define so this called hydraulic diameter D_h as

$$D_h = \frac{4A_c}{P_{wet}} \tag{2.33}$$

where A_c is the flow cross section area and P_{wet} corresponds to the wet perimeter of the same. For a circular tube $D_h = D_i = D$.

With this parameter one can redefine the Reynolds number in equation 2.1 as

$$Re = \frac{u_m D_h}{\nu} \tag{2.34}$$

The Darcy-Weisbach equation 2.9 and the Nusselt number equation 2.29 also become respectively

$$f = \frac{2D_h}{\rho u_m^2}\left(\frac{\Delta p}{L}\right) \tag{2.35}$$

$$Nu = \frac{hD_h}{k} \tag{2.36}$$

The helically corrugated tube, as shown in figure 2.7 and as already said, is one of the tubes used to enhance heat transfer. As it is possible to see the main parameters that describe the tube are the pitch p and the corrugation height e. For constant exterior and interior diameter, D_e and D_i respectively, and for a certain Re, the pitch and the corrugation height will be the ones to set the flow transition, the heat being transferred and the friction factor associated.

Based on these parameters, researchers tried to find out correlations that could better describe the

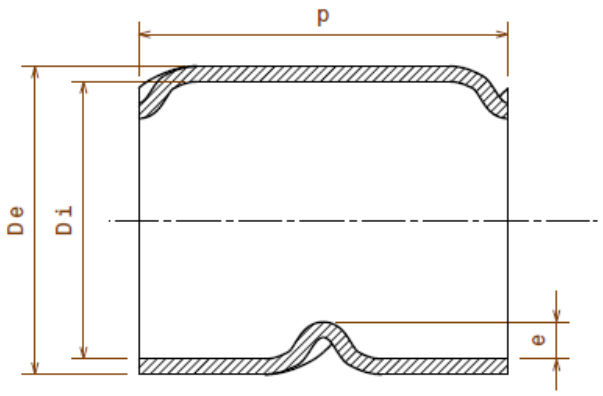

Figure 2.7: 2D section view of a corrugated tube

flow in different regimes inside helically corrugated tubes.

In 2004 Vicente et al. [17, 50] presented two papers. In both of them the results were obtained for $Re' = f(D_i)$ and $Nu' = f(D_i)$. In order to the results to be in agreement with the new equations (2.34 and 2.36) outlined for the corrugated tubes, the following conversion can be done, $Re' = (D_i/D_h)Re$ and $Nu' = (D_i/D_h)Nu$, so that the correlations proposed can be $Re = f(D_h)$ and $Nu = f(D_h)$.

So the first paper [50] was an experimental investigation about laminar and transition flow at 10 horizontal helically corrugated tubes, where water and ethylene glycol were used as test fluids. From their work they came out with a laminar flow friction factor correlation that can be expressed as

$$f = 119.6(Re')^{-0,97}\phi^{0,11} \tag{2.37}$$

where the equation was multiplied by 4 in order to agree with the Darcy friction factor. That happens because Vicente et al. [50] presented their results on Fanning friction factor basis. In this equation ϕ represents a dimensionless factor called severity index factor which can be defined as

$$\phi = \frac{e^2}{pD_i} \tag{2.38}$$

So the severity index factor relates the most important parameters that describe a corrugated tube, as shown at Fig. 2.7, and at the same time, it establishes how roughness can influence the flow. It is said that equation 2.37 correlates 95% of the experimental data within 5% and that for a certain ϕ the friction factor increased between $5 - 25\%$.

At [50] it was also determined a critical Reynolds number based on the study of 10 corrugated tubes leading to the following correlation

$$Re'_{crit} = 2100\left[1 + 1.18 \cdot 10^7 \left(\frac{e}{D_i}\right)^{3.8}\right]^{-0.1} \tag{2.39}$$

which has a 15% accuracy on its values.

For the heat transferred, a Nusselt number correlation was also determined. However, in [50], the flow had a mixed convection heat transfer where the Nusselt number depended not only on the natural

convection but also on the entry region. In this work, heat transferred by forced convection is predominant, especially because of the small size of the tubes being used ($D_i = 4.5mm$). Therefore, their solution for laminar Nu' cannot be considered.

The second paper [17] was also an experimental research about the same 10 horizontal hellically corrugated tubes with the same test fluids and flow conditions of $Re' = 2000 - 90000$ and $Pr = 2.5 - 100$. The purpose of this work was to obtain the heat transfer and isothermal friction characteristics of the tubes. From all the tubes tested, 600 points were correlated to experimentally determine the following generalized friction factor correlation for a turbulent flow

$$f = 6.12(Re')^{-0.16}\phi^{0.46} \tag{2.40}$$

which has a 7% deviation for 95% of the experimental friction data for $Re' = 8000 - 60000$. Once again, the obtained friction factor was multiplied by 4 to be in agreement with the Darcy friction factor. For $Re' = 2000 - 8000$ Vicente et al. [17] recommend that equation 2.40 should only be used for tubes of $\phi < 10^{-3}$ (soft corrugation). For the case that $\phi > 10^{-3}$ (medium-high corrugation) a constant friction factor evaluated with 2.40 at $Re' = 8000$ should be used. By following these recommendations make estimated error stay within $\pm 10\%$. It is also said that equation 2.40 can still be used for $Re' > 60000$ however the predicted friction factor values will be 16% higher than the experimental ones.

For the heat transfer results, 800 points were also experimentally correlated to obtain the following generalized Nusselt number correlation for a turbulent flow

$$Nu' = 0.3741(Re' - 1500)^{0.74}\phi^{0.25}Pr^{0.44} \tag{2.41}$$

which is valid for $Re' > 2000$ and correlates 95% of the empirical data within 14% deviation. Vicente et al. [17] also say that for an increasing Pr the heat transferred by corrugated tubes is higher (compared to smooth tubes).

There is not much research made in the laminar regime so this part lacks of correlations. One of the last works published, besides Vicente et al. [50] was by Barba et al. [28] in 2002. It was also an experimental investigation to determine the pressure drop and heat transfer in the corrugated tube with constant heat flux for $100 < Re < 800$ where the test fluid was ethylene glycol in steady forced convection. Being that said, after fitting the experimental data, for a periodically fully developed region, an isothermal friction factor correlation could be found

$$f = 61.639(Re')^{-0.8602} \tag{2.42}$$

which already agrees with the Darcy friction factor. For the same developed region the Nusselt number correlation obtained was

$$Nu' = 0.7345(Re')^{0.6589}Pr^{0.0374} \tag{2.43}$$

in which the maximum relative difference between the experimental data and the correlations results

was 5%. By looking at the exponent factors in equation 2.43 it is noticeable that for an increasing Re the heat transfer enhancement is higher than for an increasing Pr. Both equations 2.42 and 2.43 depend on $Re' = f(D_{env}) = f(D_i)$. So the same conversion can be done ($Re' = (D_i/D_h)Re$ and $Nu' = (D_i/D_h)Nu$) as used for Vicente correlations. However, correlation 2.43 only stands for the corrugated tube analyzed in Barba's experiment (Fig. 2.8) which is a little bit different from the ones considered in this work (Fig. 1.1). Therefore, and as already said, as laminar regime lacks of empirical correlations for the helical corrugated tubes, the equations 2.42 and 2.43 should only be used as a first order approximation. Note that using this correlations for the helical corrugated tubes can compromise the precision of the estimated results.

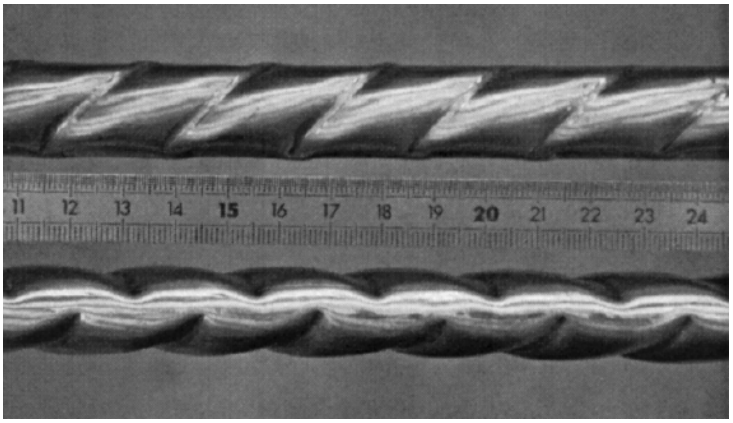

Figure 2.8: Front view (upper tube) and side view (lower tube) of Barbas's corrugated tube [28]

Later, in 2011, Pethkool et al. [51] made an experimental investigation for nine tubes (3 different corrugation heights and pitches) to evaluate the thermal performance, heat transfer enhancement and friction factor for a turbulent flow, employing water as a test fluid. The following empirical correlations were obtained

$$f = 1.15Re^{-0.239}\left(\frac{e}{D_h}\right)^{0.179}\left(\frac{p}{D_h}\right)^{0.164} \qquad 5500 < Re < 60000 \tag{2.44}$$

$$Nu = 1.579Re^{0.639}Pr^{0.3}\left(\frac{e}{D_h}\right)^{0.46}\left(\frac{p}{D_h}\right)^{0.35} \qquad 5500 < Re < 60000 \tag{2.45}$$

from which they came to a conclusion that the ratio (e/D_h) is an important factor that dominates the magnitude of the Nusselt number while the (p/D_h) ratio it is only dominant for the friction factor. In general, one should notice that the (e/D_h) ratio has a higher effect than the (p/D_h) ratio. Finally, the validation of these correlations demonstrated that the average deviations of the multiple regressions of the friction factor and the Nusselt number are within $\pm 4\%$ and $\pm 9\%$ respectively.

2.2 Governing equations of fluid flow and heat transfer

As said by Versteeg and Malalasekera [52] the governing equations of fluid flow constitute the mathematical statements of the conservation laws of physics which claim that the mass of a fluid is conserved,

the rate of change of momentum equals the sum of the forces on a fluid particle (Newton's second law) and that the rate of change of energy is equal to the sum of the rate of heat.

The fluid can be approximated as a continuum if it is assumed that the density of the fluid is high enough considering that an infinitesimally small element (in the sense of differential calculus), Fig. 2.9, of the fluid contains a sufficient number of particles, for which we can specify mean velocity and mean kinetic energy. Thus it is possible to define velocity, pressure, temperature, density, and other important quantities at each point of the fluid [53].

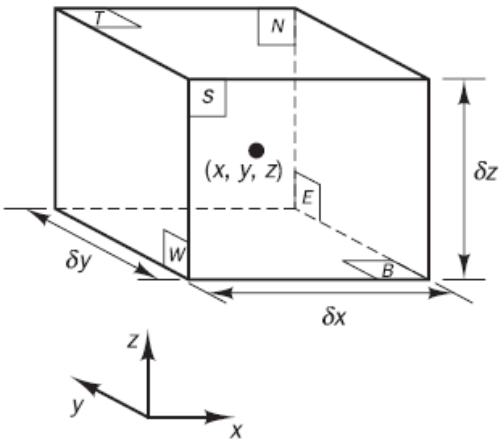

Figure 2.9: Infinitesimal fluid element [52]

2.2.1 Continuity equation

In order to obtain the mass conservation equation one must consider the mass balance for the fluid element which implies that the rate of increase of mass in the fluid element is equal to the net rate of flow of mass into the fluid element. From this balance it is possible to obtain the following expression in a compact vector notation

$$\frac{\partial \rho}{\partial t} + div(\rho \mathbf{u}) = 0 \tag{2.46}$$

which in a longhand notation yields

$$\frac{\partial \rho}{\partial t} + \frac{\partial (\rho u)}{\partial x} + \frac{\partial (\rho v)}{\partial y} + \frac{\partial (\rho w)}{\partial z} = 0 \tag{2.47}$$

The equation 2.46 is used for unsteady, three dimensional and compressible fluid flows being the left hand side the rate of change in time of the density (mass per unit volume) and the second term the net flow of mass out of the element across its boundaries (convective term). However in this work, and as it will be described in the Implementation chapter, it is assumed an incompressible flow. This means that the density is constant and the equation 2.46 becomes

$$div(\mathbf{u}) = 0 \tag{2.48}$$

and in a longhand notation

$$\frac{\partial u}{\partial x} + \frac{\partial v}{\partial y} + \frac{\partial w}{\partial z} = 0 \tag{2.49}$$

2.2.2 Momentum equations

For the momentum equations it is necessary to recall the Newton's second law which states that the rate of increase of momentum of a fluid particle is equal to the sum of forces on that fluid particle. That being said, it is possible to obtain the following momentum equations for a compressible flow for the three reference directions (x,y,z) in a compact vector notation

$$\frac{\partial(\rho u)}{\partial t} + div(\rho u \mathbf{u}) = -\frac{\partial p}{\partial x} + div(\mu \nabla u) + S_{Mx} \tag{2.50}$$

$$\frac{\partial(\rho v)}{\partial t} + div(\rho v \mathbf{u}) = -\frac{\partial p}{\partial y} + div(\mu \nabla v) + S_{My} \tag{2.51}$$

$$\frac{\partial(\rho w)}{\partial t} + div(\rho w \mathbf{u}) = -\frac{\partial p}{\partial z} + div(\mu \nabla w) + S_{Mz} \tag{2.52}$$

These equations are commonly called as the Navier-Stokes equations and they can be adapted in different ways. In this case, as previously said, it was considered an incompressible flow and it is assumed a Newtonian fluid, in which the viscous stresses are proportional to the rates of deformation. Therefore the viscosity is constant and the equations become

$$\rho\left(\frac{\partial u}{\partial t} + u\frac{\partial u}{\partial x} + v\frac{\partial u}{\partial y} + w\frac{\partial u}{\partial z}\right) = \rho g_x - \frac{\partial p}{\partial x} + \mu\left(\frac{\partial^2 u}{\partial x^2} + \frac{\partial^2 u}{\partial y^2} + \frac{\partial^2 u}{\partial z^2}\right) \tag{2.53}$$

$$\rho\left(\frac{\partial v}{\partial t} + u\frac{\partial v}{\partial x} + v\frac{\partial v}{\partial y} + w\frac{\partial v}{\partial z}\right) = \rho g_y - \frac{\partial p}{\partial y} + \mu\left(\frac{\partial^2 v}{\partial x^2} + \frac{\partial^2 v}{\partial y^2} + \frac{\partial^2 v}{\partial z^2}\right) \tag{2.54}$$

$$\rho\left(\frac{\partial w}{\partial t} + u\frac{\partial w}{\partial x} + v\frac{\partial w}{\partial y} + w\frac{\partial w}{\partial z}\right) = \rho g_z - \frac{\partial p}{\partial z} + \mu\left(\frac{\partial^2 w}{\partial x^2} + \frac{\partial^2 w}{\partial y^2} + \frac{\partial^2 w}{\partial z^2}\right) \tag{2.55}$$

where the rate of increase of x-, y- and z- momentum per unit volume of fluid particle is given by the terms on the left side. On the right side the first term represents the gravitational forces, the second term represents the pressure forces and at last the viscous forces. The contributions of these three surface forces are usually separated terms in the momentum equation and if there are any effects from body forces (centrifugal force, Coriolis force and electromagnetic force) they should be presented as source terms (S_{Mx}, S_{My} and S_{Mz}) [52].

2.2.3 Energy equation

The energy equation can be obtained from the first law of thermodynamics which claims that the rate of increase of energy of a fluid particle is equal to the sum of the net rate of heat added to the fluid particle and the net rate of work done on the same. Versteeg and Malalasekera [52] also say that the energy of

a fluid is commonly defined as the sum of internal (thermal) energy i, kinetic energy $\frac{1}{2}(u^2+v^2+w^2)$ and gravitational potential energy. This definition points that the fluid element stores gravitational potential energy and in this case, its effects will be included as a source term, giving the following energy equation

$$\rho\frac{DE}{Dt} = -div(p\mathbf{u}) + \left[\frac{\partial(u\tau_{xx})}{\partial x} + \frac{\partial(u\tau_{yx})}{\partial y} + \frac{\partial(u\tau_{zx})}{\partial z} + \frac{\partial(v\tau_{xy})}{\partial x} + \frac{\partial(v\tau_{yy})}{\partial y} + \frac{\partial(v\tau_{zy})}{\partial z} + \frac{\partial(w\tau_{xz})}{\partial x} + \frac{\partial(w\tau_{yz})}{\partial y} + \frac{\partial(w\tau_{zz})}{\partial z}\right] + div(k\nabla T) + S_E \quad (2.56)$$

where there is $E = i + \frac{1}{2}(u^2+v^2+w^2)$. The left side term represents rate of increase of energy of a fluid particle per unit volume, the first two terms of the right side represent the total rate of work done on the fluid particle by surface stresses, the third term represents the rate of heat addition to the fluid particle due to heat conduction across element boundaries and the last one is the energy source term. Despite equation 2.56 being an adequate energy equation it is preferable to extract the changes of the (mechanical) kinetic energy in order to get an equation for the internal energy i or temperature T. Thus, by rearrangement it is possible to obtain the following internal energy equation by the Newtonian model

$$\frac{\partial(\rho i)}{\partial t} + div(\rho i\mathbf{u}) = -p\,div(\mathbf{u}) + div(k\nabla T) + \Phi + S_i \quad (2.57)$$

where the effects due to viscous stresses are described by the dissipation function

$$\Phi = \mu\left(2\left[\left(\frac{\partial u}{\partial x}\right)^2 + \left(\frac{\partial v}{\partial y}\right)^2 + \left(\frac{\partial w}{\partial z}\right)^2\right] + \left(\frac{\partial u}{\partial y} + \frac{\partial v}{\partial x}\right)^2 + \left(\frac{\partial u}{\partial z} + \frac{\partial w}{\partial x}\right)^2 + \left(\frac{\partial v}{\partial z} + \frac{\partial w}{\partial y}\right)^2\right) + \lambda(div\,\mathbf{u})^2 \quad (2.58)$$

For this case, as it is considered an incompressible fluid $i = cT$, where c is the specific heat and $div\,\mathbf{u} = 0$.

Chapter 3

Implementation

In this section, at first, it will be described how the geometries to be analyzed were obtained and after the numerical model will be discussed in terms of the different assumptions made and the physics used to do the analysis. In the end, the verification and validation process will be introduced.

3.1 3D CAD geometry

In order to do a numerical simulation, first, one must define the simulation domain. So using the 3D CAD (Computer-Aided Design) modeling software available by STAR-CCM+ [34] it was possible to create 9 geometries for the corrugated tubes and one for the smooth tube for comparison. As shown at Fig. 3.1 only the flow region inside the tubes was considered for the domain. As $D_e = 5$ mm and $D_i = 4.5$ mm were the outer and the inner diameter used for the tubes in this study (the same diameters as Cruz [35] used) the wall thickness of the tubes was neglected. This will be better discussed at the numerical model chapter after enumerating all the numerical assumptions made.

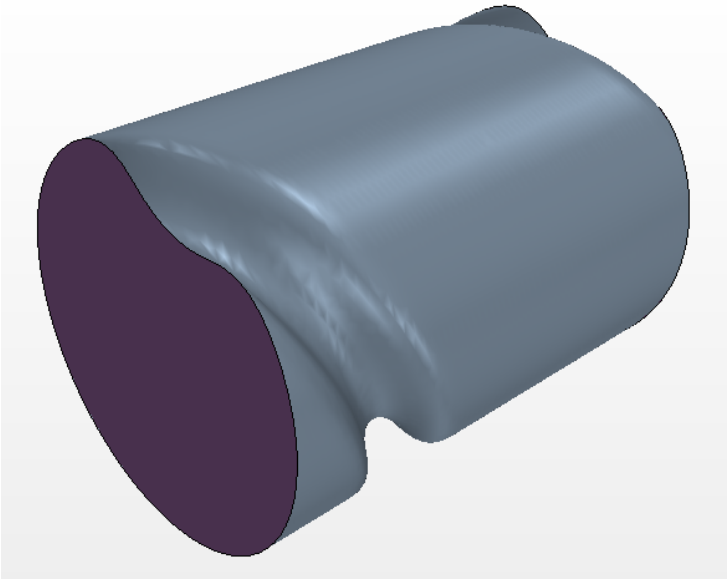

Figure 3.1: Isometric view of the corrugated tube with $p = 6$ mm and $e = 0.6$ mm

The tubes could be created by another modeling software however to avoid import errors all of them were made in the same software that will run the simulations.

As it was mentioned in the topic overview, the corrugated tubes are manufactured by cold rolling the surface of the circular tube and because of that, as it may be seen in Kareem et al. [3] review paper on the corrugations, the focus is most of the times placed only in the mid section (Fig. 2.7). However, when the geometry is created in a modeling software it must have a different approach. In this case, in order to create the corrugated tubes, the cross section was drawn at first (Fig. 3.2). After that the section was revolved 360 degrees with a sweep command through a guiding line that has the length of the pitch. As the tubes geometry repeats itself every pitch (periodic conditions), the length of the tube is always the same size of the pitch considered. The pitches considered in this study (6 mm, 9 mm and 12 mm) can be changed by changing the guide line length .

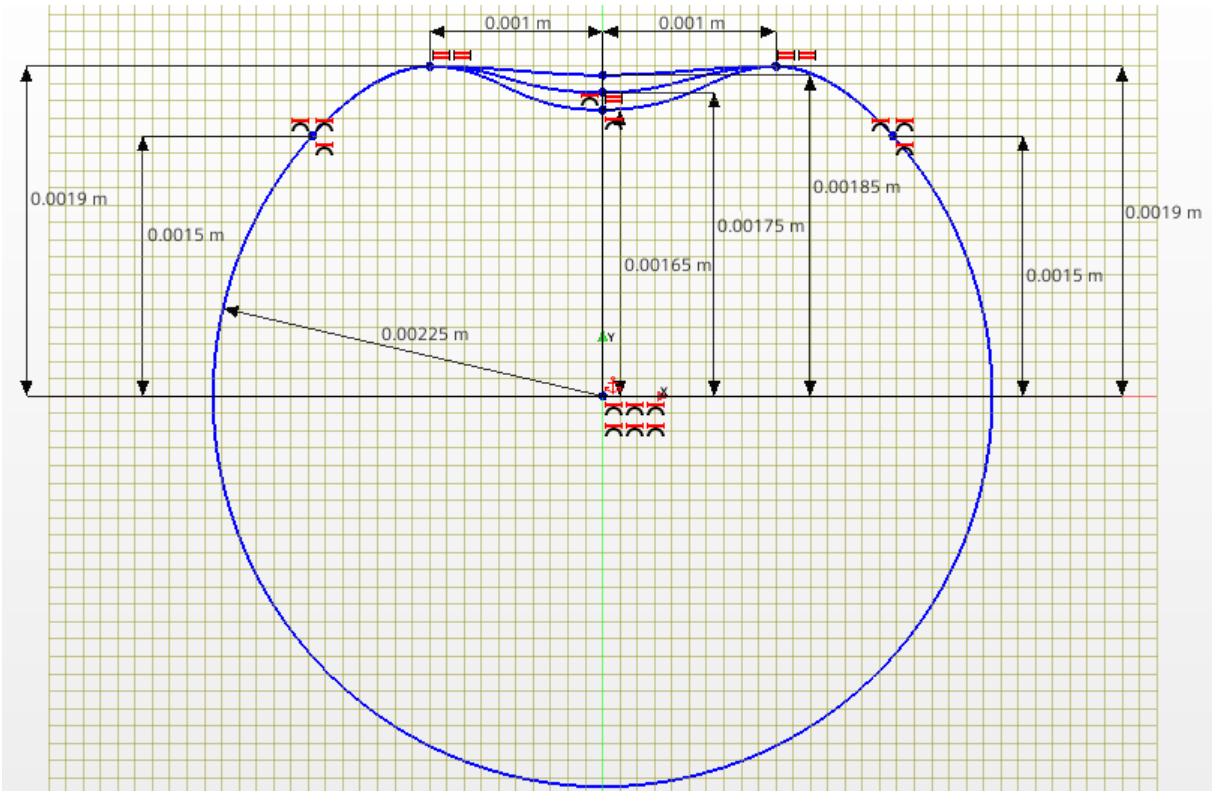

Figure 3.2: Corrugated tubes cross section and design of the corrugation height

Now considering the corrugation heights used in the tubes (0.4 mm, 0.5 mm and 0.6 mm) one can easily change their value by changing the middle point's height of the spline used to build the cross section. In Fig. 3.2 above it is possible to observe at the same time the three corrugation height configurations obtained by changing the middle point of the spline having all the other points a fixed constraint. Note that for modeling purposes the cross section is way more important than the mid section because the cross section and the guide line are the ones that in the end will define the corrugation. It is difficult to define a suitable spline for the corrugation once just by changing its top side points, despite having the same corrugation height, the corrugation will have a different form, which will affect the final results. So knowing this, the corrugations used in this study were created to be similar to the ones used

by Cruz [35] in order to compare results.

After completing the CAD models, table 3.1 was made to summarize the most important properties of the tubes that will be analyzed. Note that for numerical purposes only one smooth tube was created ($6\ mm$ long).

Table 3.1: Corrugated tubes and smooth tube properties

	$p \cdot 10^3(m)$	$e \cdot 10^3(m)$	$A_w/l \cdot 10^6(m)$	$V_w/l \cdot 10^9(m^2)$	$D_h \cdot 10^3(m)$	$P_w \cdot 10^3(m)$	$A_c \cdot 10^6(m)$	p/D_h	e/D_h	ϕ
tube 1	6	0.4	1.4518E-2	1.5259E-5	4.369	13.971	15.259	1.3734	0.0916	0.0059
tube 2	6	0.5	1.4771E-2	1.5150E-5	4.329	13.998	15.150	1.3859	0.1155	0.0093
tube 3	6	0.6	1.5053E-2	1.5043E-5	4.283	14.050	15.043	1.4010	0.1401	0.0133
tube 4	9	0.4	1.4232E-2	1.5259E-5	4.369	13.971	15.259	2.0601	0.0916	0.0040
tube 5	9	0.5	1.4374E-2	1.5150E-5	4.329	13.998	15.150	2.0789	0.1155	0.0062
tube 6	9	0.6	1.4547E-2	1.5043E-5	4.283	14.050	15.043	2.1015	0.1401	0.0089
tube 7	12	0.4	1.4122E-2	1.5259E-5	4.369	13.971	15.259	2.7468	0.0916	0.0030
tube 8	12	0.5	1.4218E-2	1.5150E-5	4.329	13.998	15.150	2.7719	0.1155	0.0046
tube 9	12	0.6	1.4344E-2	1.5043E-5	4.283	14.050	15.043	2.8020	0.1401	0.0067
smooth tube	-	-	1.4138E-2	1.5904E-5	4.5	14.137	15.904	-	-	-

As it is possible to see the first two columns show the pitches and corrugation heights used. Cruz [35] did numerical and experimental studies with helical inward corrugated tubes with the same pitch variation and from his work he concluded that the pitch had not major influence on the flow transition and that the corrugation height is way more important in this aspect. So that is one of the reasons why this parameter will also be studied in here, because it it important to verify how the transition varies.

In the third and fourth column of table 3.1 there is the wet area and the wet volume respectively per unit length. As already known, being the corrugation a passive enhanced heat transfer method, the wet areas of the corrugated tubes (for the same pitch) are always greater than the one of the smooth tube. However there is an exception for the tube 7 where the wet area is slightly lower than the smooth tube which happens due to low inward corrugation ($0.4\ mm$). This only means that the corrugation height should have a greater value yet, tube 7 will still be analyzed this way so it can be compared to the other tubes in order to verify if this case is really worth it in terms of heat transfer enhancement.

Now for the wet volume per unit length, it is clear that as the corrugation is placed inward there is less wet volume on the corrugated tubes compared to the smooth tube.

To be more clear another table, where it is possible to observe the corrugated tube to smooth tube volume ratio, was created (table 3.2). So being the smooth tube's wet volume the maximum volume that one tube can have, as higher the corrugation the less is the ratio for the corrugated tubes. This ratio values only depend on the corrugation height and for the corrugation heights of 0.4 mm, 0.5 mm and 0.6 mm the tubes have less 4.06%, 4.74% and 5.42% in wet volume respectively.

In the sixth and seventh columns of table 3.1 there are the wet perimeter and the cross section area respectively. Both of them only depend on the corrugation height as well and they are always lower than the the smooth tube's perimeter and cross section.

Finally, in the fifth and the three last columns there are the hydraulic diameter (determined with 2.33), the p/D_h and e/D_h adimensional ratios and the severity index (determined with 2.38) respectively, which can be replaced in the empirical correlations 2.37, 2.40, 2.41, 2.44 and 2.45 to obtain the different friction

Table 3.2: Corrugated tube to smooth tube wet volume ratio

	$p \cdot 10^3(m)$	$e \cdot 10^3(m)$	$V_{w,c}/V_{w,s}$
tube 1	6	0.4	0.9594
tube 2	6	0.5	0.9526
tube 3	6	0.6	0.9458
tube 4	9	0.4	0.9594
tube 5	9	0.5	0.9526
tube 6	9	0.6	0.9458
tube 7	12	0.4	0.9594
tube 8	12	0.5	0.9526
tube 9	12	0.6	0.9458
smooth tube	-	-	1

factors and Nusselt numbers for different flow regimes in order to validate the numerical results.

Note that A_w, V_w, P_w and A_c values were are obtained from the CAD models designed on the StarCCM+ software [34].

3.2 Numerical Model

As already mentioned, the software STAR-CCM+ will be the one used to do the numerical simulations [34]. One of the main reasons that it was chosen it's because it is a software capable of solving fluid flow and heat transfer problems at the same time. It is also very versatile since its solution includes the geometry, the mesh, the boundary conditions, the physics models and the simulation results all in one environment.

3.2.1 Boundary conditions

So at first place, the CAD geometries that were made were split by patch in order to identify the inlet, the outlet and the wall surface of the domain. With these it was possible to define the boundary conditions. This being said, the inlet surface was defined as an inlet velocity boundary condition, the outlet surface was defined with a pressure outlet boundary condition and finally the wet surface (wall surface) was left with the default wall boundary condition (with no-slip condition) which are the conditions normally used for an incompressible fluid flow. Usually the helical corrugated tubes are long so only a periodic section was considered for the research. Therefore the inlet and the outlet boundary conditions were defined as an interface which means that the solution quantities transfer between the two regions of the simulation. The periodic length of the tubes corresponds to the pitch used in each one, as it is possible to see in table 3.1.

Note that in order to determine the Nusselt number a constant heat flux must be imposed on the wall. This is not necessary for the friction factor once it will be determined for isothermal conditions.

3.2.2 Mesh models

The second task is to define the mesh. The polyhedral mesher, the prism layer mesher and the surface remesher were the models used. Since the corrugated tubes have part of the shape of a smooth tube the generalized cylinder meshing model was also supposed to be chosen. However, since the corrugation heights used in the tubes are too prominent this model did not work as expected and was rejected, especially because every mesh created with this model was an irregular mesh.

So for the polyhedral meshing model it is known that it uses an arbitrary polyhedral cell shape to build the core of the mesh Fig. 3.3.

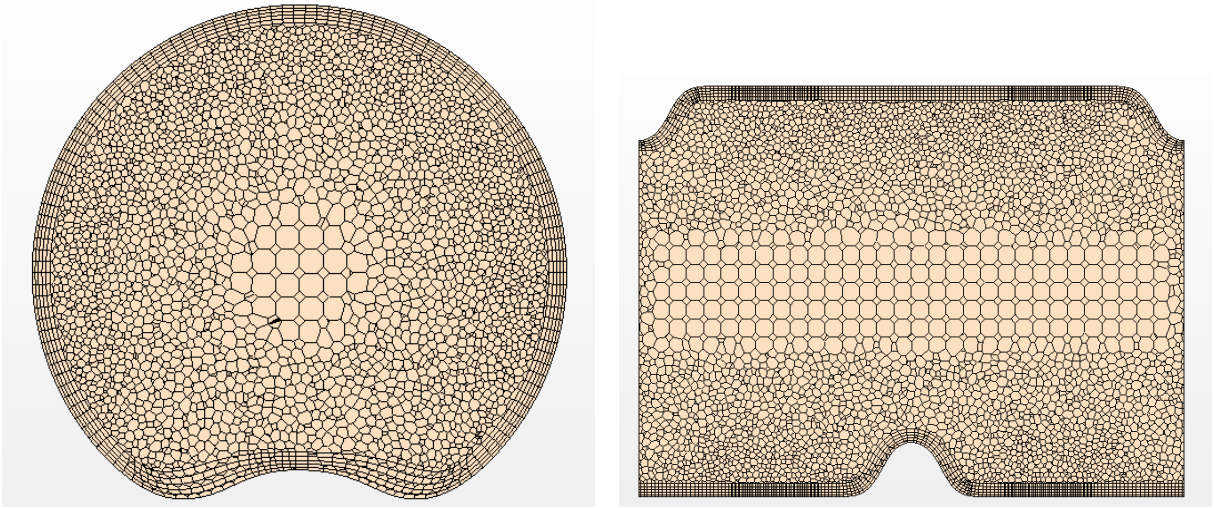

(a) Cross section mesh view

(b) Mid section mesh view

Figure 3.3: Representation of a coarse polyhedral and prism layer mesh with surface remesher in the helical corrugated tube with $p = 6$ mm and $e = 0,6$ mm

It could be used with the generalized cylinder mesher to generate extruded orthogonal cells along the length of the cylindrical section of the tube, however as explained, it was not possible but it is recommended with cylindrical geometries. As it is possible to see in the figure, a volumetric control was also created to reduce the number of cells in middle once the most important region for analysis is the region near to the wall.

As the polyhedral mesher is used with a periodic interface, the mesher produce a conformal mesh for the periodic boundary pair.

The prism layer mesher is used to generate orthogonal prismatic cells next to the boundaries or wall surfaces creating a layer of cells essential to improve the accuracy of the flow solution. It is defined in terms of its thickness and the number of cell layers within it as it may be seen in Fig. 3.3.

Finally, there is the surface remesher which in order to improve the overall quality of the existing surface and optimize it for the volume mesh models, it retriangulates the surface of the geometry. After this, the resulting mesh can be seen in Fig. 3.4.

Note that in the interface the prism layer mesh has an irregular representation however in the interior of the tube it was generated as expected. This irregularities does not compromise the final results. One should also know that a coarse mesh was represented since the different types of mesh are more clearly

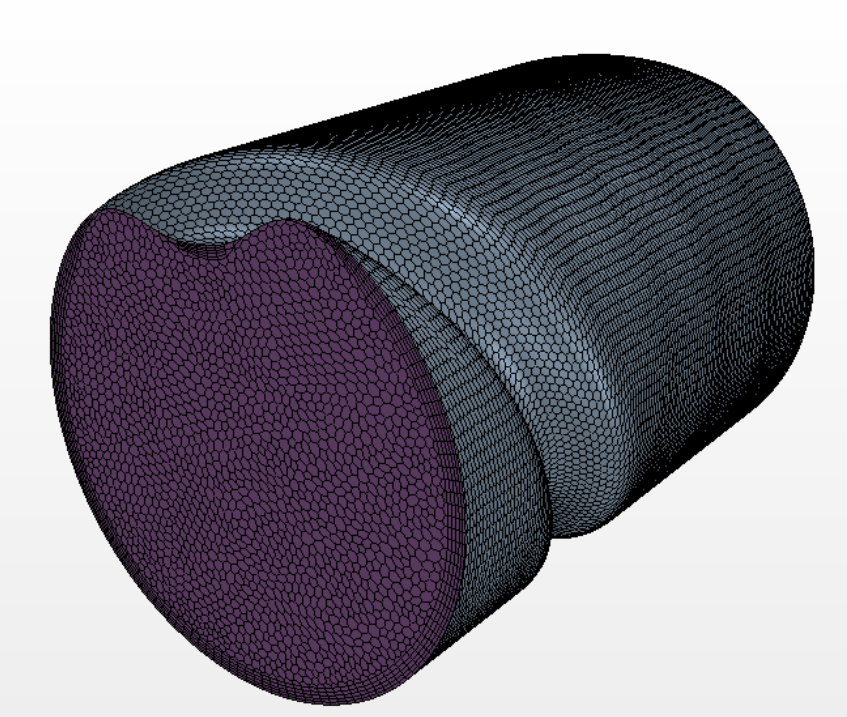

Figure 3.4: Isometric mesh view of the helical corrugated tube with $p = 6$ mm and $e = 0.6$ mm

identified. Also note that the number of cells used will be described at section 3.3 on Table 3.3.

3.2.3 Physics models

Assumptions

After defining the mesh, the physics models must be chosen to initiate the numerical simulations. However, as the real case studies sometimes are too complex to define, some assumptions are made in order to simplify the numerical studies. Therefore, the following assumptions are presented for this study:

- Water as working fluid;
- Constant water properties evaluated at $300K$;
- Mean bulk inflow temperature of $300K$;
- Incompressible flow;
- Newtonian fluid (constant viscosity);
- Hydrodynamically and thermically fully developed flow;
- Constant wall heat flux of $100\ kW/m^2$;
- Negligible water vaporization;
- Negligible gravitacional forces ;

- Negligible heat transferred by conduction and radiation.

A lot of studies focus on the liquid heat transfer process because of the higher heat transfer coefficients of denser fluids [17, 50]. Being the water a safer fluid, with an easy access and management, it is the most common choice for experiments. Water was chosen as a working fluid not only for these reasons but also because it was the same fluid used by Cruz [35], among other assumptions here enumerated. This was done in order to better compare the final results. Being that said, it is also assumed the water to have constant properties evaluated at $300K$ with the same mean bulk inflow temperature. As said by Cruz [35], these are valid assumptions for numerical analysis if the temperature differences are low ($\delta T < 10K$), which is verified in his and this work.

As already told in the governing equations section, it was also considered a Newtonian fluid in which is known that viscous stresses are proportional to the rates of deformation and therefore the viscosity is considered constant [52]. The flow was also considered to be hydrodinamically and thermally developed so it could be modeled as a periodic region with periodic boundary conditions . It was considered a constant heat flux boundary condition with $q'' = 100kW/m^2$ in order to have some reasonable water temperature variation from the inlet to the outlet of the tube. At the same time water vaporization is neglected so the fluid flow can always be in liquid state (one phase).

As the wall thickness of the tube is really low, as it is described in the 3D CAD geometry, and as said by Bergman et al. [33] the net heat transfer by conduction in the axial direction can be neglected as it has a small contribution compared to the heat transferred by forced convection. The same applies to the heat transferred by radiation (neglected) once an estimation made by Cruz [35] shows that its contribution is two orders of magnitude lower compared to the two previous. As for the gravitational forces, they can also be neglected once Andrade [54] work shows that the heat transferred by forced convection is predominant.

Laminar regime

With these assumptions the numerical physics models can now be chosen. So for the laminar regime the following models were used:

- Three dimensional
- Liquid;
- Segregated flow;
- Constant density;
- Gradients;
- Laminar;
- Steady/Implicit unsteady;
- Segregated fluid temperature or isothermal;

- Solution interpolation;

When choosing the models, first, the continuum space must be defined. So the three dimensional model was chosen since corrugated tubes does not have any symmetry plans in order to make 1D or 2D analysis and mainly because the three cylindrical components (r, θ, z) are important for the secondary flow analysis. Then, since water is the working fluid, a liquid material was chosen. Its properties were changed for the ones given by Bergman et al. [33] evaluated at $300K$. With it, one should then define the pretended type of flow, being in this case the segregated flow the one used. This model solves each of the momentum equations (2.53, 2.54 and 2.55) in turn, one for each dimension. The connection between the momentum and continuity (2.49) equations is achieved with a predictor-corrector approach [34]. The segregated fluid flow is based on constant density fluid flow which was one of the assumptions made and the model chosen for the equation of state (constant density). That is the main reason why the segregated flow model was selected. With this one the gradient model is automatically selected as well.

The viscous regime model for this case is laminar and the time model selection (steady or implicit unsteady) depends on the convergence state and the Reynolds number used for the analysis.

Additional physics models as segregated fluid temperature or isothermal and the solution interpolation were also used. The segregated fluid temperature model will solve the total energy equation (2.57) with temperature as the solved variable [34]. It allows to define the bulk inflow temperature which was set to $300K$. This option was always selected every time a Nusselt number needed to be found. In order to determine the pressure drop along the tube and finally the friction factor associated, isothermal analysis were made. For this case the segregated fluid isothermal model was always selected. This model keeps the continuum temperature constant with $300K$ (set value). This option is suitable for problems where the temperature variations are small and negligible. It would be computationally expensive to solve an ordinary energy transport equation when it would only yield a nearly constant field of temperature [34].

In the other hand the solution interpolation model allow to select the interpolation method that is used to map the solution data when remeshing occurs. The nearest neighbor was the one used by default. It maps the solution data from one mesh to another by comparing the cell centroids in each mesh. It means that the new cell gets the solution data from an old cell whose cell centroid is closest to its own. Note that despite being quick it does not provide the smoothest interpolation results [34].

Turbulent regime

For the turbulent regime the following models were used:

- Three dimensional;
- Liquid;
- Segregated flow;
- Gradients;

- Constant density;
- Implicit unsteady;
- Turbulent;
- Reynolds-Averaged Navier-Stokes;
- All y^+ wall treatment;
- $k-\omega$ turbulence;
- SST (Menter) $k-\omega$;
- Wall distance;
- Segregated fluid temperature or isothermal;
- Solution interpolation;

So the first steps for the turbulent regime are the same as for the laminar regime. First the space is defined as three dimensional, then a liquid material is chosen and the flow is defined as segregated flow (with the gradients model auto selected). After that the constant density model is chosen for the equation of state and the time selection was implicit unsteady once for steady state the simulations do not converge.

As the turbulent regime will be studied in this case, the viscous regime is set to turbulent and by choosing this model the Reynolds-Averaged Navier-Stokes (RANS) model is automatically associated. This last one provides closure relations for the RANS equations that govern the transport of the mean flow quantities [34]. These equations can be obtained by decomposing each solution variable φ in the instantaneous Navier-Stokes equations into their mean value $\overline{\varphi}$ and their fluctuating component φ' resulting in

$$\varphi = \overline{\varphi} + \varphi' \tag{3.1}$$

where the velocity components, pressure, energy or species concentration are represented by φ.

Whit this, for the Reynolds averaged turbulence, the $k-w$ turbulence model was chosen. This is a two-equation model that solves transport equations for the turbulent kinetic energy k and the specific dissipation rate ω (the dissipation rate per unit turbulent kinetic energy $\omega \propto \epsilon/k$) in order to determine the turbulent eddy viscosity [34].

A study developed by Wilcox et al. [55] state that the $k-\omega$ model has a better performance (compared with the $k-\epsilon$ model) for boundary layers under adverse pressure gradients. However the most significant advantage is that it may be applied for all the boundary layer including the viscous-dominated region, without further modification. Nevertheless, one should note that the $k-\omega$ model has one big disadvantage. In its original form, the boundary layer computations are sensitive to the values of ω in the free-stream which translates into extreme sensitivity to inlet boundary conditions for internal flows (a problem that the $k-\epsilon$ model does not have).

This sensitivity problem was solved by Menter [56] who recognized that the transport equation from the standard $k-\epsilon$ model could be transformed into a ω transport equation by variable substitution [34]. The transformed equation is similar to the one in the standard $k-\omega$ model but has an additional non-conservative cross-diffusion term containing the dot product $\nabla k \cdot \nabla \omega$. This inclusion potentially makes the $k-\omega$ model give identical results to the k_ϵ model. Menter [56] suggested using a blending function (which includes functions of wall distance) that would include the cross-diffusion term far from walls, but not near the wall. By this approach the $k-\epsilon$ model is effectively blended in the far-field with the $k-\omega$ model near the wall making the flow simulations practical. Menter also made a modification to the linear constitutive equation and named the model containing this modification as SST (shear-stress transport) $k-\omega$ model. This model was also automatically chosen by STAR-CCM+ [34].

At the same time it was also automatically chosen the all y^+ wall treatment. It is known that the walls are a source of vorticity therefore it is essential an accurate prediction of the flow across the wall boundary layer. For high Reynolds numbers the streamwise velocity is characterized by unsteady swirling flows inside the boundary layer [34]. For RANS turbulence models the wall treatment provides boundary conditions to the solvers for flow and energy that are specific to turbulent boundary layers. In addition, it imposes special values for turbulence quantities on the centroids of the near-wall cells. Note that not all wall treatments are available with every RANS model or model variant. For example, high Reynolds number models do not contain the ability to attenuate the turbulence in the viscosity-affected regions and therefore they only include a high-y^+ wall treatment ($y^+ > 30$). The low Reynolds number models only work with a low-y^+ wall treatment ($y^+ \sim 1$) and an all-y^+ wall treatment (used in this case). Finally, the two-layer all-y^+ wall treatment is only available with the two-layer $k-\epsilon$ and the two-layer Reynolds Stress turbulence models [34]. The all-y^+ wall treatment uses blended wall functions that recreat the low-y^+ wall treatment for fine meshes and the high-y^+ wall treatment for coarse meshes. It also produces reasonable answers for meshes of intermediate resolution (when the wall-cell centroid falls within the buffer region of the boundary layer). Thus, this wall treatment is suitable for a wide range of near-wall mesh densities.

Another automatic selected model was the wall distance which is a parameter that represents the distance from a cell centroid to the nearest wall face with a non-slip boundary condition. Note that many physical models require this parameter to account for near-wall effects. In order do determine the wall distance the implicit tree method was used by default. This method makes an exact projection calculation in real space, which is based on a triangulation of the surface mesh.

One should note that all the models used for the turbulent regime were used with the default parameter values.

Transition regime

The transition region is also relevant for this work and some tests were performed with the $\gamma Re-\theta$ (Gama-Re-Theta) transition model. As said by [34] this is a two-equation correlation-based transition model that is capable to provide a semi-local approach to predict the onset of transition in a turbulent boundary layer. It is known that the majority of the transition models are based on the concept of

intermittency which is a measure of the amount of time during which the flow is turbulent. Thus, an intermittency value of 1 represents a fully turbulent flow (100% of the time) and an intermittency of 0 corresponds to a fully laminar flow. It is also said that this model was specially formulated for unstructured CFD codes. As previously mentioned the Gamma-Re-Theta model is based on 2 equations where the first one is an intermittency transport equation. This one is used in such a way that the source terms attempt to mimic the behavior of the algebraic engineering correlations. It is also important to note that the evaluation of momentum thickness Reynolds number is avoided by relating this quantity to a vorticity-based Reynolds number. Finally, for the second equation, a correlation for transition onset momentum thickness Reynolds number is defined in the free-stream which is transported (by solving a separate transport equation) into the boundary layer.

This transition model is incomplete since two critical correlations were proprietary and therefore omitted. A reason for such an omission is that the model provides a framework for users to implement their own correlations, which for the case of STAR-CCM+ is done in such a way that allows the custom specification of correlations using field functions (wall distance in this case). One must recognize that the process of calibrating the needed correlations is very complex and time-consuming and therefore the generic correlations provided within the model were used by default.

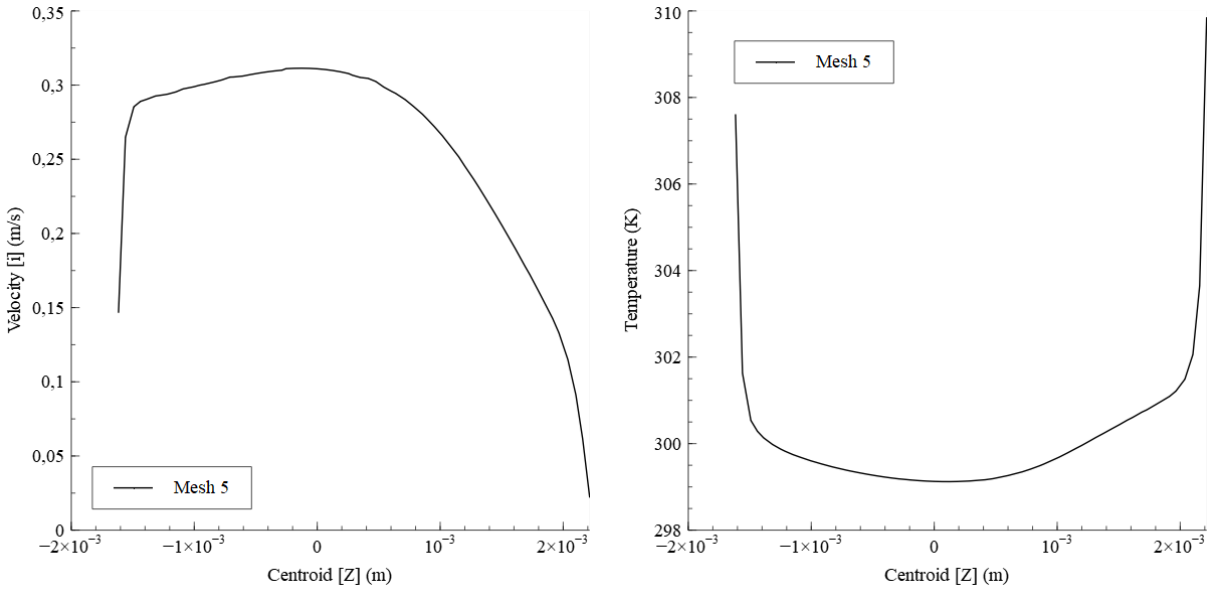

(a) Velocity profile (mesh 5 from Table 3.3)

(b) Temperature profile (mesh 5 from Table 3.3)

Figure 3.5: Velocity and temperature profiles for $Re = 1000$, $p = 6\ mm$ and $e = 0.6\ mm$ with an imposed constant heat flux on the walls of $\dot{q} = 100\ kW/m^2$ and transition model $\gamma Re - \theta$

As initially mentioned, tests were performed with this model and its default values, however the results obtained were erroneous as it is possible to see in Fig. 3.5. The most refined mesh (mesh 5 from section 3.3 and Table 3.3) was here used once they are the most accurate results as per grid convergence study (Fig. 3.7 and 3.8) that will be analyzed at section 3.3.To better understand the plots one should know that a line probe that pass through the centroid of the corrugated tube (in the z coordinate direction) was defined in order to obtain the axial (i) velocity and temperature profiles of that region. In one hand the velocity and temperature profiles for the tested corrugated tube (with the most refined mesh) were not

characteristic, namely similar to the fully developed smooth tube profiles (Fig. 2.1 and 2.4). There are also strong gradients near the corrugation lower point ($\approx -1.6 \cdot 10^{-3}\ m$) and the secondary flow region near the tube wall ($\approx 1.8 \cdot 10^{-3}\ m$) is indistinguishable. At Fig. 3.6 bellow it is possible to observe, through the velocity field in the mid section, that the flow does not seem fully developed, despite having a converged solution.

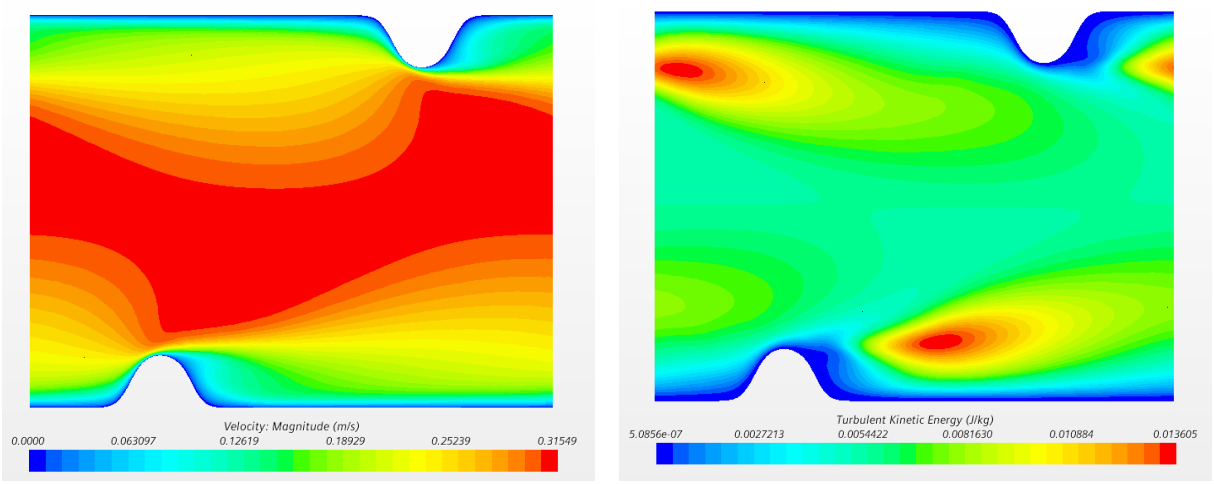

(a) Velocity Magnitude

(b) Turbulent Kinetic Energy

Figure 3.6: Velocity magnitude in the mid section and TKE for $Re = 1000$, $p = 6\ mm$ and $e = 0.6\ mm$ with an imposed constant heat flux on the walls of $\dot{q} = 100\ kW/m^2$ and transition model $\gamma Re - \theta$

The fluctuations of the flow motion were also analysed using turbulence kinetic energy (TKE), which is dependent on the velocity and can be defined as the measure of the turbulence intensity present in the flow. As one can see in the TKE field of Fig. 3.6, the peak is too close to the downstream of the corrugation. As demonstrated in Wang et al. [30], Córcoles-Tendero et al. [57], Córcoles et al. [58] work, this would only be acceptable for high turbulent Reynolds numbers ($Re > 10000$) and for a bigger pitch ($p > 10\ mm$). One should note that it is considered a constant corrugation height of $e = 0.6\ mm$, being equal to the corrugation height presented at [58] and similar to the other two papers ([30, 57]). As this case study has $Re = 1000$ and a pitch of $p = 6\ mm$, this is not possible to happen and the TKE peak should be further away (near to the upstream of the next corrugation as it will be shown in the Results chapter).

So with these problems plus the fact that the used transition model is incomplete, prevented the same from being used. Thus it was considered that the transition occurs instantaneously, being only chosen for the different Reynolds numbers a laminar or a turbulent model. It is worth noting that the critical transition Reynolds number for the different corrugated tubes was determined through equation 2.39 in order to choose the flow regime.

3.3 Verification and Validation

As said by Versteeg and Malalasekera [52] one should recognize that errors and uncertainty are inevitable aspects of CFD modelling so it becomes essential to develop rigorous methods to quantify the

level of confidence in its results. Whit this, two main concepts appear. In one hand there is the numerical verification which can be defined as the process of determining whether the model implementation accurately represents the developer's conceptual description of the model and the solution to the model. On the other hand there is the numerical validation that can be defined as the process of determining the degree to which a model is an accurate representation of the real world from the perspective of the intended uses of the model. With validation it is possible to quantify the uncertainty. These two concepts, that had their origin from AIAA (American Institute of Aeronautics and Astronautics), Oberkampf and Trucano, are nowadays broadly accepted.

Verification

For the numerical verification a grid independence study was made. The analysis were performed for the worst case scenario, which means, for the tube of lowest pitch and highest corrugation ($p = 6\ mm$ and $e = 0.6\ mm$). The test was made for two Reynolds numbers ($Re = 100$ in laminar regime and $Re = 1000$ in turbulent regime) and for five different meshes.

Table 3.3: Number of cells per mesh

	Base Size (m)	Number of prism layers	Cells
Mesh 1	$2 \cdot 10^{-4}$	4	51782
Mesh 2	$1 \cdot 10^{-4}$	5	334606
Mesh 3	$8 \cdot 10^{-5}$	6	627609
Mesh 4	$6 \cdot 10^{-5}$	7	1465398
Mesh 5	$4 \cdot 10^{-5}$	8	2933918

As it is possible to see in table 3.3 the main parameters that were changed during the refinement of the mesh (Fig. 3.3 and 3.4) were the base size and the number of prism layers. The center cells were also changed based on the percentage of the base size mesh and the prism layer thickness was defined with $1.5 \cdot 10^{-4}\ m$ and kept constant throughout the refinement process.

Table 3.4: Water properties at 300K [33]

$T(K)$	$v_f \cdot 10^3(m^3/kg)$	$\rho(m^3/kg)$	$c_{p,f}(kJ/(kg \cdot K))$	$\mu_f \cdot 10^6(N \cdot s/m^2)$	$k_f \cdot 10^3(W/(m \cdot K))$	Pr_f	$\nu_f \cdot 10^9(m^2/s)$
300	1.003	997	4.179	855	613	5.83	857.565

At table 3.4 above, there are shown the water parameters that were defined for the grid independence analysis and for all the simulations done in this work.

As already mentioned in the Numerical model chapter (discussion about the transition region) a line probe that passes through the centroid of the tube (in the z coordinate direction) was defined in order to obtain the axial (i) velocity profile of that region. Therefore, for the laminar regime ($Re = 100$) and for the turbulent regime ($Re = 1000$) an isothermal velocity profile was obtained (Fig. 3.7). One should note that each solution was only accepted when the residuals of the simulations were at least in the order of 10^{-5} [52]. It was also certified that the the near-wall grid had $y^+ < 1$, because of the no-slip condition used at the walls.

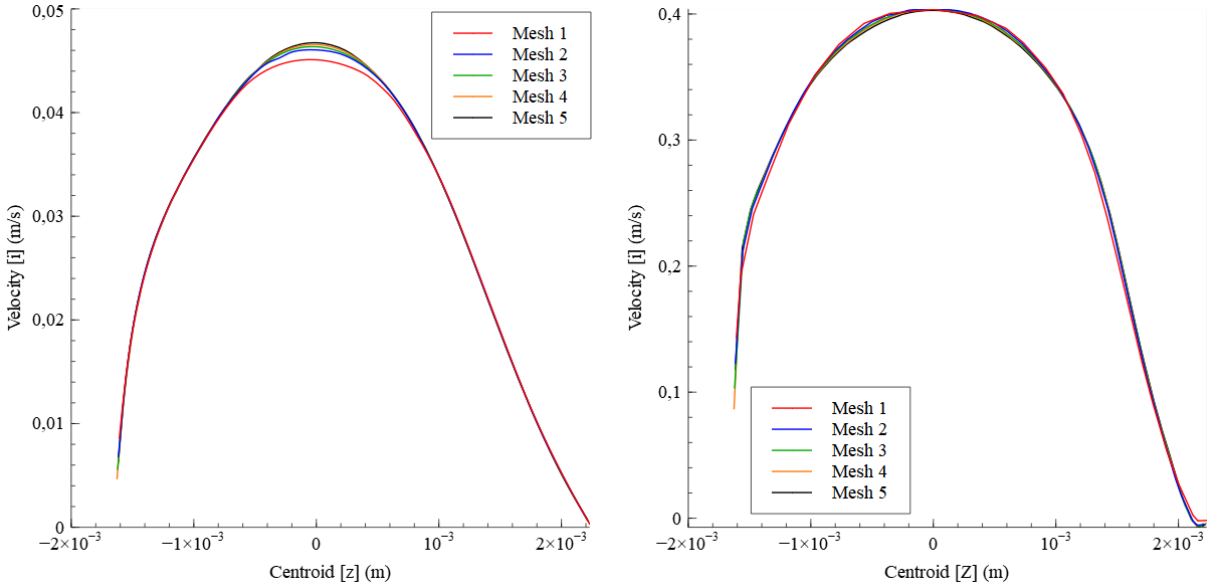

(a) $Re = 100$ (b) $Re = 1000$

Figure 3.7: Isothermal grid independence study for the corrugated tube with $p = 6\ mm$ and $e = 0.6\ mm$

Through analysis it was concluded that the mean relative error of the velocity between the line probe points at mesh 4 and 5 was 1.21% and 1.13%, for $Re = 100$ and $Re = 1000$ respectively. For $Re = 100$ one can also notice a slight velocity augmentation near to the lowest corrugation point ($\approx -1.6 \cdot 10^{-3}\ m$) compared to the nearest point to the tube wall ($\approx 1.6 \cdot 10^{-3}\ m$). It is clear that viscous effects are predominant in the laminar regime (lower maximum velocity and lower velocities near to the wall) and therefore the velocity profile becomes more tapered. In the other hand, for $Re = 1000$ turbulent diffusion becomes predominant and there is higher velocity near to the wall and corrugation, being the maximum velocity in this regime ≈ 8.62 higher than for the laminar case.

As already known, the analysis that are going to be performed for the different corrugated tubes will have an imposed constant heat flux on the walls of $\dot{q} = 100\ kW/m^2$. As for isothermal conditions there is only an hydrodynamic boundary layer and for an imposed heat flux a thermal boundary layer is also formed, it is important to verify if there is any influence of this last one on the velocity profile. Thus, another study was made (Fig. 3.8) for $Re = 1000$ in order to obtain the temperature profile of the corrugated tube and the velocity profile (to be compared with the isothermal one). So it was obtained a mean relative error of the velocity and temperature (between mesh 4 and 5) equal to 1.12% and 0.09% respectively. In the temperature profile plot it is easy to spot the secondary flow region originated by the presence of the corrugation ($\approx 1.7 \cdot 10^{-3}$ to $2 \cdot 10^{-3}\ m$). This phenomenon will be better described in the Results chapter.

Finally, as the maximum absolute error between the thermal and isothermal velocity for mesh 4 and 5 was $1.4 \cdot 10^{-4}$ and $2.06 \cdot 10^{-4}$ respectively, it was concluded that the imposed heat flux had no influence on the velocity profile of the tubes. As the relative error between mesh 4 and 5 was around 1%, mesh 4 parameters were the ones selected to be used in all the numerical simulations for the 9 different corrugated tubes in order to have not only accurate results but also reduce the numerical analysis time.

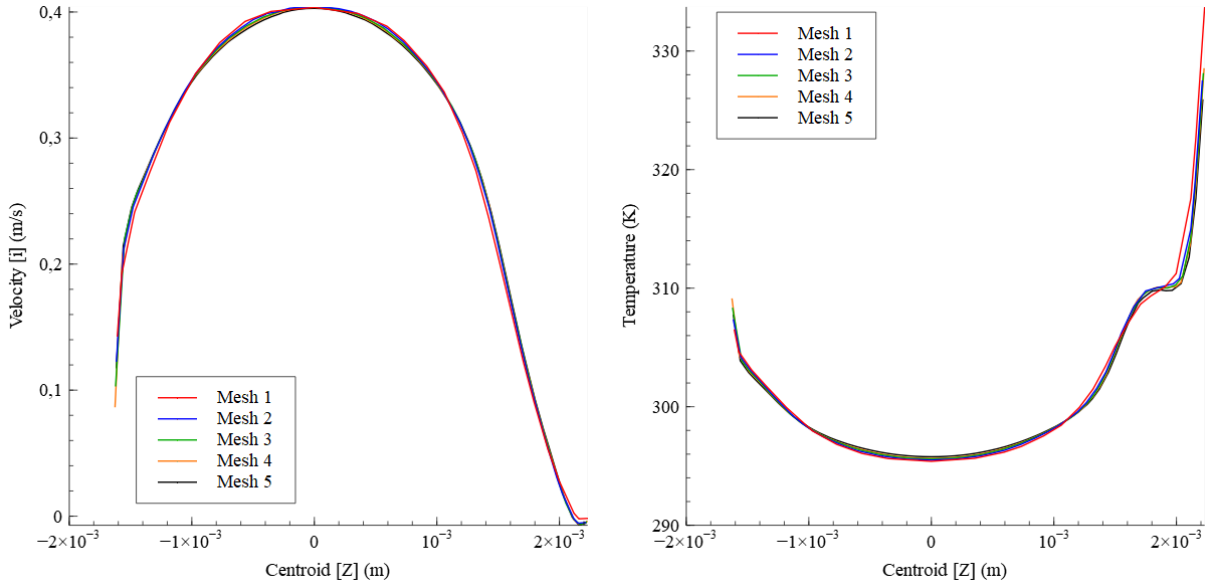

(a) Velocity profile

(b) Temperature profile

Figure 3.8: Grid independence study for $Re = 1000$, $p = 6\ mm$ and $e = 0.6\ mm$ with an imposed constant heat flux on the walls of $\dot{q} = 100\ kW/m^2$

One should note that the thermal analysis was only performed for the turbulent Reynolds once it was proven that the imposed heat flux had no influence on the turbulent velocity profile ($Re = 1000$). Hence, it won't also have influence in the laminar regime ($Re = 100$).

Validation

In order to validate the physical models a basic smooth tube problem will be evaluated and compared with the available correlations.

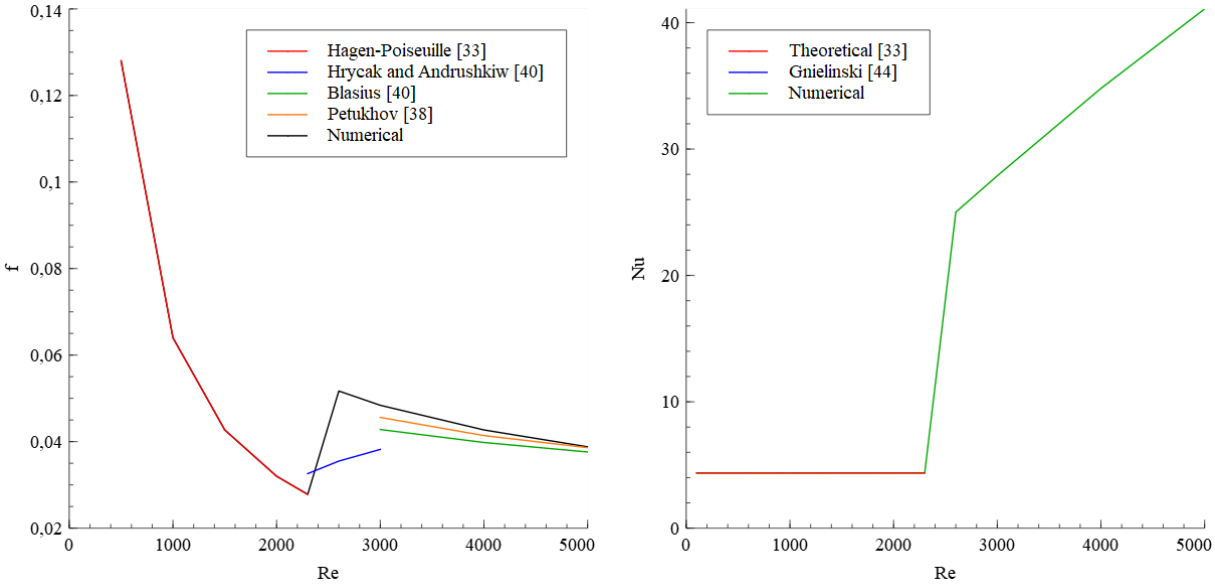

(a) Isothermal friction factor

(b) Nusselt number

Figure 3.9: Isothermal friction factor and Nusselt number for a smooth tube

So after the analysis two plots were obtained as it is possible to observe on the Fig. 3.9 bellow. The left plot refers to an isothermal friction factor analysis on the tube. In this case the numerical results were compared to the Hagen-Poiseuille equation, 2.10 (for hydrodynamically fully developed laminar regime), to the Hrycak and Andrushkiw equation, 2.12 (for the transition regime) and finally to the Blasius and Petukhov equations, 2.13 and 2.11 respectively (for hydrodynamically fully developed turbulent regime). The numerical results were obtained through the Darcy-Weisbach equation, 2.9 where the pressure drop was determined through the inlet to the outlet water interface (pressure drop report).

By plot analysis, for the laminar regime, the maximum relative error between the numerical friction factor and the one obtained through the Hagen-Poiseuille equation was 0.03%, which is a good fitting.

As already mentioned, it was considered an instantaneous transition. So the laminar model was used until $Re = 2300$ (onset of the transition regime as referred by Cruz [35] and Bergman et al. [33]) and the turbulent model was defined from $Re = 2600$.

With an instantaneous transition, comparing the Hrycak and Andrushkiw isothermal transition equation to the numerical results is is obvious that it will exist a huge error associated. So the maximum relative error for the friction factor between the numerical results and the one obtained through equation 2.12 is 31.4% at $Re = 2600$, decreasing the error as Re increases.

For the turbulent regime the maximum relative error between the numerical friction factor and the Blasius and Petukhov equations, are 11.61% and 5.81% respectively, for $Re = 3000$. Both errors also decrease with increasing Re.

These high relative errors in transition and onset of the turbulent regime can be explained through Andrade et al. [59]. In this paper it is mentioned that Everts and Meyer [60, 61] stated that the transition flow regime can be divided into two flow regimes which are the transitional and the quasi-turbulent regimes. Identifying the onset of transitional regime is easier than the end of it. Therefore the start of the quasi-turbulent flow regime becomes not clear, which can bring implications on accurately identifying the start of the turbulent flow regime. Nevertheless, through their work it was possible to define the transition zone for the smooth tube, which starts from $Re \approx 2300$ (as previously mentioned) and ends at $Re \approx 3000$.

In conclusion, it is acceptable to have higher relative errors for the quasi-turbulent regime. From $Re \approx 3000$, where the turbulent regime begins, the errors start to decrease reaching 31% (Blasius) and 0.54% (Petukhov) at $Re = 5000$, compared to the numerical results. So the obtained results become valid. Note that in the Results chapter 4 it will be considered a transition region for the smooth tube of $Re = 2300 - 3000$ in order to be in agreement with Andrade et al. [59].

Now, for the heat transfer on the smooth tube, the average numerical Nusselt number on the wet surface of the tube will be compared to the theoretical Nusselt number of the laminar regime, 2.29, and to the Gnielinski correlation for a hydrodynamiaclly and thermally fully developed turbulent regime, 2.30.

In order to determine the numerical average Nusselt number different parameters were previously obtained through numerical analysis. Therefore it was made a surface average report on the wet surface to determine the wall temperature (T_w), a mass flow average report on the inlet interface surface to determine the mean inflow temperature ($T_{m,i}$) and a mass flow average report on the outlet interface

surface to determine the mean outflow temperature ($T_{m,o}$). Then equation 2.21 was used to obtain the convective heat transfer coefficient (h). Note that the mean temperature (T_m) was determined through the average $(T_{m,i} + T_{m,o})/2$. This is acceptable since there is a small size domain (small corrugated tubes) where the inflow and the outflow temperatures are very close (more a linear temperature growth which in comparison to a long tube will have a logarithmic growth). One should also note that $T_s = T_w$. Finally, with h, using equation 2.21, where $D = D_i$ (inner tube diameter) and k from table 3.4, the numerical Nusselt number was calculated. It is important to know that this procedure was used for all the tested tubes.

Thus analysing the right plot of Fig. 3.9 the maximum relative error between the laminar numerical Nu and the theoretical one is 0.35% which is a good fitting. In the other hand, the maximum relative error between the turbulent Nu and the Gnielinski correlation is 24.31% for $Re = 3000$, decreasing to 7.93% for $Re = 5000$. As specified by Ammar and Park [46] the Gnielinski correlation has an error of $\pm 20\%$. Being this said, despite the error spike at $Re = 3000$, as the Reynolds increases, being further away from the quasi-turbulent regime, the error start to decrease and therefore the turbulent results also become acceptable. It is worth noting that transition Nusselt was not analysed due to the lack of correlations.

With this analysis one can conclude that the smooth tube case is fully validated, missing only the corrugated tubes validation. These will be validated at the Results chapter 4, when possible, with the available correlations.

Chapter 4

Results

This chapter will start with the corrugated tubes validation with the available empirical correlations. Then the objectives from section 1.3 will be analyzed and discussed. Finally, the optimum working conditions will be described for the tubes with $6\ mm$ pitch and 0.4, 0.5 and $0.6\ mm$ corrugation height, for the tubes with $9\ mm$ pitch and 0.4, 0.5 and $0.6\ mm$ corrugation height and at last for the tubes with $12\ mm$ pitch and 0.4, 0.5 and $0.6\ mm$ corrugation height. Note that all the studies were performed for $Re = 100-3000$. Also note that a different nomenclature from Table 3.1 and 3.2 in the following chapters is used in order to be more clear which tubes are being analyzed in graphs and in order to better display of the data in the result tables.

4.1 Corrugated tubes validation

As per Implementation's section 3 last statement, in this section the corrugated tubes validation will be analyzed.

One should note that from now on in all the represented plots the black line will always represent the smooth tube's numerical results, the lines with circles the numerical results for the tubes with $6\ mm$ pitch, the lines with triangles the numerical results for the tubes with $9\ mm$ pitch and the lines with squares the numerical results for the tubes with $12\ mm$ pitch. One should also note that for each of these groups of lines the darker the colour the higher the corrugation (0.4, 0.5 and $0.6\ mm$). In the work of Cruz [35], in order to distinguish the different tubes, the severity index (equation 2.38) was used instead. This approach was not chosen due to very similar severity index values which could induce some confusion.

As stated at transition regime subsection of Implementation section 3 it was considered an instantaneous transition region for all the tubes were the critical Reynolds number for the onset of the transition region was determined through correlation 2.39 given by Vicente et al. [50]. This correlation confirms that the main parameter responsible for the advance or delay of the onset of the transition region in the corrugated tubes is the corrugation height. The determined critical Re for the 3 different corrugation heights (0.6, 0.5 and $0.4\ mm$) with 15% accuracy are ≈ 753, ≈ 807 and ≈ 879 respectively (lower margin). It is very clear that the higher the corrugation the lower the critical Reynolds. However, as the values

are very similar and in order to ease the analysis the transition region was then defined for the range of Reynolds $Re = 700 - 850$. This range is acceptable once Cruz [35], through empirical analysis for the tubes with $0.4\ mm$ corrugation height, determined that the transition range was given by $Re = 850 - 1000$ mentioning that it could even be extended to $Re = 700 - 1100$ to better fit some numerical results.

So for these conditions the following results are presented.

4.1.1 Friction factor

Analyzing the isothermal friction factor, between all the nine corrugated tubes, one can start by inspecting the three tubes with $0.4\ mm$ corrugation height and 12, 9 and $6\ mm$ pitch (Fig. 4.1, 4.2 and 4.3 below). The reason is that these were the same parameter tubes studied by Cruz [35] and therefore there are more experimental results to support the numerical data and validate it.

As previously explained for the smooth tube validation, the numerical results were obtained through the Darcy-Weisbach equation 2.35 where the pressure drop was determined through the inlet to the outlet water interface of the corrugated tube (pressure drop report).

So with this, for the laminar region ($Re = 100 - 700$ in red) the numerical data was compared to the laminar friction factor correlation 2.37 obtained by Vicente et al. [50].

In this range, comparing Vicente's laminar correlation to the laminar numerical results for the tube with $12\ mm$ pitch and $0.4\ mm$ corrugation height (Fig. 4.1) it is possible to observe that the maximum relative error of the numerical data compared to the empirical one is 8.2% at $Re = 100$ decreasing until 5.5% at $Re = 700$.

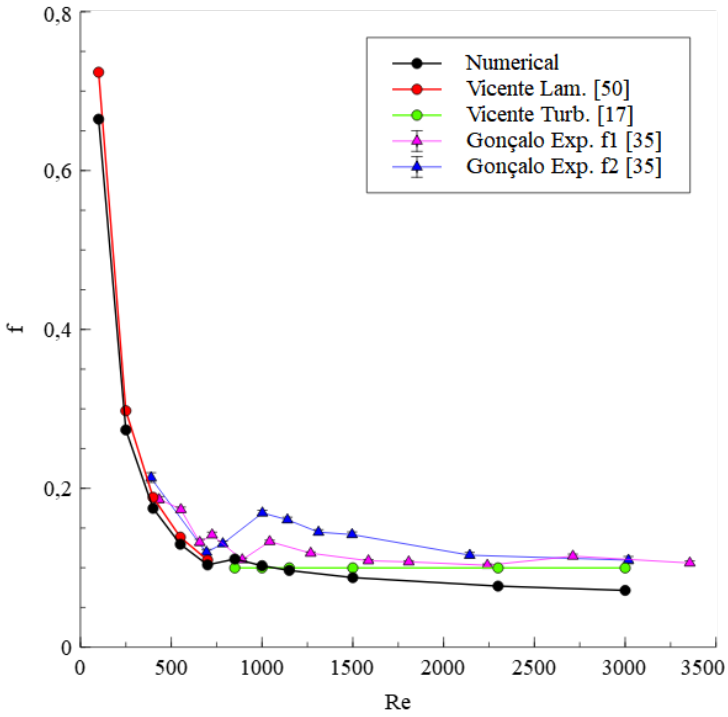

Figure 4.1: Isothermal friction factor of the helical corrugated tube with $p = 12$ mm and $e = 0.4$ mm

For the tube with $9\ mm$ pitch and $0.4\ mm$ corrugation height (Fig. 4.2) it is possible to observe that

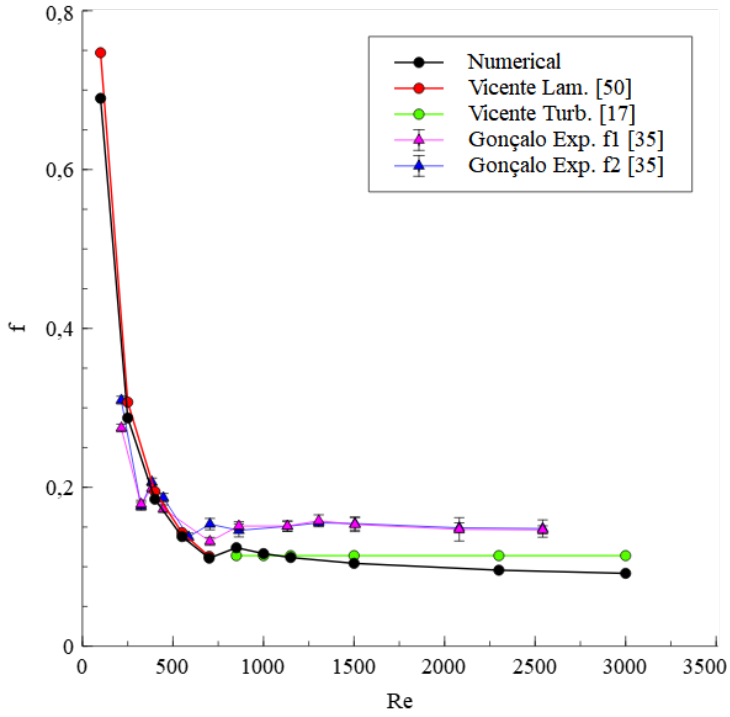

Figure 4.2: Isothermal friction factor of the helical corrugated tube with $p = 9$ mm and $e = 0.4$ mm

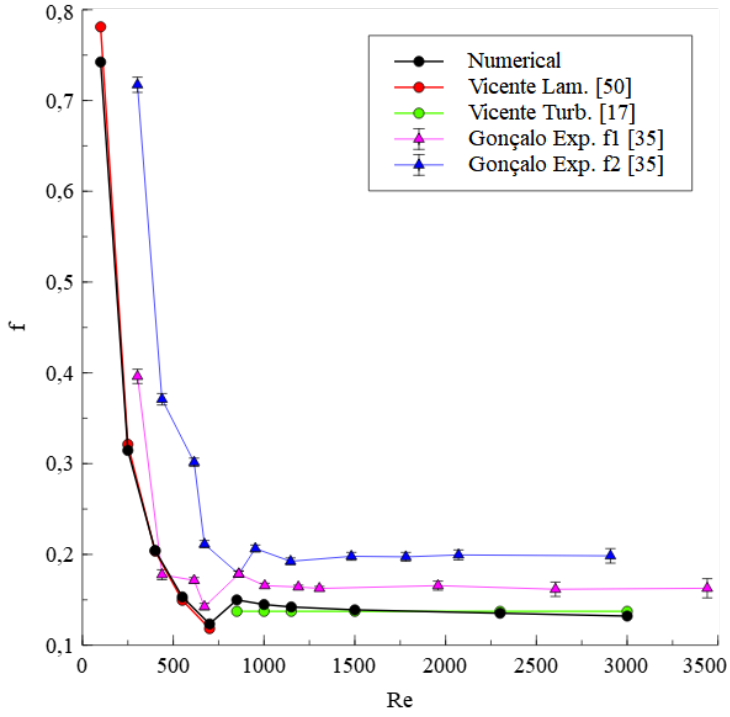

Figure 4.3: Isothermal friction factor of the helical corrugated tube with $p = 6$ mm and $e = 0.4$ mm

the maximum relative error of the numerical data compared to the empirical one is 7.7% at $Re = 100$ decreasing until 2% at $Re = 700$.

Finally, for the tube with $6\ mm$ pitch and $0.4\ mm$ corrugation height (Fig. 4.3) it is possible to observe that the maximum relative error of the numerical data compared to the empirical one is 5% at $Re = 100$,

decreasing until 0.4% at $Re = 400$ and again increasing to 4.3% at $Re = 700$.

These errors indicate that for these three tubes there is a higher accuracy for the laminar friction factor results for a higher laminar Reynolds number.

For the turbulent regime ($Re = 850 - 3000$ in green) the numerical data was compared to the turbulent friction factor correlation 2.40 obtained by Vicente et al. [17]. In this case, as the correlation depends not only of Re' and Pr but also the Severity Index ϕ, Vicente et al. [17] advises to evaluate the turbulent regime at a constant Reynolds number of 8000 which was considered for all the tubes due to all the calculated severity indexes (table 3.1) being $\phi > 10^{-3}$ (considered a medium-high corrugation).

In this range, comparing Vicente's turbulent correlation to the turbulent numerical results for the tube with $12\ mm$ pitch and $0.4\ mm$ corrugation height (Fig. 4.1) it is possible to observe that the maximum relative error of the numerical data compared to the empirical one is 28.4% at $Re = 3000$ decreasing until 2.7% at $Re = 1000$ and again increasing to 11.2% at $Re = 850$.

For the tube with $9\ mm$ pitch and $0.4\ mm$ corrugation height (Fig. 4.2) it is possible to observe that the maximum relative error of the numerical data compared to the empirical one is 19.5% at $Re = 3000$ decreasing until 2.1% at $Re = 1150$ and again increasing to 8.9% at $Re = 850$.

Finally, for the tube with $6\ mm$ pitch and $0.4\ mm$ corrugation height (Fig. 4.3) it is possible to observe that the maximum relative error of the numerical data compared to the empirical one is 9.1% at $Re = 850$, decreasing until 1.2% at $Re = 1500$ and again increasing to 3.8% at $Re = 3000$.

The high relative error at $Re = 850$ in the three cases is cause of the proximity to the transition region. One can also verify that the higher the turbulent Re the higher the relative error (opposite to what it is expected) which can be explained by the fact that it is used a constant Vicente turbulent correlation due to low turbulent Reynolds numbers.

As already mentioned Cruz [35] performed some experimental studies and used the testing kit illustrated at Fig. 4.4 where the pressure drop ($\Delta P1$) was measured from the inlet of the test section to the outlet (which represents a length of $780\ mm$) and the pressure drop ($\Delta P2$) was measured from the last third of the test section to the outlet of it with pressure sensors.

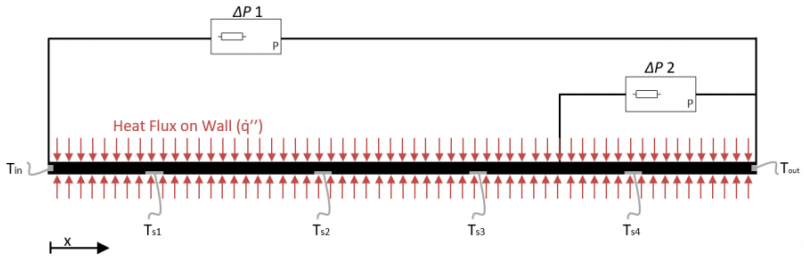

Figure 4.4: Experimental test section scheme [35]

With the test Cruz verified that hydrodynamic fully developed conditions in the tested corrugated tubes could be fully assured in the last third of the test section (friction factor f_2). These conditions are represented in the plots by the blue curve. Pink line represents the experimental friction factor f_1 through the whole testing tube.

Comparing these empirical results with the numerical friction factor results for the 3 corrugated tubes with $0.4\ mm$ corrugation height and 12, 9 and $6\ mm$ pitch (Fig. 4.1, 4.2 and 4.3 above) one can observe that the experimental friction factor f_2 has always higher values than the numerical ones (over estimated). Cruz says that this happens due to welding problems either in the tube connections or eventual not visible leaks in sensors.

Note that experimental friction factor f_2 has always higher values then the experimental friction factor f_1 being an exception the corrugated tube with $9\ mm$ pitch and $0.4\ mm$ corrugation height which has the two lines practically overlapped.

Despite the empirical results uncertainty not covering the numerical results one can affirm that the flow regimes in each case have a good compatibility for the flow behavior described by the numerical results emphasizing also the transition region for each case (which confirms a good decision for the transition range). In this case friction factor f_1 for the three cases fits better the transition region than the friction factor f_2. Note that the empirical results uncertainty is represented at Fig. 4.1, 4.2 and 4.3 however due to very small variation it may be difficult to see it in some cases.

In general, for the three cases, friction factor f_1 fits better all the numerical results which is in accordance with Cruz [35] work. Through Vicente's formulas and Cruz's experimental data one can affirm that the 3 corrugated tubes with $0.4\ mm$ corrugation height and 12, 9 and $6\ mm$ pitch are hydrodynamically validated.

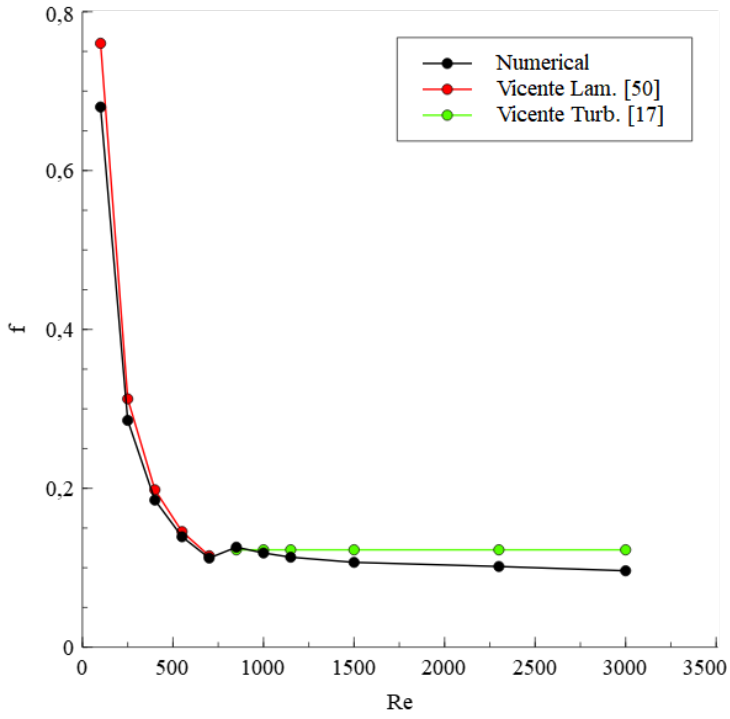

Figure 4.5: Isothermal friction factor of the helical corrugated tube with $p = 12$ mm and $e = 0.5$ mm

Now, one can perform the same analysis for the remaining corrugated tubes. Note that the following corrugated tubes with 0.5 and 0.6 corrugation heights do not have empirical data from Cruz for validation.

Being that said, for the laminar regime ($Re = 100 - 700$), comparing Vicente's laminar correlation to

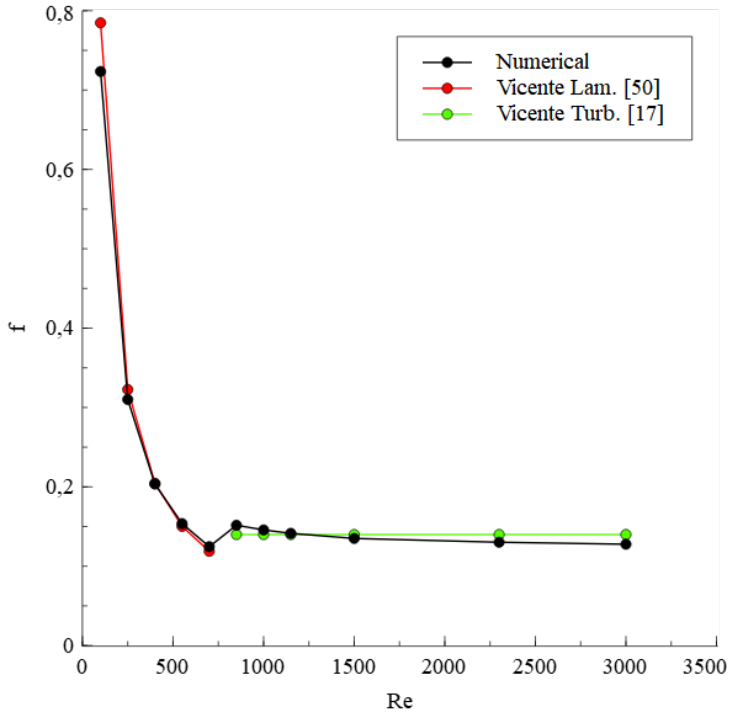

Figure 4.6: Isothermal friction factor of the helical corrugated tube with $p = 9$ mm and $e = 0.5$ mm

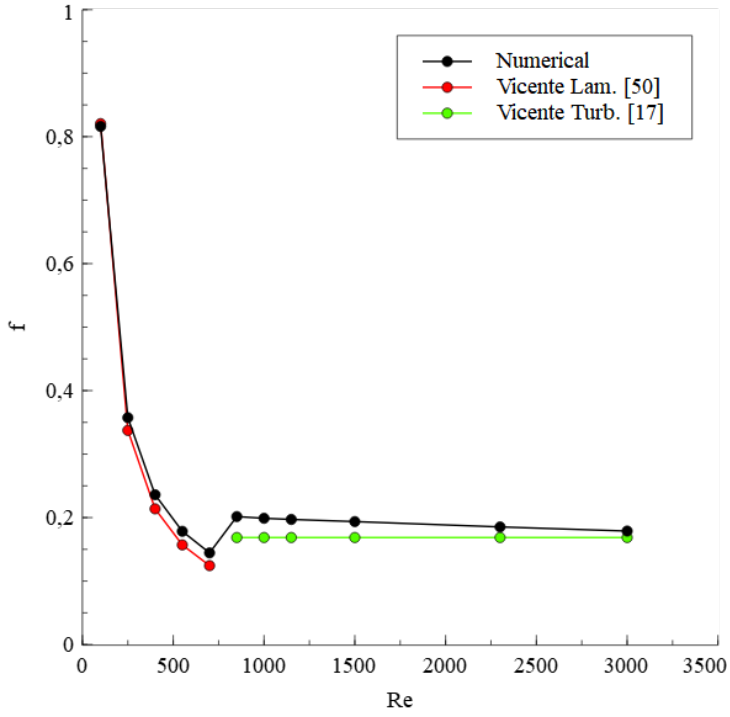

Figure 4.7: Isothermal friction factor of the helical corrugated tube with $p = 6$ mm and $e = 0.5$ mm

the laminar numerical results for the tube with $12\ mm$ pitch and $0.5\ mm$ corrugation height (Fig. 4.5) it is possible to observe that the maximum relative error of the numerical data compared to the empirical one is 10.6% at $Re = 100$ decreasing until 2.5% at $Re = 700$.

For the tube with $9\ mm$ pitch and $0.5\ mm$ corrugation height (Fig. 4.6) it is possible to observe that

the maximum relative error of the numerical data compared to the empirical one is 7.8% at $Re = 100$, decreasing until 0.5% at $Re = 400$ and again increasing to 4.9% at $Re = 700$.

Finally, for the tube with $6\ mm$ pitch and $0.5\ mm$ corrugation height (Fig. 4.7) it is possible to observe that the maximum relative error of the numerical data compared to the empirical one, opposite to the previous two tubes, is 16.2% at $Re = 700$, decreasing until 0.5% at $Re = 100$.

These relative errors indicate that the tubes with 12 and $9\ mm$ pitch and $0.5\ mm$ corrugation height also have a higher accuracy for the laminar friction factor results for a higher laminar Reynolds number which is opposite to the one with $6\ mm$ pitch and $0.5\ mm$ corrugation height. In this last case the convergence for some Re can be improved to reduce the relative error.

For the turbulent regime ($Re = 850 - 3000$), comparing Vicente's turbulent correlation to the turbulent numerical results for the tube with $12\ mm$ pitch and $0.5\ mm$ corrugation height (Fig. 4.5) it is possible to observe that the maximum relative error of the numerical data compared to the empirical one is 21.6% at $Re = 3000$ decreasing until 2.7% at $Re = 850$.

For the tube with $9\ mm$ pitch and $0.5\ mm$ corrugation height (Fig. 4.6) it is possible to observe that the maximum relative error of the numerical data compared to the empirical one is 8.7% at $Re = 3000$ decreasing until 1.1% at $Re = 1150$ and again increasing to 8.3% at $Re = 850$.

Finally, for the tube with $6\ mm$ pitch and $0.5\ mm$ corrugation height (Fig. 4.7) it is possible to observe that the maximum relative error of the numerical data compared to the empirical one is 19.6% at $Re = 850$, decreasing until 6.1% at $Re = 3000$.

The high relative error at $Re = 850$ in the tubes with 9 and $6\ mm$ pitch and $0.5\ mm$ corrugation height is because of the proximity to the transition region. One can also verify that the higher the turbulent Re the higher the relative error in the tubes with 12 and $9\ mm$ pitch and $0.5\ mm$ corrugation height (opposite to what it is expected) which can be explained by the fact that it is used a constant Vicente turbulent correlation due to low turbulent Reynolds numbers. This case does not happen to the tube tubes with $6\ mm$ pitch and $0.5\ mm$ corrugation height.

Due to the similarity in the flow profiles and relative errors to the $0.4\ mm$ corrugated tubes, the 3 corrugated tubes with $0.5\ mm$ corrugation height and 12, 9 and $6\ mm$ pitch can be considered hydrodynamically validated.

Now for the last three tubes, for the laminar regime ($Re = 100 - 700$), comparing Vicente's laminar correlation to the laminar numerical results for the tube with $12\ mm$ pitch and $0.6\ mm$ corrugation height (Fig. 4.8) it is possible to observe that the maximum relative error of the numerical data compared to the empirical one is 11.5% at $Re = 100$ decreasing until 2.1% at $Re = 700$.

For the tube with $9\ mm$ pitch and $0.6\ mm$ corrugation height (Fig. 4.9) it is possible to observe that the maximum relative error of the numerical data compared to the empirical one is 13% at $Re = 700$, decreasing until 1.6% at $Re = 250$ and again increasing to 5.9% at $Re = 100$.

Finally, for the tube with $6\ mm$ pitch and $0.6\ mm$ corrugation height (Fig. 4.10) it is possible to observe that the maximum relative error of the numerical data compared to the empirical one is 31% at $Re = 700$, decreasing until 7.2% at $Re = 100$.

These relative errors indicate that the tube with $12\ mm$ pitch and $0.6\ mm$ corrugation height also

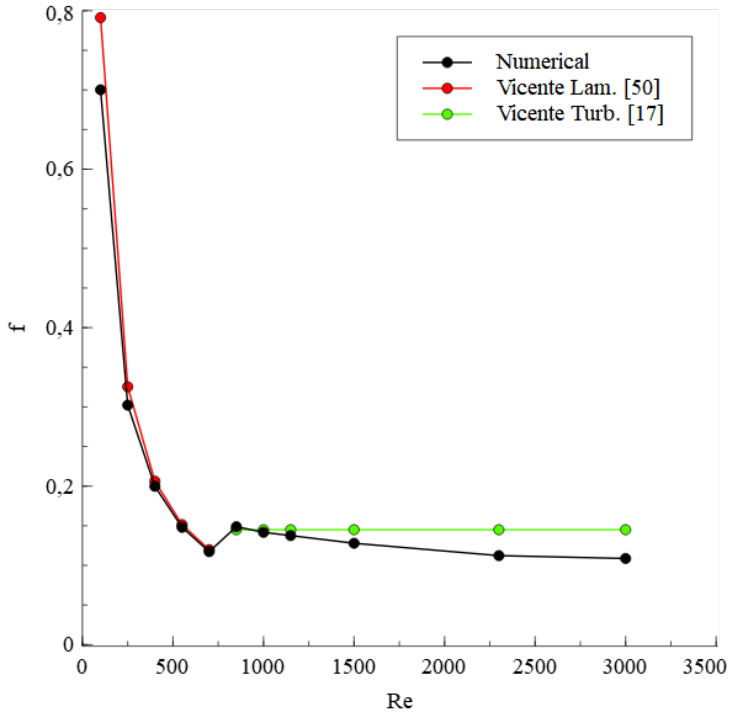

Figure 4.8: Isothermal friction factor of the helical corrugated tube with $p = 12$ mm and $e = 0.6$ mm

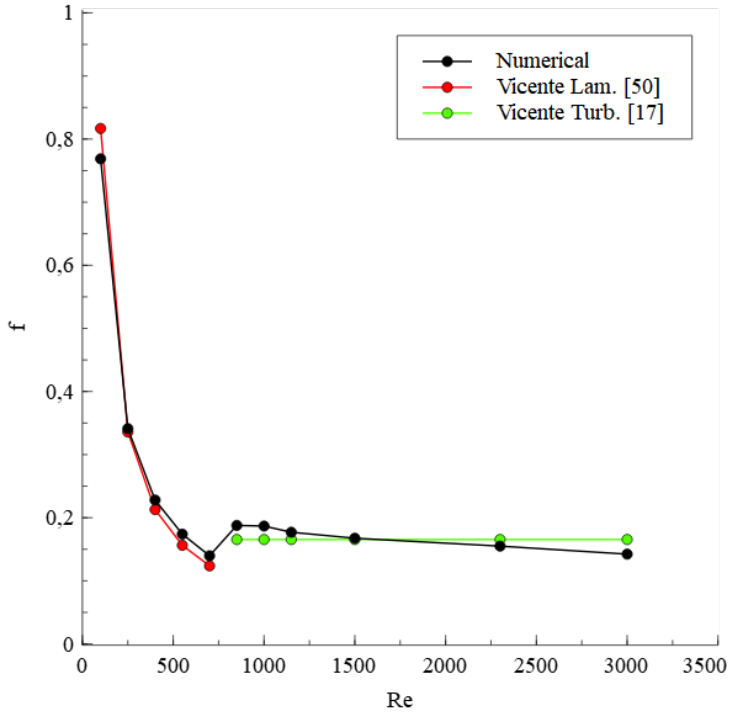

Figure 4.9: Isothermal friction factor of the helical corrugated tube with $p = 9$ mm and $e = 0.6$ mm

have a higher accuracy for the laminar friction factor results for a higher laminar Reynolds number. The opposite happens to the ones with 9 and $6\ mm$ pitch and $0.6\ mm$ corrugation height. In these two last cases the convergence for some Re can be improved to reduce the relative error.

For the turbulent regime ($Re = 850 - 3000$), comparing Vicente's turbulent correlation to the turbulent

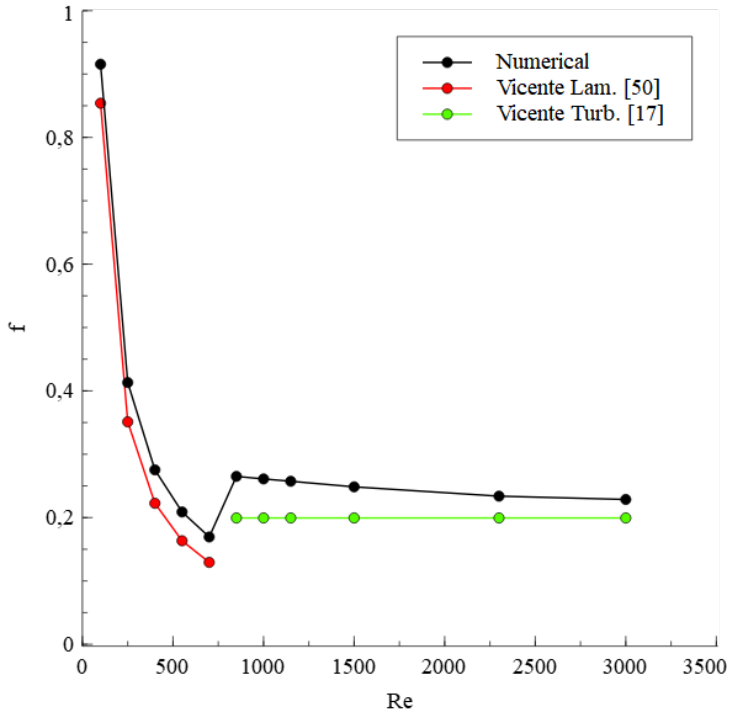

Figure 4.10: Isothermal friction factor of the helical corrugated tube with $p = 6$ mm and $e = 0.6$ mm

numerical results for the tube with $12\ mm$ pitch and $0.6\ mm$ corrugation height (Fig. 4.8) it is possible to observe that the maximum relative error of the numerical data compared to the empirical one is 25% at $Re = 3000$, decreasing until 2.2% at $Re = 1000$ and increasing again 2.7% at $Re = 850$.

For the tube with $9\ mm$ pitch and $0.6\ mm$ corrugation height (Fig. 4.9) it is possible to observe that the maximum relative error of the numerical data compared to the empirical one is 14% at $Re = 3000$ decreasing until 1.2% at $Re = 1500$ and again increasing to 13.5% at $Re = 850$.

Finally, for the tube with $6\ mm$ pitch and $0.6\ mm$ corrugation height (Fig. 4.10) it is possible to observe that the maximum relative error of the numerical data compared to the empirical one is 32.9% at $Re = 850$, decreasing until 14.7% at $Re = 3000$.

The high relative error at $Re = 850$ in the tubes with 9 and $6\ mm$ pitch and $0.6\ mm$ corrugation height is because of the proximity to the transition region. One can also verify that the higher the turbulent Re the higher the relative error in the tubes with 12 and $9\ mm$ pitch and $0.6\ mm$ corrugation height (opposite to what it is expected) which once again can be explained by the fact that it is used a constant Vicente turbulent correlation due to low turbulent Reynolds numbers. This case does not happen to the tube tubes with $6\ mm$ pitch and $0.6\ mm$ corrugation height.

Once again, due to the similarity of the flow profiles and relative errors to the $0.4\ mm$ corrugated tubes, the 3 corrugated tubes with $0.6\ mm$ corrugation height and 12, 9 and $6\ mm$ pitch can be considered hydrodynamically validated.

4.1.2 Nusselt number

Taking the same approach for the average Nusselt number, one can also start by inspecting the three tubes with $0.4\ mm$ corrugation height and 12, 9 and $6\ mm$ pitch (Fig. 4.11, 4.12 and 4.13 below).

As explained for the smooth tube validation, in order to determine the numerical average Nusselt number different parameters are needed to obtain through numerical analysis. It was made a surface average report on the wet surface to determine the wall temperature (T_w), a mass flow average report on the inlet interface surface to determine the mean inflow temperature ($T_{m,i}$) and a mass flow average report on the outlet interface surface to determine the mean outflow temperature ($T_{m,o}$). Then equation 2.21 was used to obtain the convective heat transfer coefficient (h). Note that the mean temperature (T_m) was determined through the average $(T_{m,i}+T_{m,o})/2$. One can accept these values since there is a small size domain (small corrugated tubes) where the inflow and the outflow temperatures are very close (more a linear temperature growth which in comparison to a long tube will have a logarithmic growth). One should also note that $T_s = T_w$. Finally, with h, using equation 2.36, where $D = D_h$ (hydraulic diameter) and k from table 3.4, the numerical Nusselt number is calculated.

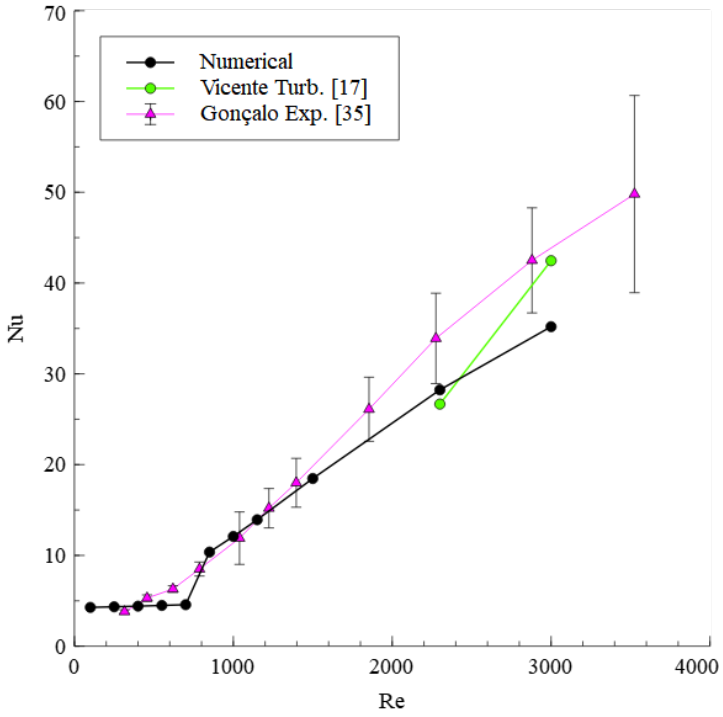

Figure 4.11: Nusselt number of the helical corrugated tube with $p = 12$ mm and $e = 0.4$ mm

In each Fig. 4.11, 4.12 and 4.13 there is a pink line that represents Cruz [35] experimental results.

For the laminar regime ($Re = 100 - 700$) one can observe that the numerical results have a similar behavior as the smooth tube laminar regime which means that the heat transfer is almost constant. In the other hand, for the experimental laminar results, the higher the Re the higher the Nu. This happens because Cruz's experimental setup wasn't long enough to allow the flow to assure thermal fully developed conditions which were only guaranteed for the turbulent regime.

Relative to the transition region it is clear that the same was well defined for the three tubes once the

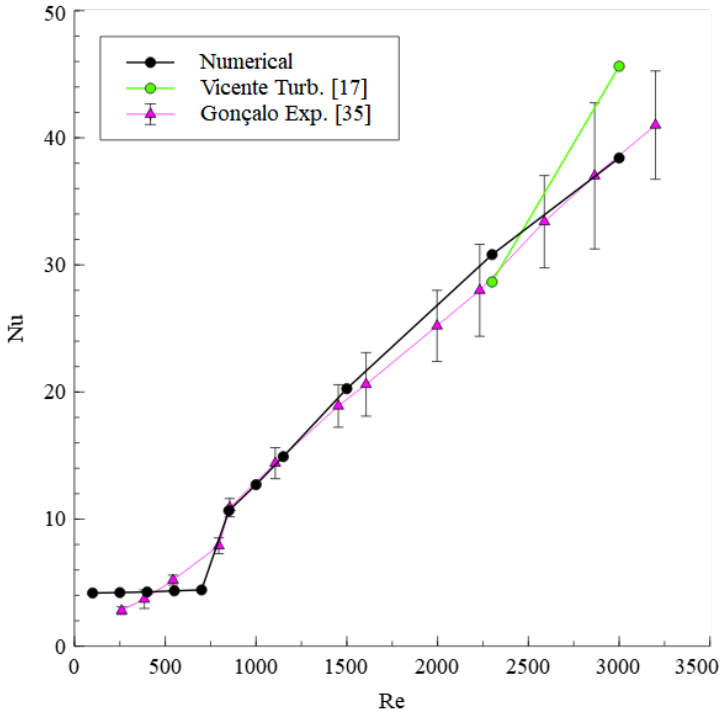

Figure 4.12: Nusselt number of the helical corrugated tube with $p = 9$ mm and $e = 0.4$ mm

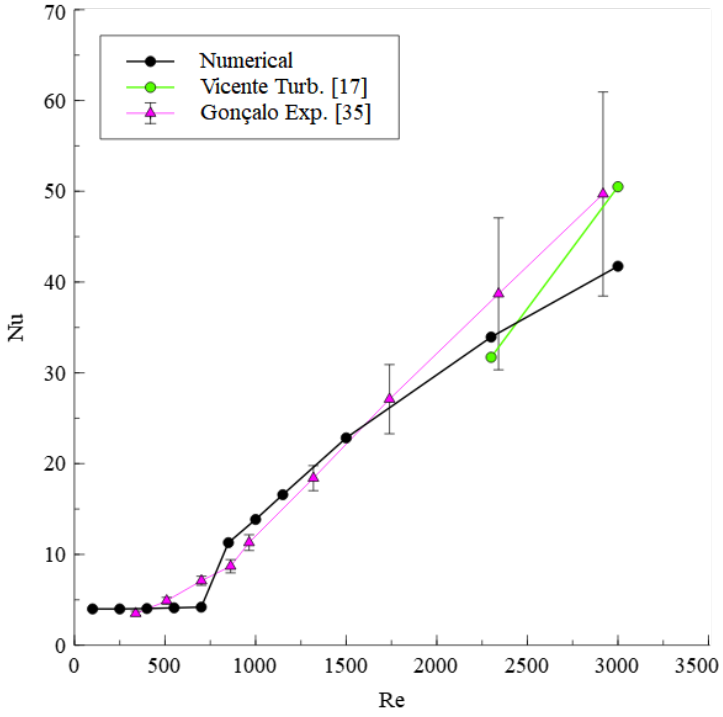

Figure 4.13: Nusselt number of the helical corrugated tube with $p = 6$ mm and $e = 0.4$ mm

experimental curve fits well the numerical data.

Now for the turbulent regime, $Re = 850 - 3000$ the same behaviour of the smooth tube is also obtained. As can be observed the Nu starts to grow rapidly after the transition which implies that there is a higher heat transfer through the corrugated tube wall, being this one higher for a higher Re. The

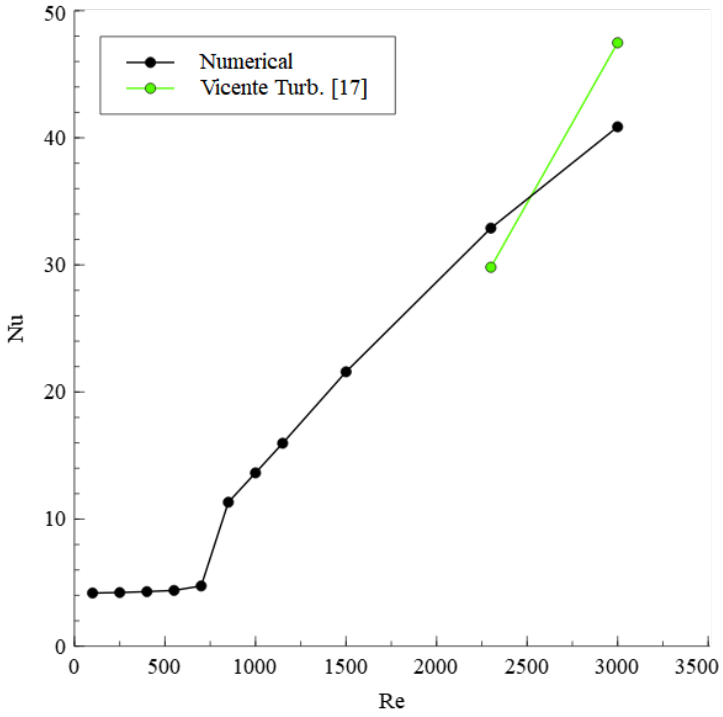

Figure 4.14: Nusselt number of the helical corrugated tube with $p = 12$ mm and $e = 0.5$ mm

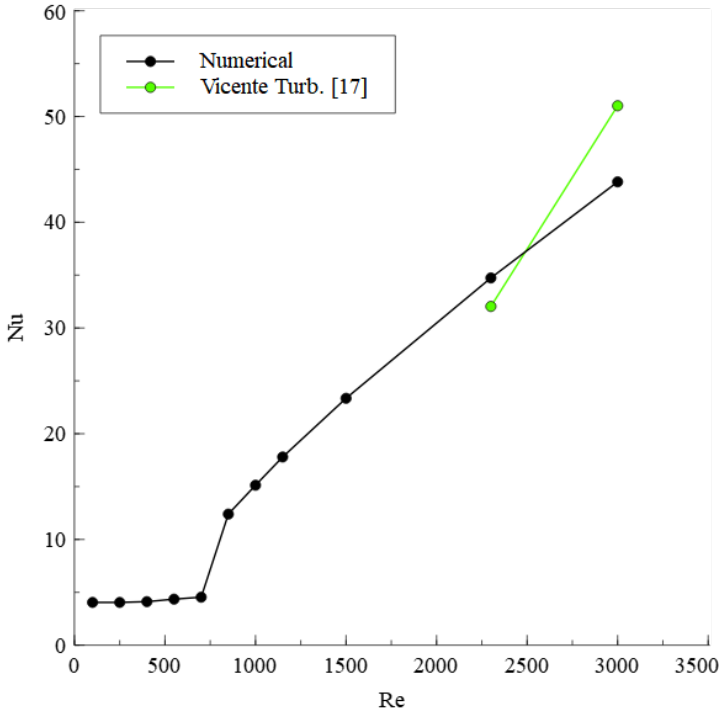

Figure 4.15: Nusselt number of the helical corrugated tube with $p = 9$ mm and $e = 0.5$ mm

experimental data uncertainty has a good fitting for the numerical data in this regime.

The numerical results in the turbulent regime were also compared to the Vicente's turbulent Nusselt correlation 2.41. As the turbulent Vicente's friction factor, this correlation is also only valid for a very high Reynolds numbers ($Re' = 8000 - 60000$). However, the expression was used for Reynolds 2300 and

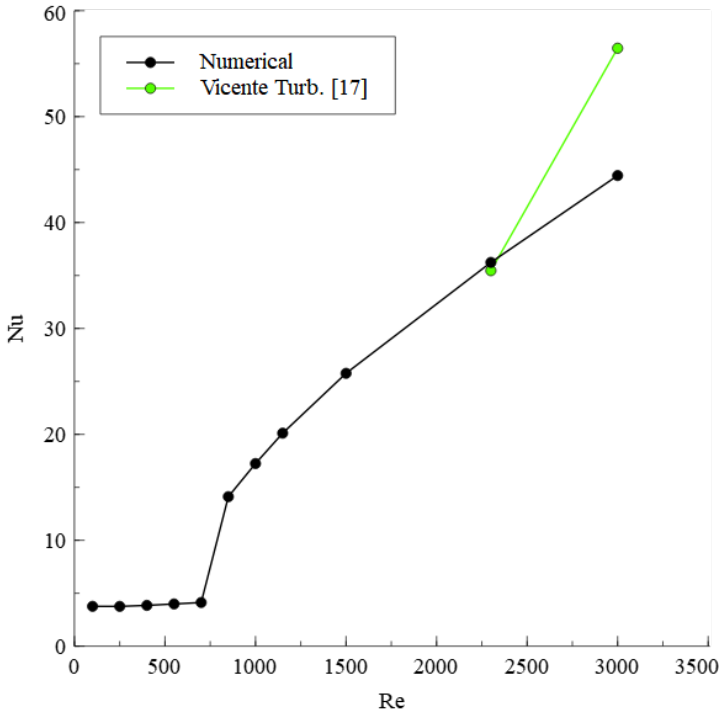

Figure 4.16: Nusselt number of the helical corrugated tube with $p = 6$ mm and $e = 0.5$ mm

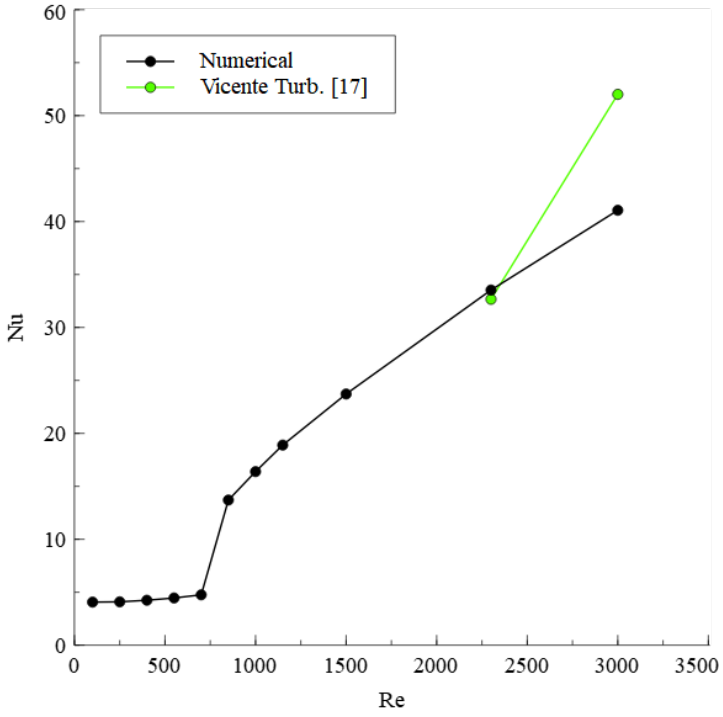

Figure 4.17: Nusselt number of the helical corrugated tube with $p = 12$ mm and $e = 0.6$ mm

3000 once other way there would not exist any correlations to cover this regime.

Comparing the correlation's results for these two Reynolds numbers to the turbulent numerical results of the tubes with $0.4\ mm$ corrugation height and 12, 9 and $6\ mm$ pitch one can obtain the following relative errors: 5.9% and 17.1% (Fig. 4.11), 7.5% and 15.8% (Fig. 4.12) and 7% and 17.3% (Fig. 4.13)

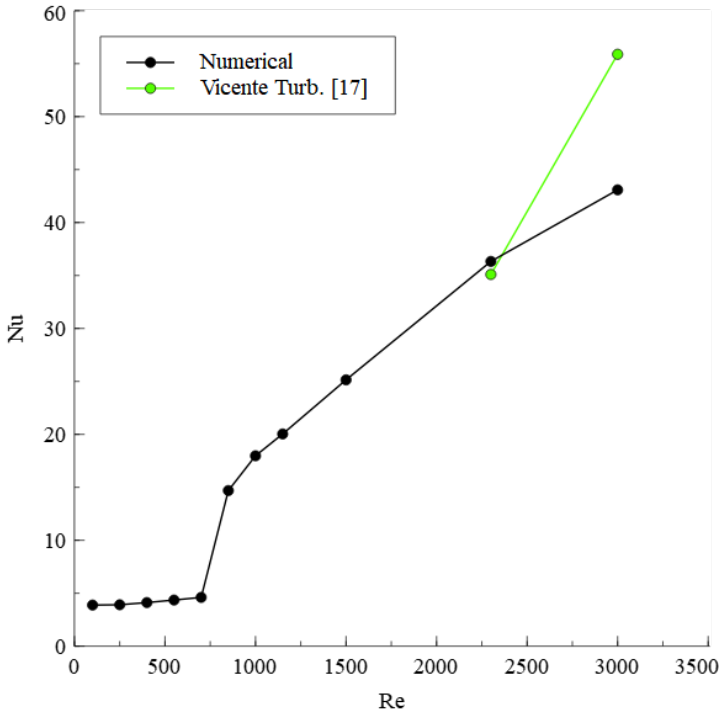

Figure 4.18: Nusselt number of the helical corrugated tube with $p = 9$ mm and $e = 0.6$ mm

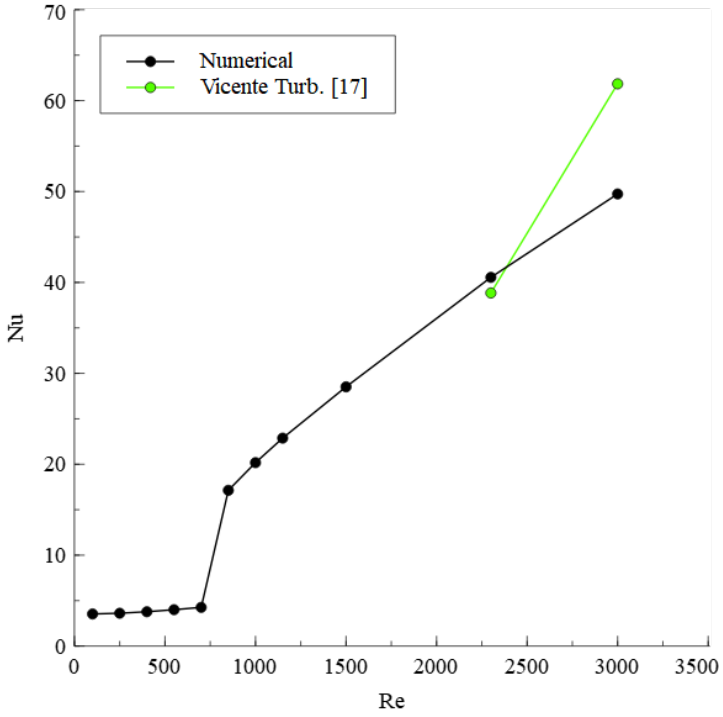

Figure 4.19: Nusselt number of the helical corrugated tube with $p = 6$ mm and $e = 0.6$ mm

respectively.

As it is possible to verify the relative errors are very high which can be justified due to the fact that the correlation is being used for too low Reynolds numbers.

There were not found any empirical correlations for the laminar regime for the average Nusselt num-

ber for the corrugated tubes. Despite that, with the good fitting of the numerical results with Cruz's experimental data for the tubes with $0.4\ mm$ corrugation height and 12, 9 and $6\ mm$ pitch, one can consider that these tubes are thermally validated.

Now the same analysis can be performed for the remaining tubes (only turbulent regime due to lack of laminar correlations).

For the tubes with $0.5\ mm$ corrugation height and 12, 9 and $6\ mm$ pitch, and for Reynolds 2300 and 3000, one can obtain the following relative errors: 10.3% and 13.9% (Fig. 4.14), 8.4% and 14.1% (Fig. 4.15) and 2.2% and 21.3% (Fig. 4.16) respectively.

Then for the tubes with $0.6\ mm$ corrugation height and 12, 9 and $6\ mm$ pitch, and for Reynolds 2300 and 3000, one can obtain the following relative errors: 2.7% and 21% (Fig. 4.17), 3.5% and 22.9% (Fig. 4.18) and 4.4% and 19.6% (Fig. 4.19) respectively.

Once again the relative errors are very high which can be justified due to the fact that the correlation is being used for too low Reynolds numbers.

Due to the lack of correlations for the laminar regime and a poor accordance of the Vicente's Nusselt turbulent correlation with the turbulent numerical Nusselt number the 3 tubes with $0.5\ mm$ corrugation height and 12, 9 and $6\ mm$ pitch and the 3 tubes with $0.6\ mm$ corrugation height and 12, 9 and $6\ mm$ pitch cannot be thermally validated. Empirical analysis should be done to thermally verify each one of them.

Despite the non-validation, the results will still be used to find the optimum working conditions of the corrugated tubes comparing to the smooth tube isothermal friction factor and average Nusselt number.

4.2 f vs Re

Now that all the corrugated tubes are hydrodynamically validated one can compare them with the results obtained for the smooth tube and check what is their behavior throughout the different flow regimes.

As previously described in the beginning of the Results chapter all the data was analysed for a Reynolds range of $Re = 100-3000$. At Fig. 4.20 it is possible to observe a general view of the isothermal friction factor for the different corrugated tubes compared to the smooth tube for the full range. Note that a result for $Re = 4000$ was presented for the smooth tube once its transition region ends at $Re = 3000$ and otherwise there wouldn't be any values for the turbulent regime represented on the chart.

Having a closer look to the laminar region $Re = 100 - 700$ (Fig. 4.21) is it possible to confirm that all the corrugated tubes have a higher isothermal friction factor than the smooth tube being the tube with $6\ mm$ pitch and $0.6\ mm$ corrugation height the worst of all and the smooth tube the best. All the tubes represent the same downtrend having the highest values at a lower Re and then decreasing as we approach the transition region.

Now regarding the turbulent region $Re = 850-3000$ (Fig. 4.22) one can realize that after the transition ($Re = 700 - 850$) all the tube had an increase in the friction factor values, especially the ones with a higher corrugation height and lower pitch slightly decreasing as the Re in the turbulent region grows.

It is easy to verify that the transition region of the corrugated tubes ($Re = 700 - 850$) occurs way

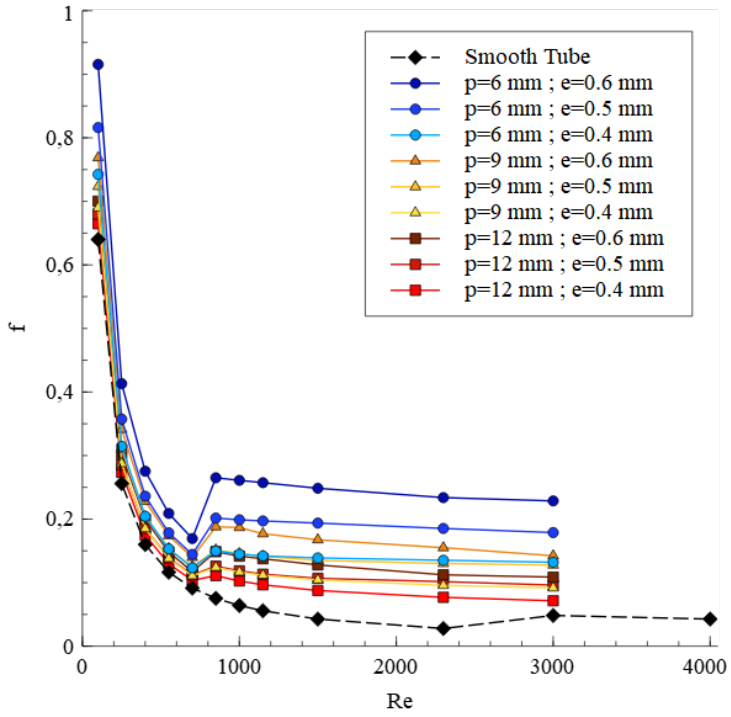

Figure 4.20: Comparison of the friction factor as function of Reynolds number for the different corrugated tubes and smooth tube

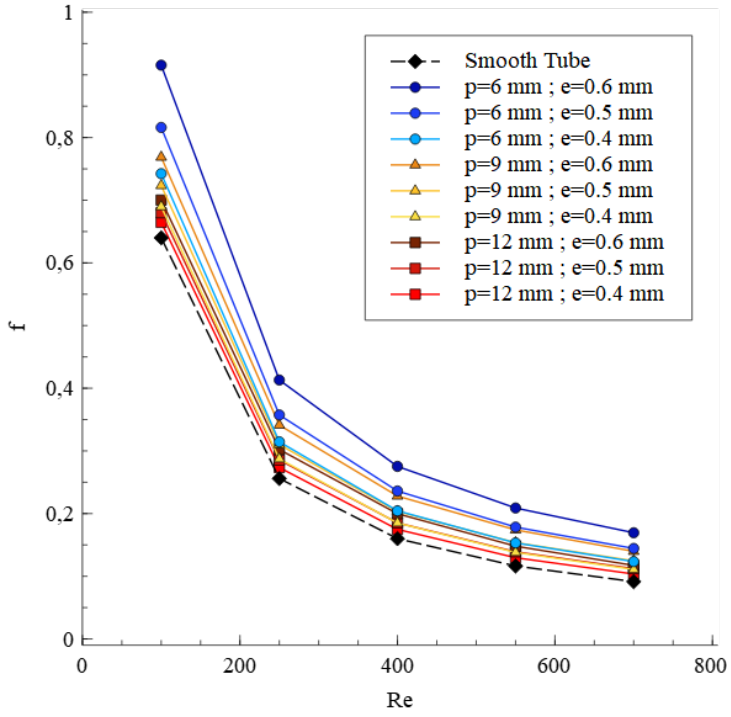

Figure 4.21: Comparison of the friction factor as function of Reynolds number for the different corrugated tubes and smooth tube - Close up $Re = 100 - 700$ (laminar regime)

sooner than the smooth tube's one ($Re = 2300 - 3000$) and therefore the smooth tube for the range of $Re = 700 - 2300$ has lower and therefore better values of isothermal friction factor once it is still in the laminar regime. However, once the smooth tube becomes turbulent the friction factor becomes very

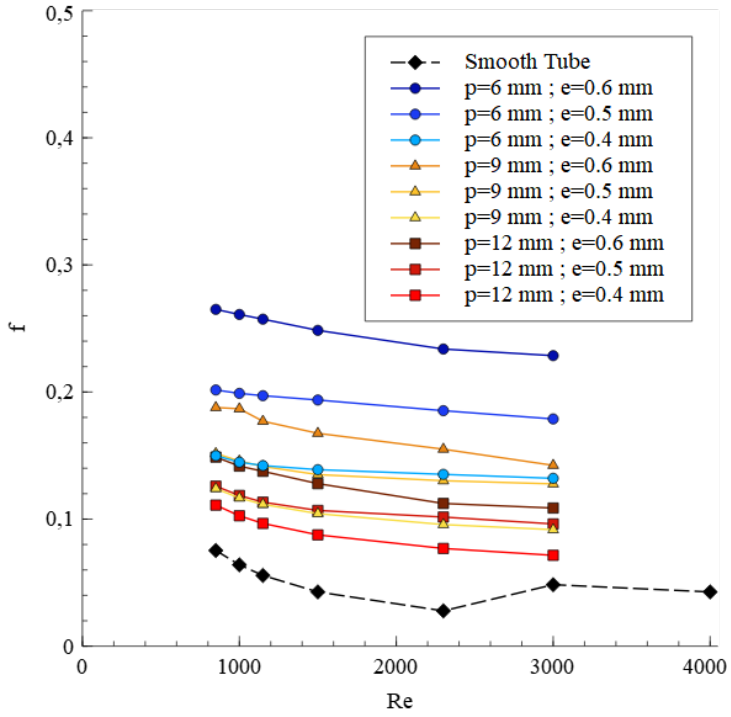

Figure 4.22: Comparison of the friction factor as function of Reynolds number for the different corrugated tubes and smooth tube - Close up $Re = 850 - 3000$ (turbulent regime)

similar but still better than all the corrugated tubes being again the tube with $6\ mm$ pitch and $0.6\ mm$ corrugation height the worst of all. The tube with $12\ mm$ pitch and $0.4\ mm$ corrugation height, despite having a higher isothermal friction factor than the smooth tube still performs better in this regime then the rest of the corrugated tubes.

4.2.1 Friction Augmentation Factor

After the qualitative analysis one can make a quantitative one through the friction augmentation factor comparison with the smooth tube. In the figure below (Fig. 4.23) it is possible to observe the general view for all the tubes for the friction augmentation factor throughout all the flow regimes and at table 4.1 all the correspondent values.

Having a closer look on the laminar and transition region (Fig. 4.24 one can verify that the tube with $12\ mm$ pitch and $0.4\ mm$ corrugation height has the closest friction values to the smooth tube having an augmentation factor of 1.04 at $Re = 100$ and 1.13 at $Re = 700$. In the other hand the tube with $6\ mm$ pitch and $0.6\ mm$ corrugation height has the highest friction values for this region compared to the smooth tube, having an augmentation factor of 1.43 at $Re = 100$ and 1.85 at $Re = 700$. As the transition occurs, either the tube with $12\ mm$ pitch and $0.4\ mm$ corrugation height and the tube with $6\ mm$ pitch and $0.6\ mm$ corrugation height increase their friction augmentation values to 1.47 and 3.52 respectively for $Re = 850$.

For the turbulent regime (Fig. 4.23) one can observe that the friction augmentation factor starts to increase more rapidly, practically in a linear way, obtaining its maximum of 8.4 at $Re = 2300$ for the tube

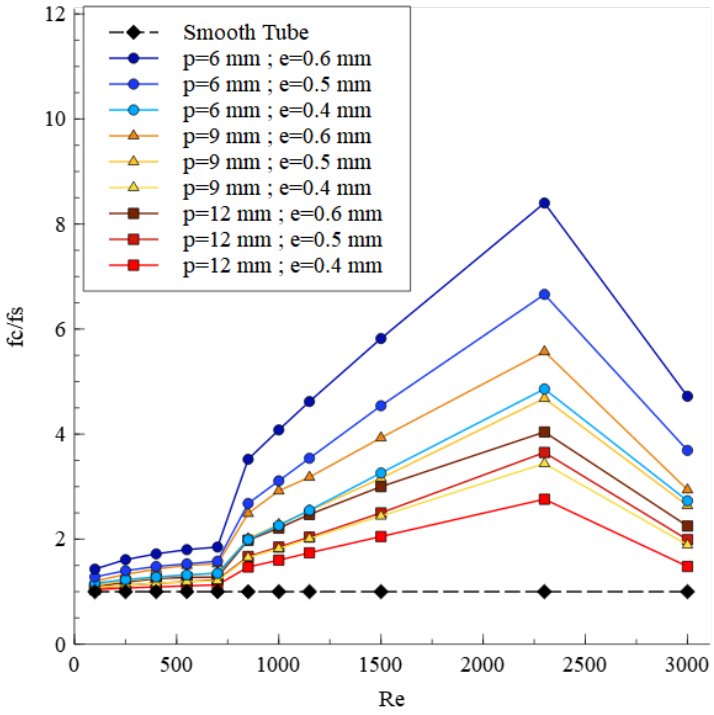

Figure 4.23: Comparison of the friction augmentation factor as function of Reynolds number for the different corrugated tubes and smooth tube

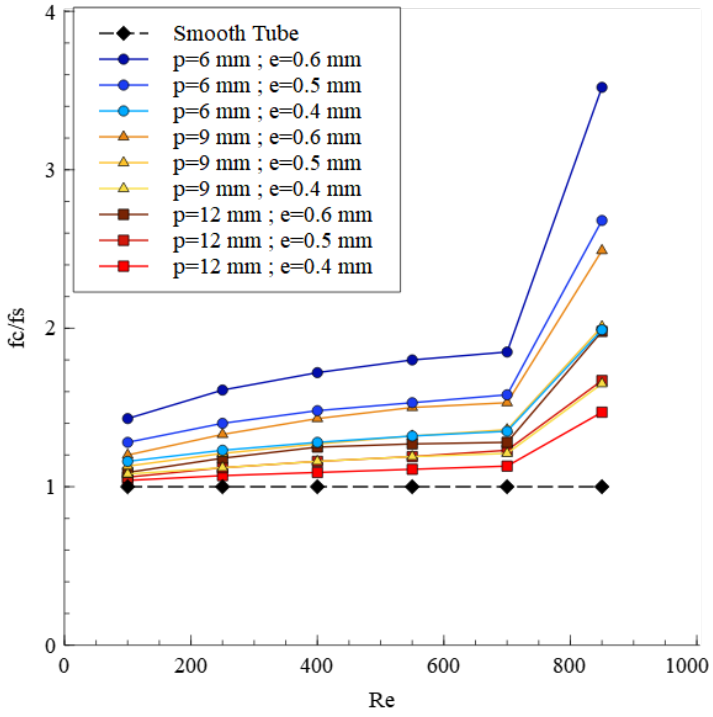

Figure 4.24: Comparison of the friction augmentation factor as function of Reynolds number for the different corrugated tubes and smooth tube - Close up $Re = 100 - 850$ (laminar and transition regime)

with $6\ mm$ pitch and $0.6\ mm$ corrugation height and for the same Re its lowest of 2.76 for the tube with $12\ mm$ pitch and $0.4\ mm$ corrugation height. Looking at the close-up represented at Fig. 4.25 it is clear that as soon as the smooth tube becomes turbulent the friction augmentation factor gets very low for all

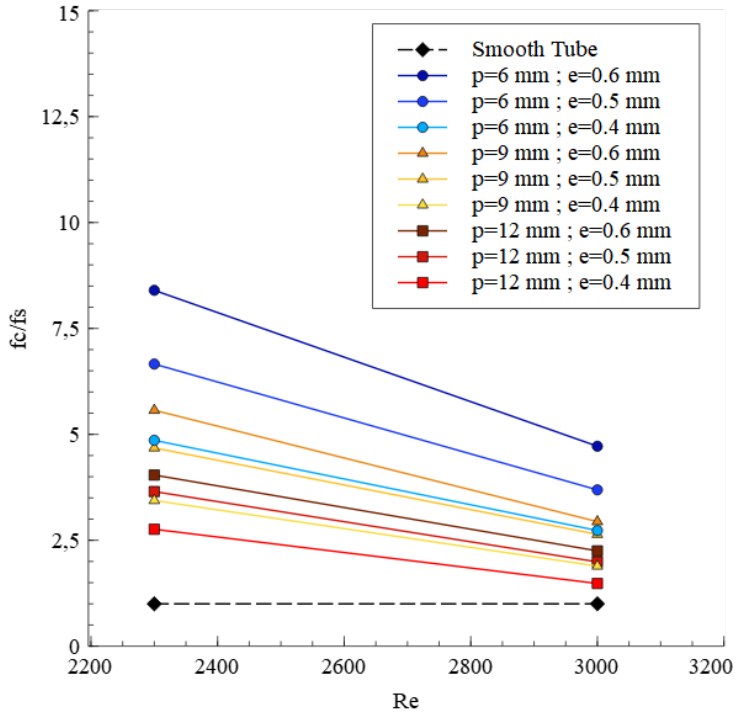

Figure 4.25: Comparison of the friction augmentation factor as function of Reynolds number for the different corrugated tubes and smooth tube - Close up $Re = 2300 - 3000$ (turbulent regime)

Table 4.1: Friction augmentation factor for the corrugated tubes compared to the smooth tube

Re	$p6e0.4/smooth$	$p6e0.5/smooth$	$p6e0.6/smooth$	$p9e0.4/smooth$	$p9e0.5/smooth$	$p9e0.6/smooth$	$p12e0.4/smooth$	$p12e0.5/smooth$	$p12e0.6/smooth$	$smooth/smooth$
100	1.16	1.28	1.43	1.08	1.13	1.20	1.04	1.06	1.09	1
250	1.23	1.40	1.61	1.12	1.21	1.33	1.07	1.12	1.18	1
400	1.28	1.48	1.72	1.16	1.27	1.43	1.09	1.16	1.25	1
550	1.32	1.53	1.80	1.19	1.32	1.50	1.11	1.19	1.27	1
700	1.35	1.58	1.85	1.21	1.36	1.53	1.13	1.23	1.28	1
850	1.99	2.68	3.52	1.65	2.01	2.49	1.47	1.67	1.98	1
1000	2.26	3.11	4.08	1.82	2.28	2.92	1.60	1.85	2.21	1
1150	2.55	3.54	4.62	2.01	2.54	3.18	1.74	2.04	2.47	1
1500	3.26	4.54	5.82	2.44	3.16	3.93	2.05	2.50	3.00	1
2300	4.86	6.66	8.40	3.44	4.68	5.57	2.76	3.65	4.04	1
3000	2.73	3.69	4.72	1.89	2.64	2.94	1.48	1.99	2.25	1

the tubes, becoming 4.72 for the tube with $6\ mm$ pitch and $0.6\ mm$ corrugation height and 1.48 for the tube with $12\ mm$ pitch and $0.4\ mm$ corrugation height.This happens due to the increase of the isothermal friction factor for the smooth tube for this region.

In conclusion, for laminar region $Re = 100 - 700$ the friction augmentation factor tends to be slightly higher for all the tubes. As the transition for the corrugated tubes occur there is a jump in the friction augmentation factor which grows almost linearly for all the cases in the range of $Re = 850 - 2300$. Then, when the smooth tube becomes turbulent $Re = 2300 - 3000$ all the friction augmentation factors decrease becoming almost as low as the laminar ones.

4.3 Nu vs Re

As concluded in the end of Nusselt section 4.1.2 not all the corrugated tubes could be thermally validated due to the lack of empirical correlations especially for the low Reynolds numbers. However, it was still

decided to use the numerical results, compare them to the smooth tube and check what is their behavior throughout the different flow regimes.

As already mentioned all the data was analysed for a Reynolds range of $Re = 100-3000$. At Fig. 4.26 it is possible to observe a general view of the average Nusselt number for the different corrugated tubes compared to the smooth tube for the full range. Note that a result for $Re = 4000$ was presented for the smooth tube once its transition region ends at $Re = 3000$ and otherwise there wouldn't be any values for the turbulent regime represented on the chart.

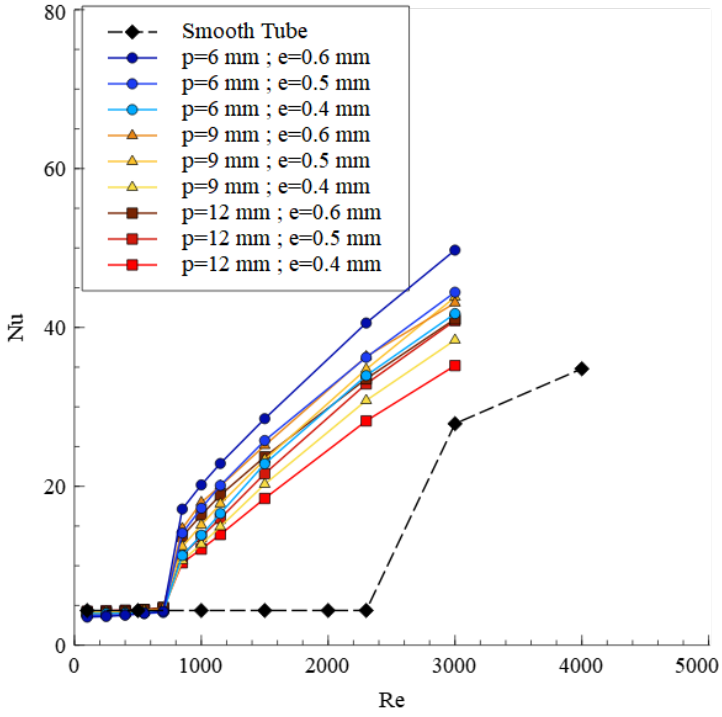

Figure 4.26: Comparison of the Nusselt number as function of Reynolds number for the different corrugated tubes and smooth tube

Having a closer look to the laminar region $Re = 100 - 700$ (Fig. 4.27) is it possible to confirm that all the corrugated tubes have in general a lower average Nusselt number than the smooth tube (opposite to what happened to the isothermal friction factor) being the tube with $6\ mm$ pitch and $0.6\ mm$ corrugation height again the worst of all.

It is known that in the laminar regime the smooth tube allows a constant heat transfer through the walls (constant Nusselt number) while for the corrugated tubes, as it is possible to observe at Fig. 4.27, they then to have an uptrend, having the tubes lower Nu values than the smooth tube until $Re \approx 300$ and then slightly higher values until the end of the laminar region at $Re = 700$ where the tube with $12\ mm$ pitch and $0.6\ mm$ corrugation height has the heighest Nu value.

Now regarding the turbulent region $Re = 850-3000$ (Fig. 4.28) one can realize that after the transition $Re = 700 - 850)$ all the tubes had an increase in the average Nusselt number, especially the ones with a higher corrugation height and lower pitch.

As per Fig. 4.26 it is easy to verify that the transition region of the corrugated tubes ($Re = 700 - 850$) occurs way sooner than the smooth tube's one ($Re = 2300 - 3000$) and therefore the smooth tube for the

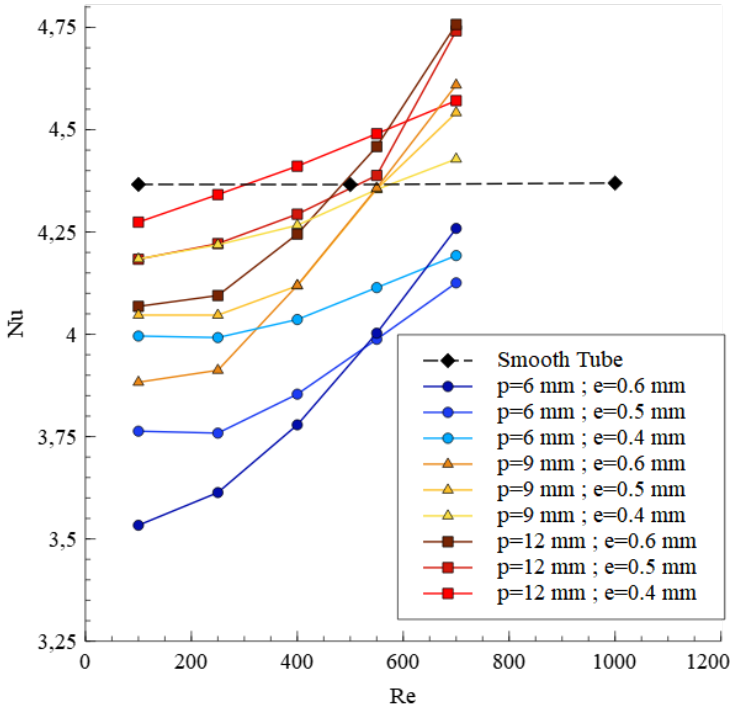

Figure 4.27: Comparison of the Nusselt number as function of Reynolds number for the different corrugated tubes and smooth tube - Close up $Re = 100 - 700$ (laminar regime)

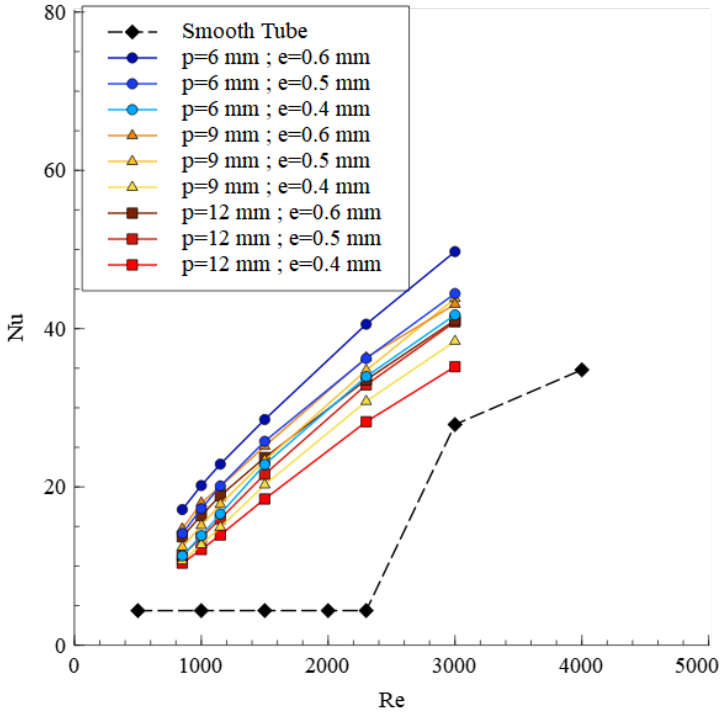

Figure 4.28: Comparison of the Nusselt number as function of Reynolds number for the different corrugated tubes and smooth tube - Close up $Re = 850 - 3000$ (turbulent regime)

range of $Re = 700 - 2300$ has way lower and therefore worst values of average Nusselt number once it is still in the laminar regime. Once the smooth tube becomes turbulent (Fig. 4.28) the Nu jumps in value and keeps a constant growth. However it still under performs all the corrugated tubes being again the

tube with $6\ mm$ pitch and $0.6\ mm$ corrugation height now the best of all in terms of heat transfer. The tube with $12\ mm$ pitch and $0.4\ mm$ corrugation height has the lowest Nu of all the corrugated tubes in this regime but is still better than the smooth tube.

4.3.1 Nusselt Augmentation Factor

So in the same way, after the qualitative analysis one can make a quantitative one through the Nusselt augmentation factor comparison with the smooth tube. In the figure below (Fig. 4.29) it is possible to observe the general view for all the tubes for the Nusselt augmentation factor throughout all the flow regimes and at table 4.2 all the correspondent values.

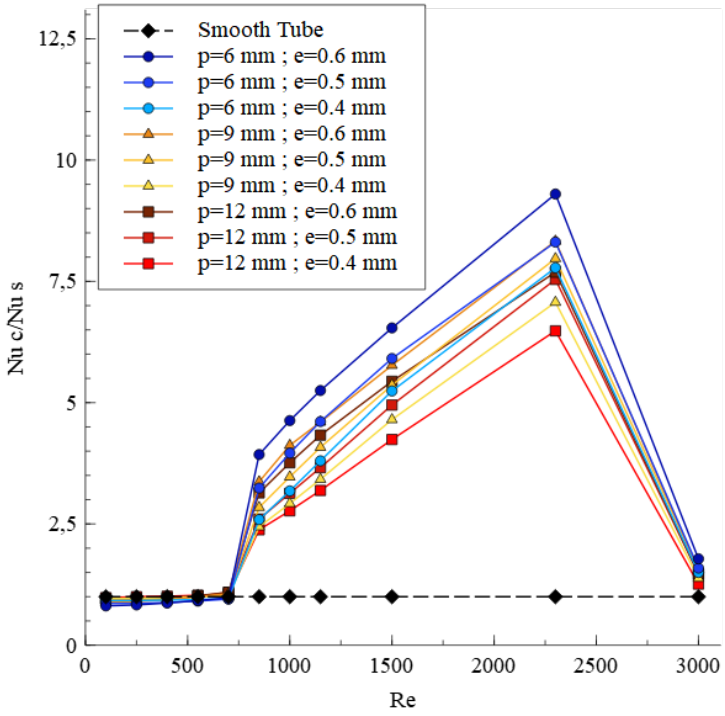

Figure 4.29: Comparison of the Nusselt augmentation factor as function of Reynolds number for the different corrugated tubes and smooth tube

Having a closer look on the laminar and transition region (Fig. 4.30 one can verify that in general all the corrugated tubes similar but slightly lower values of Nu augmentation factor compared to the smooth tube. The tube with $6\ mm$ pitch and $0.6\ mm$ corrugation height has the lowest augmentation factor for this region, having an augmentation factor of 0.81 at $Re = 100$ and 0.98 at $Re = 700$. As already seen, for some of the corrugated tubes, for $Re > 300$, the Nu augmentation factor has an improvement but still very close to the smooth tube's heat transfer capability. So for $Re = 700$ (at the end of the laminar region) the tube with $12\ mm$ pitch and $0.6\ mm$ corrugation height obtains the maximum augmentation of 1.09.

As the transition occurs, the tube with $6\ mm$ pitch and $0.6\ mm$ corrugation height becomes the one with the highest Nu augmentation factor, with 3.93 at $Re = 850$ and the tube with $12\ mm$ pitch and $0.4\ mm$ corrugation height becomes the worst with a Nu augmentation factor of 2.38 for $Re = 850$. All

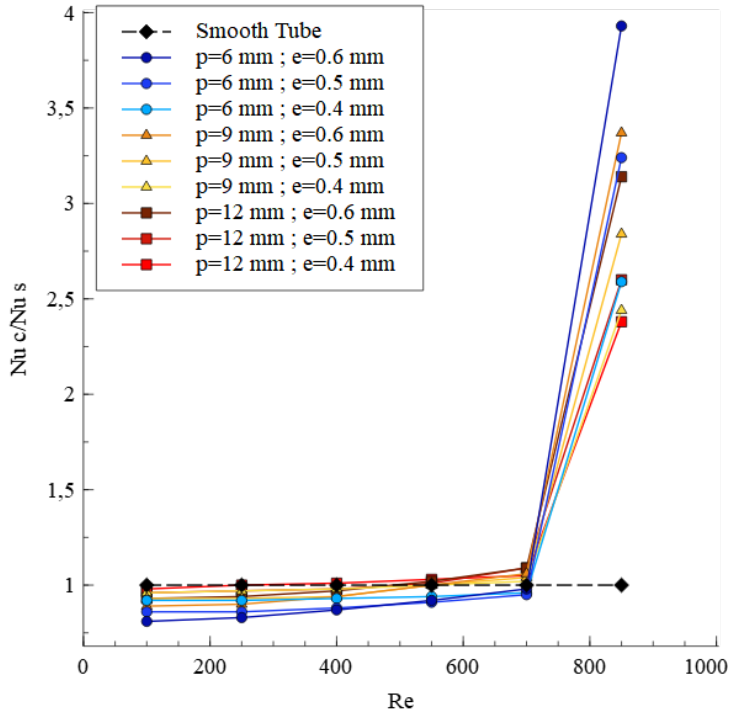

Figure 4.30: Comparison of the Nusselt augmentation factor as function of Reynolds number for the different corrugated tubes and smooth tube - Close up $Re = 100 - 850$ (laminar and transition regime)

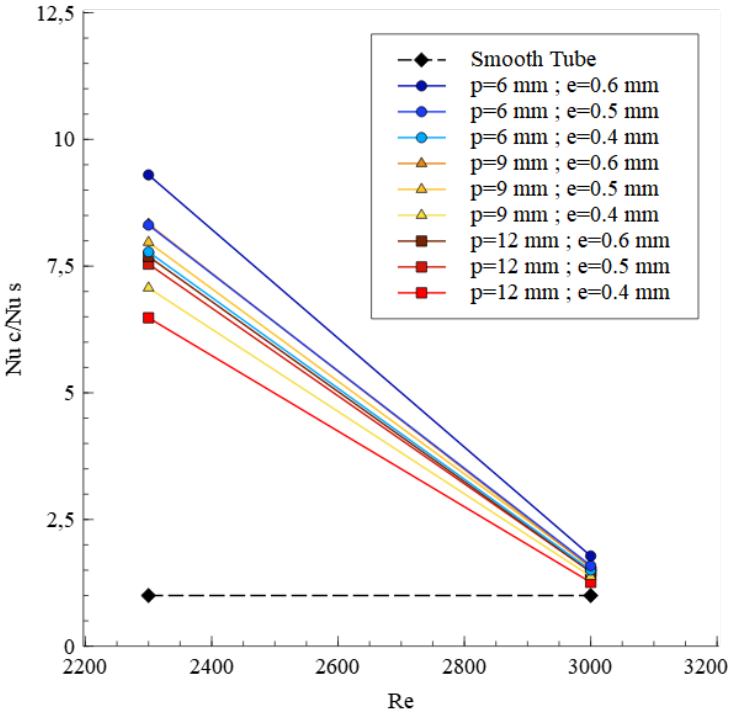

Figure 4.31: Comparison of the Nusselt augmentation factor as function of Reynolds number for the different corrugated tubes and smooth tube - Close up $Re = 2300 - 3000$ (turbulent regime)

the tubes have a better performance than the smooth tube after the transition.

For the turbulent regime (Fig. 4.29) one can observe that the Nusselt augmentation factor starts to increase more rapidly, practically in a linear way (the same way that happened to the friction augmen-

Table 4.2: Nusselt augmentation factor for the corrugated tubes compared to the smooth tube

Re	$p6e0.4/smooth$	$p6e0.5/smooth$	$p6e0.6/smooth$	$p9e0.4/smooth$	$p9e0.5/smooth$	$p9e0.6/smooth$	$p12e0.4/smooth$	$p12e0.5/smooth$	$p12e0.6/smooth$	$smooth/smooth$
100	0.92	0.86	0.81	0.96	0.93	0.89	0.98	0.96	0.93	1
250	0.92	0.86	0.83	0.97	0.93	0.90	1.00	0.97	0.94	1
400	0.93	0.88	0.87	0.98	0.94	0.94	1.01	0.98	0.97	1
550	0.94	0.91	0.92	1.00	1.00	1.00	1.03	1.01	1.02	1
700	0.96	0.95	0.98	1.02	1.04	1.06	1.05	1.09	1.09	1
850	2.59	3.24	3.93	2.44	2.84	3.37	2.38	2.60	3.14	1
1000	3.18	3.96	4.63	2.92	3.47	4.12	2.77	3.13	3.76	1
1150	3.80	4.61	5.25	3.42	4.08	4.60	3.19	3.66	4.33	1
1500	5.24	5.91	6.54	4.65	5.36	5.77	4.24	4.95	5.44	1
2300	7.78	8.31	9.30	7.07	7.97	8.33	6.48	7.54	7.69	1
3000	1.50	1.59	1.78	1.38	1.57	1.55	1.26	1.47	1.47	1

tation factor for this regime), obtaining its maximum of 9.3 at $Re = 2300$ for the tube with $6\ mm$ pitch and $0.6\ mm$ corrugation height and for the same Re its lowest of 6.48 for the tube with $12\ mm$ pitch and $0.4\ mm$ corrugation height. Looking at the close-up represented at Fig. 4.31 it is clear that as soon as the smooth tube becomes turbulent the Nusselt augmentation factor gets very low for all the tubes, becoming 1.78 for the tube with $6\ mm$ pitch and $0.6\ mm$ corrugation height and 1.26 for the tube with $12\ mm$ pitch and $0.4\ mm$ corrugation height. This happens due to the increase of the average Nusselt number for the smooth tube for this region.

In conclusion, for laminar region $Re = 100 - 700$ the Nusselt augmentation factor tends to be slightly lower for all the tubes. As the transition for the corrugated tubes occur there is a jump in the Nusselt augmentation factor which grows almost linearly for all the cases in the range of $Re = 850 - 2300$. Then, when the smooth tube becomes turbulent $Re = 2300 - 3000$ all the Nusselt augmentation factors decrease becoming almost as low as the laminar ones.

4.4 Corrugation effect on the flow

Based on the previous analysis one can now discuss and characterize the flow effects that the corrugation causes to the corrugated tubes.

As already mentioned by Liebenberg and Meyer [11] at the Topic Overview chapter 2.1, the main purpose of using passive techniques is to induce swirl and vortices at the secondary flow region which will mix the fluid layers with the core flow and increase the wet area. Kareem et al. [3] also stated that the main goal of the corrugation is to promote the secondary recirculation flow by inducing radial velocity components, mixing the flow layers and finally, increasing the wet perimeter with holding the throat cross-section area constant, which leads to an increase of the convective surface area. Therefore, the induced swirl effect it is pointed as the main feature of the corrugated tubes. As mentioned by Cruz [35], this effect is however mostly characterized by experimental results where its hard to analyse and obtain a qualitative description of the resulting flow.

As per numerical analysis made for the different corrugated tubes, one can affirm that the swirl effect produced by the corrugation transforms the inlet axial flow into a 3 dimensional flow as it is possible to verify by the cross section views presented at Fig. 4.32, Fig. 4.33 and Fig. 4.34 below which are decomposed into the 3 dimensional components of the velocity in cylindrical coordinates (axial, radial and tangential respectively). The influence on the corrugated tubes can then be verified on the pressure

losses and heat transfer through the tubes.

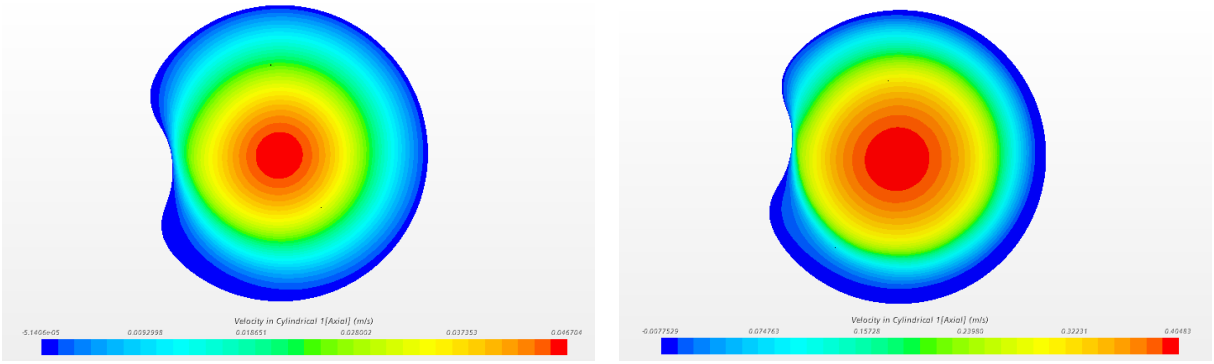

(a) $Re = 100$ (b) $Re = 1000$

Figure 4.32: Axial velocity for the laminar and turbulent flow regime of the tube with $p = 6\ mm$ and $e = 0.6\ mm$

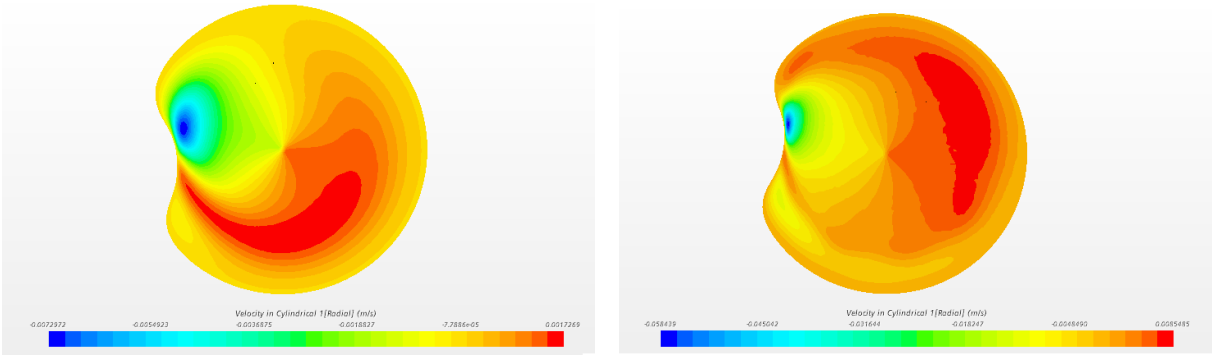

(a) $Re = 100$ (b) $Re = 1000$

Figure 4.33: Radial velocity for the laminar and turbulent flow regime of the tube with $p = 6\ mm$ and $e = 0.6\ mm$

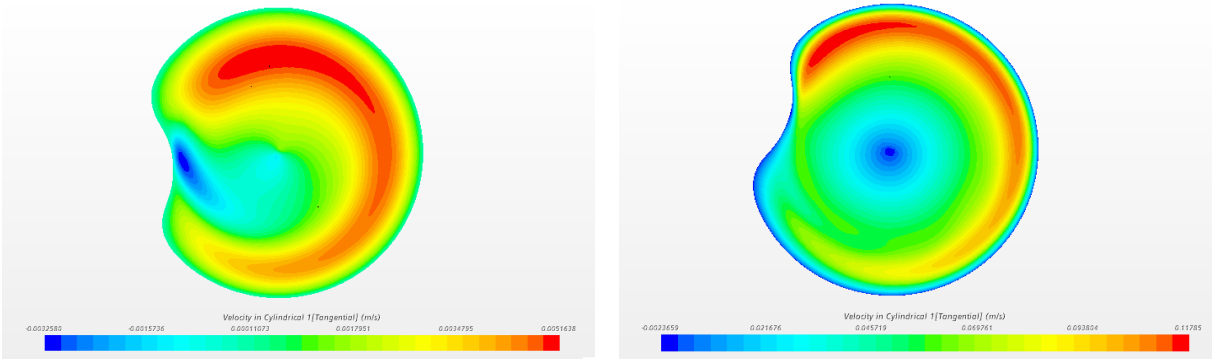

(a) $Re = 100$ (b) $Re = 1000$

Figure 4.34: Tangential velocity for the laminar and turbulent flow regime of the tube with $p = 6\ mm$ and $e = 0.6\ mm$

Starting by the axial velocity component, Fig. 4.32, it is possible to observe that the velocity profile shows a similar behaviour to the one obtained for the smooth tube, Fig. 2.3. As mentioned by Cruz [35], the continuity equation and the wall boundary condition (no-slip condition) forces the mass flow to the center of the tube, accelerating the flow towards the center. The same behaviour was verified for the

laminar and turbulent region. Note that the tube with $6\ mm$ pitch and $0.6\ mm$ corrugation height was only chosen as an example.

Now for the radial velocity component, Fig. 4.33, it is known to have its origin due to the corrugation geometry. As one can verify on the figure and as per Cruz [35], close to the corrugation, there is a zone where the flow has a radial negative component of the velocity. In his work it was also referred that its magnitude is almost 10 times higher than in the rest of the section. In this case, for the tube with $6\ mm$ pitch and $0.6\ mm$ corrugation height, the magnitude is ≈ 6 times higher for the laminar region and and ≈ 7 times higher for the turbulent region. This radial velocity magnitude is very small when compared with the magnitudes that the axial component of the velocity assumes. Therefore, and as per Cruz [35], it can be concluded that this radial component, despite being clearly produced by the corrugation, it is not large enough to, by itself, affect the flow significantly.

Finally, for the tangential velocity component, Fig.4.34, as it is possible to see that it induces swirls around the tube walls to towards the corrugation. In the work of Cruz [35] it is said to have a maximum magnitude is 10% of the axial component magnitude. In this case for the tube with $6\ mm$ pitch and $0.6\ mm$ corrugation height, the maximum tangential magnitude compared to the axial one is $\approx 11\%$ for the laminar region and and $\approx 30\%$ for the turbulent region. Therefore, the effects of the corrugation in the tangential velocity component are definitely more significant than in the radial one.

Overall, it is possible to confirm that the internal flow, for this example of corrugated tube, is a complex 3 dimensional flow with an induced swirl that promotes flow re-circulation and secondary flow regions which affect the pressure losses and the heat transfer of the tube.

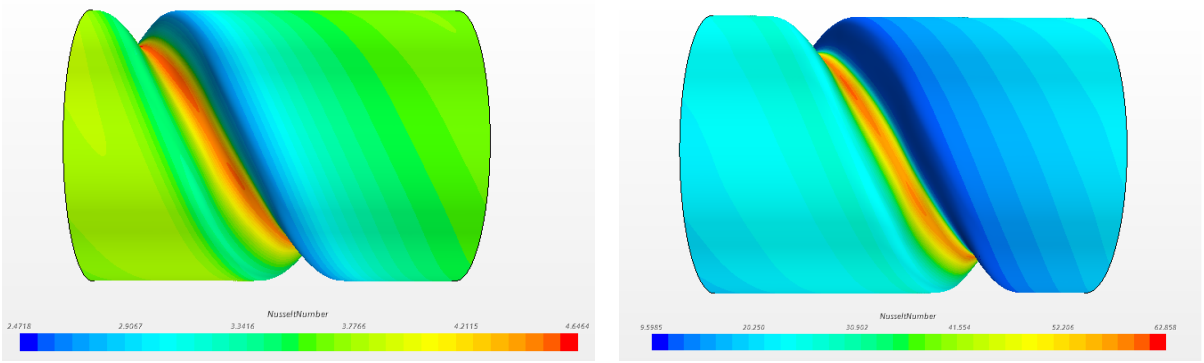

(a) $Re = 100$ (b) $Re = 1000$

Figure 4.35: Nusselt number for the laminar and turbulent regime of the tube with $p = 6\ mm$ and $e = 0.6\ m$

The corrugation has influence not only at the flow inside the corrugated tube but also in the heat transferred throughout the walls. As it is known, an uniform heat flux is applied to the tested tube walls. The Nusselt number was then presented at Fig. 4.35 (for laminar $Re = 100$ and turbulent $Re = 1000$ respectively) in order to study this behaviour. It is clear that inside the corrugation the Nu has a higher value (red zone) and right after the corrugation the lowest value is achieved (blue zone) which was also verified by Cruz [35]. In his work the low Nu after the corrugation is justified by the fact that there is a small flow separation in that zone. In the rest of the tube the heat transfer tends to be constant (green zone in the laminar region). For the same corrugation height, the longer the pitch the higher the area

with constant zone of heat transferred. For the turbulent regime there is a progressive improvement of the heat transferred from the end of one corrugation to the beginning of the next one. Once again, for the same corrugation height, the higher the pitch the sooner the in between corrugation area stabilizes for the Nu.

As per Cruz [35] the opposite can also happen, where the lowest Nusselt number occurs in the corrugation depth and the highest in the zone after it, which can be justified by the re-circulation zone induced at the corrugation.

One or another can occur depending on the pitch and the corrugation height used. Despite this it is also important to acknowledge that there is a gradient variation along a periodic domain of the flow for each corrugated tube, which makes one understand that the flow has a thermally pulsating behaviour.

4.5 Thermal Performance

In the previous chapters the isothermal friction factor (resultant of the pressure drop determined for each tube) and the average Nusselt number (heat transferred by each tube) were the two parameters that were studied and compared to the smooth tube's numerical data. Both of them were individually qualitatively and quantitatively analysed with the the support of the friction and Nusselt augmentation factors respectively. However an analysis which involves the combination of these two parameters is also needed. As per Cruz [35] this means that is relevant to have an analysis which can present a solution where it is possible to compare and decide which corrugated tube is better in terms of balancing the potential improvement of the heat transfer with an increased friction factor that in turn will demand a larger pumping power. To compliment this point Webb et al. [31] also suggested in his work that the main influential variables in order to obtain the optimum surface geometry of the flow in the tube are the pressure drop, heat transfer rate and flow rate.

So based on this and in order to achieve this dual criteria analysis the thermal performance factor presented in equation 4.1 below can be used.

$$\eta = \frac{Nu_c/Nu_s}{(f_c/f_s)^{1/3}} \tag{4.1}$$

This equation defines the ratio of the enhanced tube heat transfer coefficient to the smooth tube at constant pumping power and it was used by Wang et al. [49] and Pethkool et al. [51] among others.

Being this said, in the figure Fig. 4.36 below, it is possible to observe the general view for all the tubes for the Thermal Performance factor as function of Re throughout all the flow regimes ($Re = 100 - 3000$) and at table 4.3 all the correspondent values.

Looking closer to the laminar region ($Re = 100 - 700$) (Fig. 4.37) one can verify that all the corrugated tubes have a worse thermal performance than the smooth tube. This can be explained by the fact that for this regime the corrugation works more as an obstacle then as a heat transfer enhancement technique which makes the corrugation tubes have a higher friction factor than the smooth tube (Fig. 4.20) and a lower heat transfer comparing to the same (Fig. 4.27).

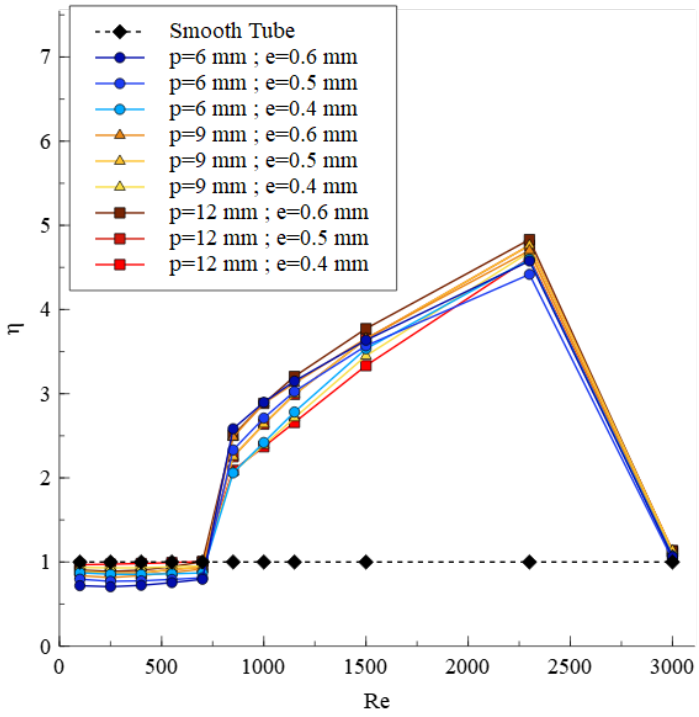

Figure 4.36: Comparison of the thermal performance as function of Reynolds number for the different corrugated tubes and smooth tube

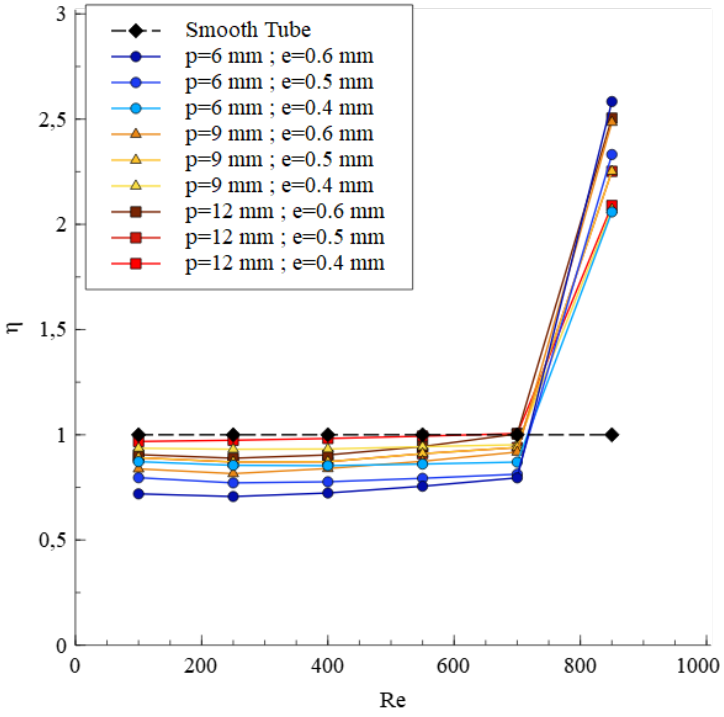

Figure 4.37: Comparison of the thermal performance as function of Reynolds number for the different corrugated tubes and smooth tube - Close up $Re = 100 - 850$ (laminar and transition regime)

As it is possible to see the values are slightly lower then the smooth tube's, being the tube with $6\ mm$ pitch and $0.6\ mm$ corrugation height the lowest performance for this region, having a factor of 0.72 at $Re = 100$ and 0.8 at $Re = 700$. The tube with $12\ mm$ pitch and $0.4\ mm$ corrugation height has the closest

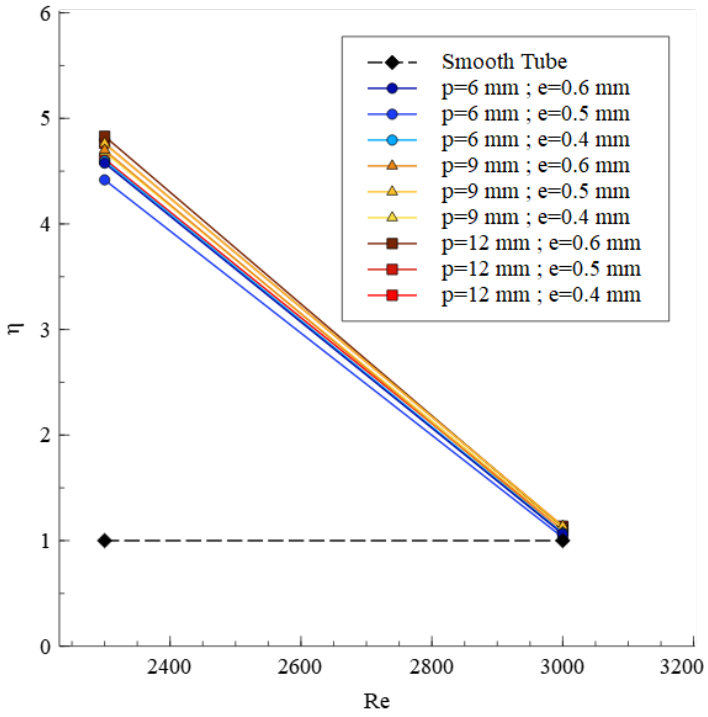

Figure 4.38: Comparison of the thermal performance as function of Reynolds number for the different corrugated tubes and smooth tube - Close up $Re = 2300 - 3000$ (turbulent regime)

thermal performance to the smooth tube, having a factor of 0.97 at $Re = 100$ and 1.01 at $Re = 700$. This happens due to the fact that this corrugated tube has a low corrugation height and therefore the closest wet area per unit length to the smooth tube's (Table 3.1).

As the transition occurs ($Re = 700 - 850$) there is a boost in thermal performance and the tube with 6 mm pitch and 0.6 mm corrugation height becomes the one with the highest thermal performance factor, 2.58 for $Re = 850$, and the tube with 6 mm pitch and 0.4 mm corrugation height becomes with the one with the lowest value, 2.06 for $Re = 850$. So all the corrugated tubes have a better performance than the smooth tube after the transition.

Table 4.3: Thermal performance factor for the corrugated tubes compared to the smooth tube

Re	$p6e0.4/smooth$	$p6e0.5/smooth$	$p6e0.6/smooth$	$p9e0.4/smooth$	$p9e0.5/smooth$	$p9e0.6/smooth$	$p12e0.4/smooth$	$p12e0.5/smooth$	$p12e0.6/smooth$	$smooth/smooth$
100	0.87	0.80	0.72	0.94	0.89	0.84	0.97	0.94	0.91	1
250	0.85	0.77	0.71	0.93	0.87	0.82	0.97	0.93	0.89	1
400	0.85	0.78	0.72	0.93	0.87	0.84	0.98	0.94	0.90	1
550	0.86	0.79	0.76	0.94	0.91	0.87	0.99	0.95	0.94	1
700	0.87	0.81	0,80	0.95	0.94	0.92	1.01	1.02	1.00	1
850	2.06	2.33	2.58	2.07	2.25	2.49	2.09	2.19	2.50	1
1000	2.42	2.71	2.90	2.39	2.64	2.89	2.37	2.55	2.88	1
1150	2.78	3.03	3.15	2.71	2.99	3.13	2.66	2.89	3.20	1
1500	3.53	3.57	3.64	3.45	3.65	3.66	3.33	3.65	3.77	1
2300	4.60	4.42	4.58	4.68	4.76	4.70	4.61	4.90	4.83	1
3000	1.07	1.03	1.06	1.11	1.14	1.08	1.11	1.17	1.12	1

For the turbulent regime presented at Fig. 4.36 ($Re = 850 - 3000$) one can observe that the thermal augmentation factor starts to increase more rapidly, practically in a linear way (the same behaviour as the friction augmentation factor and Nusselt augmentation factor for this regime), obtaining its maximum of 4.9 at $Re = 2300$ for the tube with 12 mm pitch and 0.5 mm corrugation height and for the same Re its lowest of 4.42 for the tube with 6 mm pitch and 0.5 mm corrugation height. In the middle section,

for Reynolds between 850 and 2300 the tube with $12\ mm$ pitch and $0.6\ mm$ corrugation height prevails with the highest thermal performance factor. There is such high thermal performance factor values in this range once the smooth tube is still in the laminar region and due to secondary flow resulting from vorticity.

Looking at the close-up represented at Fig. 4.38 it is clear that as soon as the smooth tube becomes turbulent (from $Re = 3000$) the thermal performance factor gets very low for all the corrugated tubes, having a maximum of 1.17 at $Re = 3000$ for the tube with $12\ mm$ pitch and $0.5\ mm$ corrugation height and having a minimum of 1.03 at $Re = 3000$ for the tube with $6\ mm$ pitch and $0.5\ mm$ corrugation height. As already mentioned this happens due to the increase of the heat transfer for the smooth tube for this region.

In conclusion, for laminar region $Re = 100 - 700$ the thermal augmentation factor tends to be slightly lower for all the tubes. As the transition for the corrugated tubes occur there is a jump in the thermal performance which grows almost linearly for all the cases in the range of $Re = 850 - 2300$. Then, when the smooth tube becomes turbulent $Re = 2300 - 3000$ all the thermal performance factors decrease becoming almost as low as the laminar ones.

Comparing these results with the ones obtained by Cruz [35] one can say that the thermal performance chart from his study demonstrate the same behaviour of the one here presented. However, one should note that for the laminar thermal performance factor, the results presented by his work are very high and better than the smooth tubes ones which can be explained by the fact that in his experimental work it was not possible to obtain thermally fully developed conditions for the laminar region as it is possible to see at Fig. 4.11, Fig. 4.12 and Fig. 4.13. In his work he also defines the region with the best thermal performance which goes from $Re = 1000$ (post corrugation tube transition) to $Re = 2000$ (pre smooth tube transition) and in fact it corresponds to the same here obtained ($Re = 850 - 2300$). In the turbulent regime he also presented lower values of thermal performance factor being those similar to the ones determined for the laminar regime.

These results also come in accordance to Kareem et al. [3] who concluded that for the analysis made for all the regimes (laminar, transition and turbulent) and in terms of optimization, the heat transfer is always accompanied with pressure drop which has higher values for a turbulent flow.

4.6 Pareto Efficiency Curve

Once the data from the thermal performance factor it is not enough to characterize the optimum flow working conditions for a heat exchanger it was also performed a multi-objective optimization study which determined the Pareto efficiency presented at Fig. 4.39. This study has the aim to verify the working conditions where it is possible to minimize the volume per heat transferred across the wall while minimizing pumping power.

As the heat flux through the walls of the different tubes is constant, the heat transferred is also constant. With a constant wet volume for each tube, in the chart one can observe horizontal lines once the volume per heat transferred (y axis) ends up being also constant which means that it is independent

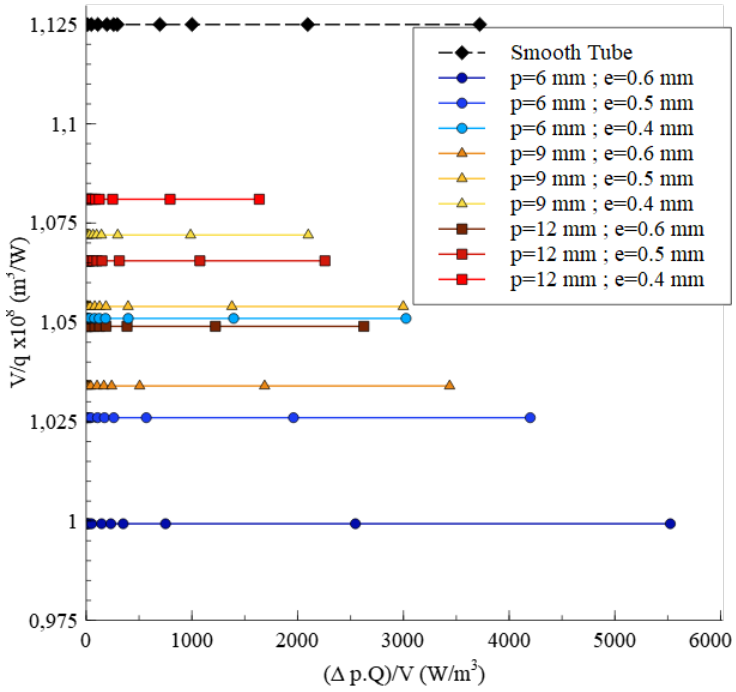

Figure 4.39: Pareto efficiency curve for the different corrugated tubes and smooth tube

of the pumping power per unit volume (x axis). This behaviour it is not verified for example at Guerra [62] and Passos [63] work once in their case there is a constant temperature imposed to the walls instead of a constant heat flux boundary condition.

So based on the results on Fig. 4.36 where it was concluded that the best thermal performance is achieved in the range $Re = 850 - 2300$ and based on the Fig. 4.39 where it is intended to minimize the volume per heat transferred across the wall while minimizing pumping power, it is possible to affirm that the most efficient working conditions happen for the tube with $6\ mm$ pitch and $0.6\ mm$ corrugation height for $Re = 850$. In case the best thermal performance is needed the tube with $12\ mm$ pitch and $0.5\ mm$ corrugation height for $Re = 2300$ can be chosen at a cost of a higher pumping power and higher volume per heat transferred.

Note that a higher pumping power implies a higher Reynolds number (along the x axis) being the last three dots to the right (of each curve) the pumping power corresponding to $Re = 1500$, 2300 and 3000 respectively. The lower Reynolds numbers ($Re = 100 - 1150$) dots are almost all together (for each curve) near to the y axis (volume per heat transferred) requiring then a lower pumping power. Being more precise, the highest pumping power for the laminar regime ($Re = 100 - 700$) goes for the corrugated tube with $6\ mm$ pitch and $0.6\ mm$ corrugation height with a value of $52\ W/m^3$ for $Re = 700$. The lowest pumping power for the laminar regime goes for the corrugated tube with $12\ mm$ pitch and $0.4\ mm$ corrugation height with a value of $30.1\ W/m^3$ for $Re = 700$. Finally, for the turbulent region $Re = 850 - 300$, the highest pumping power the happens again for the corrugated tube with $6\ mm$ pitch and $0.6\ mm$ corrugation height with a value of $5524.1\ W/m^3$ for $Re = 3000$ and the lowest pumping power the happens again for the corrugated tube with $12\ mm$ pitch and $0.4\ mm$ corrugation height with a value of $1637\ W/m^3$ for $Re = 3000$.

One can also observe that the smooth tube has similar values of pumping power to the tube with $9\ mm$ pitch and $0.6\ mm$ corrugation height however its volume per heat transferred is higher than all the other corrugated tubes. Despite this value being higher for the smooth tube, in general, in terms of magnitude they are all very close varying main in the pumping power which has an almost exponential growth as the Reynolds number increase.

Chapter 5

Conclusions

5.1 Work Summary

In this work the internal flow of 9-off corrugated tubes with pitch ($p = 6, 9, 12\ mm$) and corrugation height ($e = 0.4, 0.5, 0.6\ mm$) was characterized. The study was performed for $Re = 100 - 3000$ which goes from laminar to turbulent regime not only for the corrugated tubes but also for the smooth tube. The main aim was to optimize the flow and verify the influence of the corrugation geometry on the pressure losses and heat transfer. Water was used as a working fluid and all the properties were evaluated at a constant temperature of $300K$. The main boundary condition was the constant heat flux of $100\ kW/m^2$ that was imposed on the tube wall. A numerical model was developed with the CFD software STAR-CCM+, where the $k - \omega$ SST model was used to model the turbulence. The transition region was considered to be instantaneous.

Being this said, numerical analysis were first performed for the smooth tube. Their validation was important once only then it was possible to use the results as a comparison to the corrugated tubes. After that the corrugated tubes numerical results were obtained and validated with the available empirical data and Cruz [35] experimental data. After validation a comparison was made between all the corrugated tubes and the smooth tube. Note that all the results were evaluated for hydrodynamically and thermally fully developed conditions.

5.2 Main Conclusions

Finally, the following main conclusions can be presented:

- Corrugation induces a swirl promoting recirculating flow regions which decrease the critical Reynolds number and anticipate onset of the transition region;
- A higher corrugation height implies a faster transition;
- Thermal hot-spots with pulsating thermal behaviour were identified along a periodic corrugated tube domain;

- The best performance for the corrugation geometries was for $Re = 850 - 2300$ where it is verified an almost linear growth;
- The tube with $p = 6\ mm$ and $e = 0.6\ mm$ was the best in terms of thermal performance factor for $Re = 850$ with a value of 2.58, the tube with $p = 12\ mm$ and $e = 0.5\ mm$ was the best for $Re = 2300$ with a value of 4.9 and the tube with $p = 12\ mm$, $e = 0.6\ mm$ was the best in between;
- For $Re = 100 - 700$ the corrugated tubes show a lower thermal performance compared to the smooth tube and therefore it doesn't justify the use of a corrugated geometry;;
- For $Re = 3000$ the thermal performance is similar and also doesn't justify the use of a corrugated geometry;
- For constant heat flux and wet volume for each tube the heat transferred across the wall becomes constant and independent of the pumping power;
- In order to the heat exchanger to work with improved thermal performance and lower pumping power one should use the tube with $p = 6\ mm$ and $e = 0.6\ mm$ at $Re = 850$;
- In order to the heat exchanger to work with the maximum thermal performance one should use the tube with $p = 12\ mm$, $e = 0.5\ mm$ at $Re = 2300$ with a cost of a higher pumping power and a higher volume per transferred heat.

5.3 Recommendation for Future Work

After the main conclusions presented in the chapter above one can suggest a few improvements that can me made about the work here presented and a few other points to explore as an additional and complementing information for this research.

So the following points are presented:

- Expand the analysis for higher Reynolds numbers ($Re > 3000$) once the smooth tube's transition occurs very late and improve the numerical analysis (better convergence);
- Redo the experimental analysis for the 3-off tubes with 6, 9 and $12\ mm$ pitch and $0.4\ mm$ corrugation height and make experimental analysis for the 3-off tubes with 6, 9 and $12\ mm$ pitch and $0.5\ mm$ corrugation height and the 3-off tubes with 6, 9 and $12\ mm$ pitch and $0.6\ mm$ in fully developed hydrodynamic and thermal conditions in order to allow a better numerical results validation;
- Test the corrugated tubes in comparison with the smooth tube with a different test fluid (different Prandtl number);
- Test the corrugated tubes in comparison with the smooth tube with the constant wall temperature boundary condition instead of constant heat flux;

- Develop a double heat pipe heat exchanger or a compact heat exchanger made with the different corrugated tubes in order to evaluate the thermal performance and pumping power impact, both numerically and experimentally;

Bibliography

[1] J. Hærvig, K. Sørensen, and T. J. Condra. On the fully-developed heat transfer enhancing flow field in sinusoidally, spirally corrugated tubes using computational fluid dynamics. *International Journal of Heat and Mass Transfer*, 106:1051–1062, 2017.

[2] P. G. Vicente, A. GarcıÌa, and A. Viedma. Heat transfer and pressure drop for low reynolds turbulent flow in helically dimpled tubes. *International journal of heat and mass transfer*, 45(3):543–553, 2002.

[3] Z. S. Kareem, M. M. Jaafar, T. M. Lazim, S. Abdullah, and A. F. Abdulwahid. Passive heat transfer enhancement review in corrugation. *Experimental Thermal and Fluid Science*, 68:22–38, 2015.

[4] T. Dagdevir and V. Ozceyhan. An experimental study on heat transfer enhancement and flow characteristics of a tube with plain, perforated and dimpled twisted tape inserts. *International Journal of Thermal Sciences*, 159:106564.

[5] C. R. do Nascimento, V. C. Mariani, and L. dos Santos Coelho. Experimental analysis of r410a flow in helically rib-roughened tubes. *Thermal Science and Engineering Progress*, 20:100668, 2020.

[6] A. Sadeghianjahromi and C.-C. Wang. Heat transfer enhancement in fin-and-tube heat exchangers–a review on different mechanisms. *Renewable and Sustainable Energy Reviews*, page 110470, 2020.

[7] Z. Hajabdollahi, H. Hajabdollahi, and P. F. Fu. Improving the rate of heat transfer and material in the extended surface using multi-objective constructal optimization. *International Journal of Heat and Mass Transfer*, 115:589–596, 2017.

[8] Y. Camaraza-Medina, A. A. S. Escalona, O. M. Cruz-Fonticiella, and O. F. García-Morales. Method for heat transfer calculation on fluid flow in single-phase inside rough pipes. *Thermal Science and Engineering Progress*, 14:100436, 2019.

[9] Y. Hamada, W. Ohtsu, and J. Fukai. Thermal response in thermal energy storage material around heat transfer tubes: effect of additives on heat transfer rates. *Solar energy*, 75(4):317–328, 2003.

[10] C. Yu, H. Zhang, Y. Wang, M. Zeng, and B. Gao. Numerical study on turbulent heat transfer performance of twisted oval tube with different cross sectioned wire coil. *Case Studies in Thermal Engineering*, page 100759, 2020.

[11] L. Liebenberg and J. P. Meyer. In-tube passive heat transfer enhancement in the process industry. *Applied Thermal Engineering*, 27(16):2713–2726, 2007.

[12] O. Manca, S. Nardini, and D. Ricci. Numerical analysis of water forced convection in channels with differently shaped transverse ribs. *Journal of Applied Mathematics*, 2011, 2011.

[13] Z.-m. Xu and Z.-B. Zhang. Experimental investigation of the applied performance of several typical enhanced tubes. *Journal of Enhanced Heat Transfer*, 17(4), 2010.

[14] P. Naphon, M. Nuchjapo, and J. Kurujareon. Tube side heat transfer coefficient and friction factor characteristics of horizontal tubes with helical rib. *Energy Conversion and Management*, 47(18-19): 3031–3044, 2006.

[15] S. Rozzi, R. Massini, G. Paciello, G. Pagliarini, S. Rainieri, and A. Trifiro. Heat treatment of fluid foods in a shell and tube heat exchanger: Comparison between smooth and helically corrugated wall tubes. *Journal of food engineering*, 79(1):249–254, 2007.

[16] J. Den Toonder and F. Nieuwstadt. Reynolds number effects in a turbulent pipe flow for low to moderate re. *Physics of Fluids*, 9(11):3398–3409, 1997.

[17] P. G. Vicente, A. Garcıa, and A. Viedma. Experimental investigation on heat transfer and frictional characteristics of spirally corrugated tubes in turbulent flow at different prandtl numbers. *International Journal of Heat and Mass Transfer*, 47(4):671–681, 2004.

[18] T. Ravigururajan and A. Bergles. Prandtl number influence on heat transfer enhancement in turbulent flow of water at low temperatures. 1995.

[19] H. M. Blackburn, A. Ooi, and M. S. Chong. The effect of corrugation height on flow in a wavy-walled pipe. In *16th Australasian fluid mechanics conference*, pages 559–574, 2007.

[20] Y. Islamoglu and C. Parmaksizoglu. The effect of channel height on the enhanced heat transfer characteristics in a corrugated heat exchanger channel. *Applied Thermal Engineering*, 23(8):979–987, 2003.

[21] H. Mohammed, A. K. Abbas, and J. Sheriff. Influence of geometrical parameters and forced convective heat transfer in transversely corrugated circular tubes. *International Communications in Heat and Mass Transfer*, 44:116–126, 2013.

[22] S. Laohalertdecha and S. Wongwises. Condensation heat transfer and flow characteristics of r-134a flowing through corrugated tubes. *International Journal of Heat and Mass Transfer*, 54(11-12): 2673–2682, 2011.

[23] H. Safikhani and S. Eiamsa-ard. Pareto based multi-objective optimization of turbulent heat transfer flow in helically corrugated tubes. *Applied Thermal Engineering*, 95:275–280, 2016.

[24] H. Stel, A. Franco, S. Junqueira, R. Erthal, R. Mendes, M. Gonçalves, and R. Morales. Turbulent flow in d-type corrugated pipes: flow pattern and friction factor. *Journal of fluids engineering*, 134 (12), 2012.

[25] X.-w. Li, J.-a. Meng, and Z.-x. Li. Roughness enhanced mechanism for turbulent convective heat transfer. *International Journal of Heat and Mass Transfer*, 54(9-10):1775–1781, 2011.

[26] J.-A. Meng, X.-G. Liang, Z.-J. Chen, and Z.-X. Li. Experimental study on convective heat transfer in alternating elliptical axis tubes. *Experimental Thermal and Fluid Science*, 29(4):457–465, 2005.

[27] D. Khoeini, M. Akhavan-Behabadi, and A. Saboonchi. Experimental study of condensation heat transfer of r-134a flow in corrugated tubes with different inclinations. *International Communications in Heat and Mass Transfer*, 39(1):138–143, 2012.

[28] A. Barba, S. Rainieri, and M. Spiga. Heat transfer enhancement in a corrugated tube. *International communications in heat and mass transfer*, 29(3):313–322, 2002.

[29] S. Rainieri and G. Pagliarini. Convective heat transfer to temperature dependent property fluids in the entry region of corrugated tubes. *International Journal of Heat and Mass Transfer*, 45(22): 4525–4536, 2002.

[30] W. Wang, Y. Zhang, Y. Li, H. Han, and B. Li. Numerical study on fully-developed turbulent flow and heat transfer in inward corrugated tubes with double-objective optimization. *International Journal of Heat and Mass Transfer*, 120:782–792, 2018.

[31] R. Webb, R. Narayanamurthy, and P. Thors. Heat transfer and friction characteristics of internal helical-rib roughness. *J. Heat Transfer*, 122(1):134–142, 2000.

[32] S. Laohalertdecha, A. S. Dalkilic, and S. Wongwises. Correlations for evaporation heat transfer coefficient and two-phase friction factor for r-134a flowing through horizontal corrugated tubes. *International communications in heat and mass transfer*, 38(10):1406–1413, 2011.

[33] T. L. Bergman, F. P. Incropera, D. P. DeWitt, and A. S. Lavine. *Fundamentals of heat and mass transfer*. John Wiley & Sons, 2011.

[34] S. P. Software. Star-ccm+ (version 2020.1), 2004. URL `https://www.plm.automation.siemens.com/global/pt/products/simcenter/STAR-CCM.html`.

[35] G. J. G. Cruz. Experimental and numerical characterization of the flow and heat transfer inside corrugated pipes. Master's thesis, Instituto Superior Técnico, November 2019.

[36] G. G. Cruz, M. A. Mendes, J. M. Pereira, H. Santos, A. Nikulin, and A. S. Moita. Experimental and numerical characterization of single-phase pressure drop and heat transfer enhancement in helical corrugated tubes. *International Journal of Heat and Mass Transfer*, 179:121632, 2021.

[37] J. Doherty, P. Ngan, J. Monty, and M. Chong. The development of turbulent pipe flow. 2007.

[38] B. Petukhov, T. Irvine, and J. Hartnett. Advances in heat transfer. *Academic, New York*, 6:503–564, 1970.

[39] H. K. Tam, L. M. Tam, and A. J. Ghajar. Effect of inlet geometries and heating on the entrance and fully-developed friction factors in the laminar and transition regions of a horizontal tube. *Experimental thermal and fluid science*, 44:680–696, 2013.

[40] P. Hrycak and R. Andrushkiw. Calculation of critical reynolds numbers in round pipes and infinite channels and heat transfer in transition regions. In *International Heat Transfer Conference Digital Library*. Begel House Inc., 1974.

[41] M. Bernard. Mechanics of fluids. *London and New York: Taylor&Francis*, 2006.

[42] W. M. Kays, M. E. Crawford, and B. Weigand. Convective heat and mass transfer. Technical report, 2005.

[43] J. P. Meyer and M. Everts. Single-phase mixed convection of developing and fully developed flow in smooth horizontal circular tubes in the laminar and transitional flow regimes. *International Journal of Heat and Mass Transfer*, 117:1251–1273, 2018.

[44] V. Gnielinski. New equations for heat and mass transfer in turbulent pipe and channel flow. *Int. Chem. Eng.*, 16(2):359–368, 1976.

[45] V. Gnielinski. On heat transfer in tubes. *International Journal of Heat and Mass Transfer*, 63: 134–140, 2013.

[46] S. M. Ammar and C. W. Park. Validation of the gnielinski correlation for evaluation of heat transfer coefficient of enhanced tubes by non-linear regression model: An experimental study of absorption refrigeration system. *International Communications in Heat and Mass Transfer*, 118:104819, 2020.

[47] C. Yang, G. Liu, J. Zhang, and J.-y. Qian. Thermohydraulic analysis of hybrid smooth and spirally corrugated tubes. *International Journal of Thermal Sciences*, 158:106520, 2020.

[48] R. K. Ajeel, W. Saiful-Islam, K. Sopian, and M. Yusoff. Analysis of thermal-hydraulic performance and flow structures of nanofluids across various corrugated channels: An experimental and numerical study. *Thermal Science and Engineering Progress*, 19:100604, 2020.

[49] W. Wang, Y. Zhang, K.-S. Lee, and B. Li. Optimal design of a double pipe heat exchanger based on the outward helically corrugated tube. *International Journal of Heat and Mass Transfer*, 135: 706–716, 2019.

[50] P. Vicente, A. Garcia, and A. Viedma. Mixed convection heat transfer and isothermal pressure drop in corrugated tubes for laminar and transition flow. *International Communications in Heat and Mass Transfer*, 31(5):651–662, 2004.

[51] S. Pethkool, S. Eiamsa-Ard, S. Kwankaomeng, and P. Promvonge. Turbulent heat transfer enhancement in a heat exchanger using helically corrugated tube. *International Communications in Heat and Mass Transfer*, 38(3):340–347, 2011.

[52] H. K. Versteeg and W. Malalasekera. *An introduction to computational fluid dynamics: the finite volume method*. Pearson education, 2007.

[53] J. Blazek. *Computational fluid dynamics: principles and applications*. Butterworth-Heinemann, 2015.

[54] F. Andrade. Caracterização experimental da transmissão de calor em escoamentos no interior de tubos corrugados. Master's thesis, Instituto Superior Técnico, 2018.

[55] D. C. Wilcox et al. *Turbulence modeling for CFD*, volume 2. DCW industries La Canada, CA, 1998.

[56] F. R. Menter. Two-equation eddy-viscosity turbulence models for engineering applications. *AIAA journal*, 32(8):1598–1605, 1994.

[57] J. Córcoles-Tendero, J. Belmonte, A. Molina, and J. Almendros-Ibáñez. Numerical simulation of the heat transfer process in a corrugated tube. *International Journal of Thermal Sciences*, 126: 125–136, 2018.

[58] J. Córcoles, J. Belmonte, A. Molina, and J. Almendros-Ibáñez. Influence of corrugation shape on heat transfer performance in corrugated tubes using numerical simulations. *International Journal of Thermal Sciences*, 137:262–275, 2019.

[59] F. Andrade, A. Moita, A. Nikulin, A. Moreira, and H. Santos. Experimental investigation on heat transfer and pressure drop of internal flow in corrugated tubes. *International Journal of Heat and Mass Transfer*, 140:940–955, 2019.

[60] M. Everts and J. P. Meyer. Heat transfer of developing and fully developed flow in smooth horizontal tubes in the transitional flow regime. *International Journal of Heat and Mass Transfer*, 117:1331–1351, 2018.

[61] M. Everts and J. P. Meyer. Relationship between pressure drop and heat transfer of developing and fully developed flow in smooth horizontal circular tubes in the laminar, transitional, quasi-turbulent and turbulent flow regimes. *International Journal of Heat and Mass Transfer*, 117:1231–1250, 2018.

[62] B. M. B. Guerra. Unsteady flow and heat transfer through triply periodic minimal surfaces. Master's thesis, Instituto Superior Técnico, September 2020.

[63] A. G. P. Passos. Laminar flow and heat transfer in triply periodic minimal surfaces. Master's thesis, Instituto Superior Técnico, July 2019.